Scintillation Particle Detectors Based on Plastic Optical Fibres and Microfluidics

THÈSE N^{O} 5033 (2011)

PRÉSENTÉE LE 2 SEPTEMBRE 2011

À LA FACULTÉ SCIENCES ET TECHNIQUES DE L'INGÉNIEUR

LABORATOIRE DE MICROSYSTÈMES 4

PROGRAMME DOCTORAL EN MICROSYSTÈMES ET MICROÉLECTRONIQUE

ÉCOLE POLYTECHNIQUE FÉDÉRALE DE LAUSANNE

POUR L'OBTENTION DU GRADE DE DOCTEUR ÈS SCIENCES

PAR

Alessandro MAPELLI

acceptée sur proposition du jury:

Prof. M. A. Ionescu, président du jury
Prof. Ph. Renaud, Dr P. L. G. Grafström, directeurs de thèse
Prof. A. Bay, rapporteur
Dr B. Gorini, rapporteur
Dr M. Haguenauer, rapporteur

ÉCOLE POLYTECHNIQUE
FÉDÉRALE DE LAUSANNE

Suisse
2011

per Elisa

Abstract

This thesis presents the design, development, and experimental validation of two types of scintillation particle detectors with high spatial resolution. The first one is based on the well established scintillating fibre technology. It will complement the ATLAS (A Toroidal Large ApparatuS) detector at the CERN Large Hadron Collider (LHC). The second detector consists in a microfabricated device used to demonstrate the principle of operation of a novel type of scintillation detector based on microfluidics.

The first part of the thesis presents the work performed on a scintillating fibre tracking system for the ATLAS experiment. It will measure the trajectory of protons elastically scattered at very small angles to determine the absolute luminosity of the CERN LHC collider at the ATLAS interaction point. The luminosity of an accelerator characterizes its performance. It is a process-independent parameter that is completely determined by the properties of the colliding beams and it relates the cross section of a given process to the corresponding event rate. Detector modules will be placed above and below the LHC beam in roman pot units at a distance of 240 m on each side of the ATLAS interaction point. The roman pots are vessels allowing the detectors to approach the beam axis at distances of the order of a millimetre. Overlap detectors, also based on the scintillating fibre technology, will measure the precise relative position of the two detector modules. Results obtained during beam tests at DESY and at CERN validate the detectors design and demonstrate the achievable spatial resolution.

The second part of the thesis introduces a novel type of scintillation detector based on microfluidics, describing its main features and their experimental validation. Microfluidic devices can be fabricated in a single photolithographic step with dimensional resolutions of the order of a micrometre. Microchannels can be easily filled with scintillating fluid, overcoming the difficulties encountered with previous liquid scintillation detectors made of capillary bundles. The possibility to circulate and to replace the irradiated liquid scintillator makes the active medium of the detector intrinsically ra-

diation hard. Moreover, by changing the scintillator in the microchannels, the same device can be used to detect different types of particles.

Prototype detectors have been fabricated by using a photosensitive resin (SU-8) as structural element. The SU-8 negative-tone photoresist exhibits outstanding properties such as good adhesion on different types of substrates, high mechanical strength and chemical stability. Moreover, its high level of resistance to radiation damage, comparable to Kapton film, makes it a good candidate for novel radiation detectors. A standard SU-8 process has been optimized to fabricate dense arrays of hollow optical waveguides filled with liquid scintillator and coupled to external photodetectors. The photoelectric yield of this assembly is in good agreement with theoretical predictions and it is comparable to the yield of commercial small diameter scintillating fibres.

Microfluidic scintillation detectors can be designed and processed to meet the requirements of a wide range of applications like dosimetry, beam profiling, particle tracking, and calorimetry for high energy physics experiments, medical imaging, hadrontherapy and security devices. Miniaturized detectors as well as large devices can be fabricated with the same microfabrication techniques.

Keywords: *ATLAS, LHC, CERN, Charged-particle tracking, Scintillation detectors, Scintillating fibres, Liquid scintillators, Photodetectors, Microfabrication, Microfluidics, SU-8 negative photoresist.*

Version abrégée

Le travail présenté dans cette thèse traite du développement et de la caractérisation de deux types de détecteurs scintillants. Dans le premier cas, il s'agit d'un détecteur à fibres scintillantes qui sera utilisé pour déterminer la trajectoire de protons du Grand Collisionneur de Particules (LHC) au CERN. La seconde partie de la thèse présente la démonstration du principe de fonctionnement d'un nouveau type de détecteur scintillant basé sur des techniques de microfluidique.

La première partie de cette thèse décrit le travail effectué sur un système de détecteurs à fibres scintillantes pour l'expérience ATLAS (A Toroidal Large ApparatuS) au LHC. La luminosité absolue du LHC au point d'interaction d'ATLAS sera déterminée par la reconstruction des trajectoires des protons diffusés élastiquement. Un ensemble de détecteurs à fibres scintillantes ALFA (Absolute Luminosity For ATLAS) a été étudié pour effectuer cette mesure. Des modules de détection seront placés au-dessus et au-dessous du faisceau du LHC dans des pots romains à une distance de 240 m de part et d'autre du point d'interaction d'ATLAS. Les pots romains sont des récipients qui séparent les détecteurs du vide primaire du LHC. Ils permettent d'approcher les détecteurs à des distances de l'ordre du millimètre par rapport à l'axe du faisceau. Les détecteurs sont composés de 10 plans de 2×64 fibres scintillantes, arrangées perpendiculairement, dont la lumière est lue par des photomultiplicateurs multi-anodes. La position relative entre le détecteur du haut et celui du bas est déterminée par des détecteurs dits de recouvrement. Ces détecteurs sont installés au-dessous, et au-dessus, des détecteurs principaux pour détecter principalement des particules du halo du faisceau. Leur position est fixe par rapport aux détecteurs principaux et elle est déterminée avec précision préalablement à l'insertion dans les pots romains. Plusieurs tests en faisceau ont permis de valider le concept et la géométrie du système de trajectographie ALFA.

Dans la seconde partie de la thèse, le principe de fonctionnement d'un nouveau détecteur scintillant microfluidique est démontré. Les systèmes microfluidiques peuvent être fabriqués en une seule étape de photolithographie avec des éléments structurels dont

les dimensions sont de l'ordre du micromètre. Ils permettent de contrôler le flux de liquides scintillants dans des microcanaux de façon simplifiée par rapport aux détecteurs scintillants constituées de faisceaux de capillaires. Ceci permet de faire circuler et de remplacer le liquide scintillant endommagé par les radiations, prolongeant ainsi la durée de vie du détecteur. De plus, en changeant le type de scintillateur dans les microcanaux, il est possible d'utiliser le même détecteur pour différents types de mesures.

Plusieurs techniques de microfabrication ont été envisagées pour la fabrication de ces détecteurs. Les prototypes étudiés dans cette thèse ont été fabriqués en utilisant une résine photosensible, le SU-8, comme élément structurel. Le SU-8 est une photorésine négative avec de très bonnes propriétés mécaniques et chimiques. Sa tenue aux radiations, comparable à celle de films Kapton, la rend très intéressante pour la fabrication de nouveaux détecteurs scintillants. Un procédé standard de photostructuration de la résine SU-8 a été optimisé pour fabriquer des réseaux de canaux microfluidiques remplis de liquide scintillant et couplés à des photodétecteurs. Le rendement photoélectrique de ces détecteurs a été mesuré en exposant le liquide à des électrons. Il est en accord avec les estimations théoriques et il est du même ordre de grandeur que celui de fbres scintillantes commerciales.

Les détecteurs scintillants microfluidiques peuvent être conçus pour répondre aux exigences de nombreuses applications telles que la dosimétrie, le profilage de faisceau, la trajectographie et la calorimétrie dans des domaines aussi variés que la sécurité, l'imagerie médicale, la hadrothérapie et la physique des particules. Les mêmes techniques de microfabrication permettent de construire des détecteurs miniaturisés ainsi que des grandes surfaces de détection.

Mots-clés : *ATLAS, LHC, CERN, Détecteurs scintillants, Fibres scintillantes, Liquides scintillants, Photodétecteurs, Microfabrication, Microfluidique, Photorésine négative SU-8.*

Acknowledgements

I would like to express my deepest gratitude to Professor Philippe Renaud for his guidance, support, and enthusiasm over the past years. Working with him has been a very rewarding experience.

During my CERN doctoral studentship, I was supervised by Per Grafström and Christian Joram. They gave me the opportunity to discover the fascinating world of particle physics and they taught me valuable skills on detector technologies.

My gratefulness goes to Marzio Nessi and Philippe Farthouat who advised me to apply for a doctoral studentship at CERN. This was the starting point of a great experience that I shared with Madeleine, Miranda, Eva, Chantal, Carlo, Vladimir, Georges, Wieslaw, Christophe, Claude, Thomas, Jérôme(x), Andrea, Hans, Eric, Michel, Neil, André(s), Raphaël, Adrian, Maurice, Luc, Loic, José, Antti, Franciso, Paolo, and Mario.

I am forever indebted to Noelia, Xavier, and Sébastien for unveiling the mysteries of SU-8 and to the students I had the chance to supervise students at CERN and EPFL for the quality of the data they provided; Pierre, Henrik, Sune, Loic and Antonin. Thanks to Carla, Marco and Giulio for their MAPMT and read-out with which I characterized the microchannels. Professor André Rubbia allowed me to work in his laboratory and Professor Pio Picchi was of great help for the characterization of the microchannels. I also wish to thank Giovanna, Maurice, Benedetto, and Wainer for all the fruitful discussions and for their help with the experiments.

I sincerely thank my LMIS4 colleagues for the stimulating scientific, and less scientific, discussions; Ana, Lynda, Sophie, Nina, Ludovica, Bilge, Nicolas(s), Shady, Marc, Pierre, Harsha, Anja, Matteo, Pontus, Arnaud, Robert, André, Guillaume, Mario, uRBAN, Raphaël, Harald, and Fabien.

Many thanks to Arnaud for rigorously correcting my work whenever I asked him. Thanks Aurélie for bravely going through all the manuscript. Thanks Nico for all your good tips!

I thank all the staff of the CMI clean room at EPFL for running such a great clean room. I also thank all the users of the clean room, and in particular Mohssen, for sharing their expertise and good sense of humor during the long hours we spent down there dressed up in fancy suits.

I also wish to thank all the ladies, both at EPFL and at CERN, who made my administrative life so easy, Marie, Rose-Mary, Sylvie, Kathlyn, Claudia, Karine, Sandra, Claire, Kate, and Véronique. Merci les filles.

Above all, I would like to thank my parents Annamaria and Livio, my sister Elisa, and my significant other Mélanie for their unconditional love and support. Grazie!!

Contents

Chapter 1

Introduction

This chapter gives a brief account of scintillation detectors. The goals and the motivations of the thesis are then described, namely the design and the experimental validation of two different types of scintillation detectors. The first detector is based on a standard scintillating fibre tracker configuration. It will be used by the ATLAS experiment at the CERN LHC collider. The second development stems from the original idea of microfluidic scintillation detection. Lastly, the structure of the thesis is outlined.

1. Introduction

1.1 A brief history of scintillation detectors

Scintillation detectors make use of the property that certain materials, when struck by a nuclear particle or radiation, emit a small flash of light (*i.e.* scintillation). When coupled to a photodetection device, these scintillations can be converted into electrical pulses which can be analyzed to give information concerning the incident radiation. The first detection device using scintillators, known as the spinthariscope, was built in 1903 by Crookes[1]. It consisted of a Zinc Sulfide (ZnS) screen which produced scintillations when struck by α particles. These flashes of light were observed with the naked eye though a microscope in a darkened room. This setup was used in 1909 by Geiger and Marsden[2] to study the scattering of α particles and resulted in Rutherford's discovery of the atomic nucleus[3]. Despite having been used for this major breakthrough, visual scintillation counters were quickly abandoned with the invention of the gaseous ionization instruments. In 1944, the scintillation counter was restored by replacing the human eye with the newly developed photomultiplier tube (PMT). The weak scintillations could thus be efficiently, and reliably, detected much faster than with gas-filled counters. This was the beginning of modern electronic scintillation detectors. Today, scintillation detectors are widely used for the detection of α and β particles, gamma and X rays, and neutrons in many fields such as high-energy physics, medical imaging, dosimetry and security.

A typical scintillation detector consists of three main parts: a scintillator, a photodetector, and a read-out system. There are many different types of scintillation materials which can be classified into inorganic crystals, glasses and gases, and organic compounds such as crystals, plastics and liquids. PMTs are the most commonly used photodetectors with scintillators. Lately, Geiger-mode avalanche photodiodes (GM-APD), also known as silicon photomultipliers (SiPM), have started being used to detect scintillation light instead of traditional vacuum photomultipliers. The final component of the scintillation detection system is the signal-processing and data acquisition electronics which allows to count and possibly quantify the amplitude of the signals. The design of this electronics depends essentially on the type of application.

1.2 Motivation and scope of this thesis

Two different types of scintillation detectors have been studied in this thesis. The first detector is a scintillating fibre tracker used to measure the trajectory of elastically scattered protons very close to the LHC beam at CERN. The second detector consists

of a microfabricated device containing a liquid scintillator used to demonstrate the feasibility of a scintillation detector based on microfluidics.

The two main goals of this thesis can be summarized as:

- the fabrication and studies of plastic scintillating fibre prototype detectors to validate the proposed design for the measurement of the CERN LHC absolute luminosity at the ATLAS interaction point IP1,
- the validation of a novel type of scintillation detector based on microfluidics. The scope of this research work being to design, fabricate, and characterize a microfluidic device used for scintillation detection.

1.2.1 Scintillating fibre tracker

The first part of the thesis presents the work performed on a scintillating fibre tracking system for the ATLAS experiment. The ATLAS experiment will determine the absolute luminosity of the CERN LHC collider at IP1 by measuring the trajectories of protons elastically scattered at very small angles. A scintillating fibre tracker system, called ALFA, is proposed for this measurement. Detector modules will be placed above and below the LHC beam axis in Roman Pot units at a distance of 240 m on each side of the ATLAS interaction point. They allow to approach the beam axis at millimetre distance. Overlap detectors, also based on the scintillating fibre technology, will measure the precise relative position of the two detector modules.

The results obtained with prototype detectors, during various beam test experimental campaigns at DESY and at CERN, allowed to validate the detector's design and to demonstrate the achievable spatial resolution.

1.2.2 Microfluidic scintillation detector

The second part of the thesis provides the experimental demonstration of a novel type of scintillation detector based on microfluidics. It consists of a single microfluidic channel, filled with a liquid scintillator, and designed to define an array of scintillating waveguides each independently coupled to a photodetector. The experimental validation has been performed with detectors fabricated by structuring thick layers of the SU-8 negative photoresist deposited on silicon substrates. The results obtained with these devices show a light yield compatible with the theoretical expectations and comparable to small diameter scintillating fibres.

1.3 Thesis structure

A general introduction to scintillating detector assemblies is presented in Chapter 2. The requirements for the absolute luminosity measurement of the LHC collider at the ATLAS interaction point are presented and the chosen solution, based on a plastic scintillating fibres tracker, is described in Chapter 3. The fibres characterizations and beam tests experiments necessary to validate the fibre tracker design are reported in Chapter 4. The concept and experimental validation of a novel type of scintillation detector based on microfluidics are detailed in Chapter 5. General conclusions on the work performed with these two different types of scintillation detectors are drawn in Chapter 6 before depicting the perspectives for both detectors.

Chapter 2

Overview of scintillation detectors

This chapter introduces the main characteristics of the interactions of particles with matter. The properties of scintillation materials are presented and a general overview of scintillation detector assemblies is given. The basic formulas necessary for the analysis of scintillation detectors data are described.

2.1 Introduction

The basis of particle detection relies on the knowledge of the interactions occurring when particles encounter matter. These interactions depend both on the characteristics of the particle and of the detector material. When a charged particle traverses matter, it excites molecules along its path. Certain types of molecules release a small fraction of this energy, typically in the order of 3%, as optical photons. This process, known as scintillation, is especially relevant for organic substances containing aromatic rings, such as polystyrene (PS) and polyvinyltoluene (PVT) as well as scintillating liquids with toluene and xylene. Ease of fabrication and low costs have made plastic scintillators a common detector component. Recently, plastic scintillating fibres have also found widespread use in tracking and calorimetry.

2.2 Passage of particles through matter

Charged particles moving through matter interact with its components. These interactions can lead to excitation or ionization and lead to an energy loss of the traveling particles. If one considers heavy charged particles, two processes are responsible for their energy loss and their deflection when traversing a material. They lose energy by interacting with atomic electrons while elastic collisions with the atomic nuclei change their path. The inelastic interactions with the atomic electrons can be divided in two groups. The soft collisions in which only an excitation results, and the hard collisions in which sufficient energy is transferred to cause ionization. In some of the hard reactions, the transferred energy is sufficient for the ejected electron itself to cause substantial secondary ionization. These high energy recoil electrons are sometimes referred to as δ-rays or knock-on electrons. The rate of energy loss, or stopping power, in a certain range, expressed in $\mathrm{MeVg^{-1}cm^2}$, is given by the Bethe-Bloch equation

$$-\frac{dE}{dx} = Kz^2\frac{Z}{A}\frac{1}{\beta^2}\left(\frac{1}{2}\ln\frac{2m_ec^2\beta^2\gamma^2T_{max}}{I^2} - \beta^2 - \frac{\delta\left(\beta\gamma\right)}{2}\right) \tag{2.1}$$

where:

- K=$4\pi N_A r_e^2 m_e c^2$,
- z is the charge of the incident particle,
- Z is the atomic number of the absorber,

- A its atomic mass,
- β=v/c is the velocity of the particle expressed in multiples of c,
- m_e is the electron mass at rest,
- c is the velocity of light,
- γ=$1/\sqrt{1-\beta^2}$ is the Lorentz factor, and
- $\delta\,(\beta\gamma)$ is the density effect correction to ionization energy loss.

The Bethe formula describes the energy loss per distance travelled of charged particles such as protons, alpha particles, and atomic ions, but not electrons traversing matter or, alternatively, the stopping power of the material in a given energy range. The function computed for muons in copper is shown as the "Bethe" region of Fig. 2.1. Only in the Bethe region is it a function of β alone; the mass dependence is more complicated in other regions and is described elsewhere[4]. Most relativistic particles have mean energy loss rates close to the minimum in this region and they are referred to as minimum-ionizing particles (MIP).

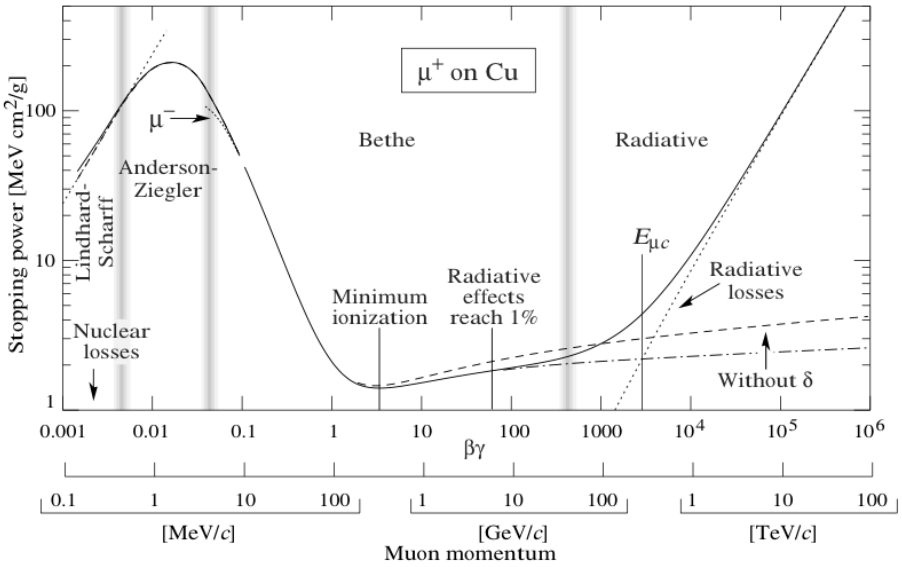

Figure 2.1: Stopping power (= $\langle -dE/dx \rangle$) for positive muons in copper as a function of $\beta\gamma = p/Mc$. Solid curves indicate the total stopping power[4].

High-energy electrons predominantly lose energy in matter by bremsstrahlung, and high-energy photons by e^+e^- pair production. The characteristic amount of matter traversed for these interactions is called the radiation length X_0, usually measured in g·cm^{-2}. It is both the mean distance over which a high-energy electron loses all but $1/e$

of its energy by bremsstrahlung and 7/9 of the mean free path for pair production by a high-energy photon. It is also the appropriate scale length for describing high-energy electromagnetic cascades. The radiation length X_0 can be defined by the following empirical fit to all existing data

$$X_0 = \frac{716.4 \cdot A}{Z\,(Z+1)\ln\frac{287}{\sqrt{Z}}} \tag{2.2}$$

where Z is the atomic number and A is the mass number.

2.3 Scintillation materials

Scintillators convert the energy of impinging charged particles, or photons, into photons in the visible range. In the case of inorganic scintillators, this is an effect in the crystal lattice whereas in organic scintillators this is simply fluorescence. Inorganic scintillators have a high light output and a slow response while organic scintillators have a low light output but are fast. Table 2.1 lists typical values of light yield and peak emission wavelength for different types of scintillation materials commonly used for detection applications. The quoted light yield is for low dE/dx particles such as fast electrons. The light is emitted in all directions inside the scintillator.

Table 2.1: Typical light yield, expressed in photons per keV, of deposited energy, wavelength of maximum emission, and decay time constants for scintillating materials typically used for detection applications.

Material	Light yield (ϕ/keV)	λ_{peak} (nm)	Decay time (s)
Glass scintillators	3 - 5	400	$\approx 10^{-9}$
Plastic scintillators	8 - 10	420	$\approx 10^{-9}$
Liquid scintillators	11 - 13	420	$\approx 10^{-9}$
Inorganic crystals	40 - 90	415 - 480	$\approx 10^{-7}$

2.3.1 Organic scintillators

Organic scintillators use the ionization produced by charged particles to generate optical photons, usually in the blue to green wavelength region. They are broadly classed into three categories; crystals, liquids, and plastics.

Scintillation light in organic compounds arises from transitions made by free electrons of the molecules. Energy deposition from a charged particle passing through the material excites the electrons from the ground state to higher states. They quickly decay to a lower state via non-radiative transitions. Light emission from this state to ground state

is known as fluorescence, and operates on a time scale of nanoseconds. Secondary fluors are integrated in the compounds and used as wavelength shifters (WLS) to shift this scintillation light to a wavelength better matched to the sensitivity of photodetectors. The absorption and emission processes occur in complex molecules and they are spread out over a wide range of photon energies with an overlap between the two spectra. This means that a fraction of the emitted light is re-absorbed. This self-absorption leads to a shortened attenuation length. The wavelength difference between the absorption and emission peaks is called the Stokes' shift. The greater this shift is, the smaller the self-absorption.

Decay times of organic scintillators are in the range of few nanoseconds and rise times are much faster. The combination of high light yield and fast response allows sub-nanosecond time resolutions. The fraction of light emitted during the decay tail depends on the nature of the exciting particle and can thus allow pulse shape discrimination and be used for particle identification.

Because of the molecular nature of luminescence in organics, these materials can be used in many physical forms without the loss of their scintillating properties. As detectors, they have been used in the form of pure crystals and as mixtures in liquid and solid solutions.

2.3.1.1 Liquid organic scintillators

A category of useful scintillators is produced by dissolving an organic scintillator in a solvent. Liquid scintillators consist simply of these two components, or a third constituent is sometimes added as a wavelength shifter to tailor the emission spectrum to better match the spectral response of the photodetectors. Because of their lack of a solid structure that could be damaged by exposure to intense radiation, liquid scintillators are more resistance to radiation damage than crystalline or plastic scintillators[5].

Liquid scintillators are often sold commercially in sealed glass containers and are handled in the same manner as solid scintillators. In certain applications, large volume detectors with dimensions of several meters may be required and liquid scintillators are often the only practical choice from the cost point of view. Liquid scintillators are also widely used to count radioactive material that can be dissolved as part of the scintillator solution. Radiations emitted by the source immediately pass through a portion of the scintillator and the counting efficiency can be close to 100%. This technique is widely used for counting low level beta activity of carbon-14 or tritium.

2.3.1.2 Plastic scintillators

If an organic scintillator is dissolved in a solvent that can then be polymerized, a solid solution is produced. Typical plastic matrices for scintillators are polystyrene (PS), polyvinyltoluene (PVT), or polymethylmethacrylate (PMMA). Plastics scintillators can easily be fabricated and shaped. They have become a very common form of organic scintillator and they are available commercially with a large variety of sizes of rods, cylinders, sheets, and fibres. The material is relatively inexpensive and plastic scintillators are often the only practical choice when it comes to large volume solid scintillation detectors. There is also a wide selection of plastic scintillators available as small diameter fibres. They can be used either as single fibres or grouped together to form bundles in applications where the particle position must be reconstructed with good spatial resolution (see Section 2.4.3).

Plastic scintillators used in detectors consist of binary and ternary solutions of selected fluors in a plastic base containing aromatic rings. Most of them have a base of either PS or PVT. Figure 2.2 depicts the scintillation mechanism.

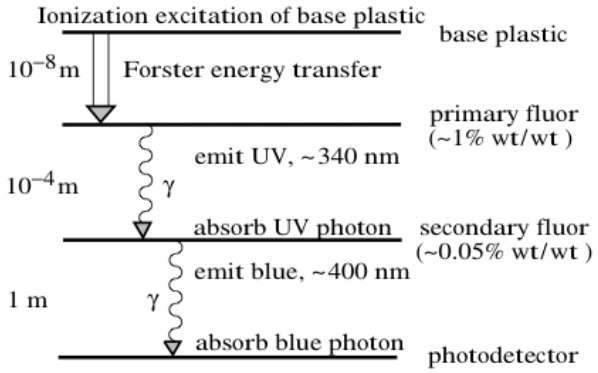

Figure 2.2: Operating mechanism of a plastic scintillator. Approximate fluor concentrations and energy transfer distances for the separate sub-processes are shown[4].

Ionization in the plastic base produces UV photons with short attenuation length in the order of a few mm. Longer attenuation lengths can be obtained by dissolving a primary fluor in high concentration, about 1% in weight, into the base. The fluor is selected to efficiently re-radiate the absorbed energy at wavelengths where the base is more transparent. The other function of this fluor is to shorten the decay time and to increase the total light yield. The scintillator base materials can have long decay times. For example, pure PS has a decay time of 16 ns. The addition of a primary fluor in high concentration can shorten the decay time by an order of magnitude. It is often necessary to add a secondary fluor, at fraction percent levels, and occasionally

a third one in order to shift light to longer wavelengths to better match the region of maximum sensitivity of the photodetectors.

2.3.1.3 Other types of organic scintillators

Pure organic crystals, thin plastic films and loaded organic scintillators can also be used for detection purposes.

Anthracene and Stilbene are commonly used as pure organic crystalline scintillators. Anthracene has the highest scintillation efficiency. For this reason, the light output per unit energy of scintillators is often described as a percentage of the light output of Anthracene. Stilbene has a lower efficiency but it is commonly used when pulse shape discrimination is required. Both materials are relatively fragile and difficult to obtain in large sizes. Moreover their efficiency of scintillation depends on the orientation of the ionizing particle with respect to the crystal axis[6].

Very thin films of plastic scintillator with thicknesses as low as 20 μg/cm^2 can be fabricated. They are very useful for detecting weakly penetrating particles such as heavy ions. The thickness of these detectors can be one or two orders of magnitude smaller than the minimum possible with other types of detectors. Thin films with thicknesses of the order of 10 μm are commercially available[7]. Thinner films can be produced with techniques such as evaporation from a solution of plastic scintillator[8;9;10;11] or spin-coating[12;13]. The film can be deposited directly on the active surface of a photodetector[9;14], or the light can be collected through a light guide in contact with the edges of the thin film[15;16]. It can also be placed inside a reflecting cavity[15;17;18;19;20]. Their short decay times in the order of few nanoseconds makes them very attractive for fast timing measurements[21].

Organic scintillators can be used for the direct detection of beta particles (fast electrons), alpha particles (positive ions) and also fast neutrons through the proton recoil process but due to the low Z-value of their constituents (hydrogen, carbon and oxygen), gamma-rays cannot be promptly detected. To provide a way of detecting them, organic scintillators can be doped with high Z elements such as lead or tin[22;23]. Even though such loaded organic scintillators have the advantage of a fast response with respect to conventional gamma-ray scintillators, the addition of these high Z elements leads to a decreased light output and the achievable energy resolution is therefore inferior to that of inorganic scintillators[24]. Other examples of loaded organic scintillators are used for neutron detection. Liquid or plastic scintillators are seeded with an element

with a high cross section for neutrons such as boron, lithium or gadolinium. The secondary charged particles or gamma-rays produced by neutron-induced reactions are then detected directly in the scintillator.

2.3.2 Inorganic scintillators

Whereas the scintillation mechanism in organic materials is of molecular nature, it depends on the electronic band structure determined by the crystal lattice of inorganic materials. Absorption of energy can result in the elevation of an electron from its normal position in the valence band across the gap into the conduction band, leaving a hole in the valence band. In the case of a pure crystal, the return of the electron to the valence band with the emission of a photon is a very inefficient process and the typical gap widths result in photons with an energy too high with respect to the visible range. To enhance the probability of visible photon emission during de-excitation, small amounts of an impurity, called activators, are added to inorganic scintillators. These activators create sites in the lattice resulting in energy states in the forbidden gap through which the electron can de-excite back to the valence band. Because the energy is lower than that of the full forbidden gap, this transition gives rise to a visible photon and can be used for the scintillation process.

Inorganic scintillators are mainly crystals of alkali halides containing a small activator impurity like thallium (Tl). Non-alkali materials such as BGO (bismuth germanate) and GSO (gadolinium oxyorthosilicate) are commonly used for positron emission tomography (PET) and for detecting neutrons[25]. Cesium fluoride[26] (CsF) and lead tungstate[27] ($PbWO_4$) exhibit interesting properties for energy and time spectroscopy. The advantage of inorganic crystals over organic scintillators lies in their greater stopping power due to their higher density and higher atomic number. Among all the scintillators, they have the highest light outputs resulting in better energy resolution capabilities.

Scintillator glasses such as cerium-activated lithium or boron silicates are widely used for neutron detection[28]. Glass scintillators can also be used for beta and gamma-ray counting when severe environmental conditions, such as corrosive chemical environments or high temperatures, prevent the use of other scintillators. Their light output is quite low and their decay times range typically between 50 and 75 ns in an intermediate range between faster organics and slower crystalline inorganics.

Certain high-purity gases can also serve as useful scintillation detection media. These consist mainly of the noble gases xenon, krypton, argon and helium along with nitrogen. These scintillators have an extremely fast response. In the gas the atoms are individually excited and return to their ground states within about 1 ns. The emitted light is usually in the UV range and a wavelength shifter, such as diphenylstilbene (DPS) must be applied on the walls of the gas container in order to shift the light to a region where photodetectors are most efficient.

2.3.3 Radiation damage effects in scintillators

All scintillation materials suffer from radiation damage. The effects of radiation damage are most likely evidenced as a reduction in the transparency of the scintillator caused by the creation of color centres that absorb the scintillation light[29]. There can also be interferences with the processes that give rise to the emission of scintillation light itself and long-lived light emission in the form of phosphorescence can be induced.

The phenomena involved in the radiation damage process are complex, unpredictable and not well understood[4]. They depend on many parameters such as the nature of the radiation, the integrated dose, the dose rate[30], the atmosphere and temperature before, during and after the irradiation[31]. Post-irradiation annealing, or at least partial recovery, can be observed over periods of time ranging from few hours to days following the exposure. It is accelerated by the diffusion in the material of atmospheric oxygen and by elevated temperatures. Because of the many variables involved, it is difficult to quantify the exact dose expected to produce measurable damage under specific circumstances to the different types of scintillation materials[32]. Rough numbers and relative sensitivities show that the least resistance appear to be thallium-activated alkali halides for which exposures to 10 Gy can be significant. The most resistant seems to be GSO in which effects start appearing only at doses of the order of 10^6 Gy. The damage in the alkali halides was observed to be closely coupled with the presence of oxygen contamination leading to the formation of hydroxyl groups whereas in the oxide scintillators, the damage was found to be related to the structural defects such as oxygen vacancies in the crystal lattice.

Plastic scintillators and plastic scintillating fibres are widely used in particle physics where they can be exposed to high levels of radiation. Hence the degradation of their performances due to radiation damage has been extensively studied in the past[33;34;35;36;37]. This degradation is mainly caused by the creation of optical absorption centres which absorb light more strongly in the UV and blue region than at longer wavelengths. This

poorly understood effect appears as a reduction of both the light yield and the attenuation length[4]. Plastic scintillators typically degrade for cumulated doses of the order of 10^3-10^4 Gy[30;38]. Special formulations of plastic scintillators for increased radiation resistance can stand doses up to 10^5 Gy before exhibiting only a little decrease in their light output[39]. Observations have shown that liquid core scintillators tolerate an order of magnitude or higher doses before the same effects appear[40].

Since absorption centres induced by radiation tend to attenuate the blue end of the spectrum most severely and are less intrusive at longer wavelengths, the most reliable method of limiting radiation damage is to shift the emission spectra at every step to the longest possible wavelength. For example by using fluors with a large Stroke's shift.

2.4 Scintillation detectors

The fundamental elements of a scintillation detector are the scintillating material and the photodetector to which it is optically coupled either directly or via a light guide[41;42]. As radiation traverses the scintillator it excites the atoms and molecules of the scintillator causing light to be emitted. This light is transmitted to the photodetector, typically a photomultiplier (PMT), where it is converted into an electrical signal (see Fig. 2.3).

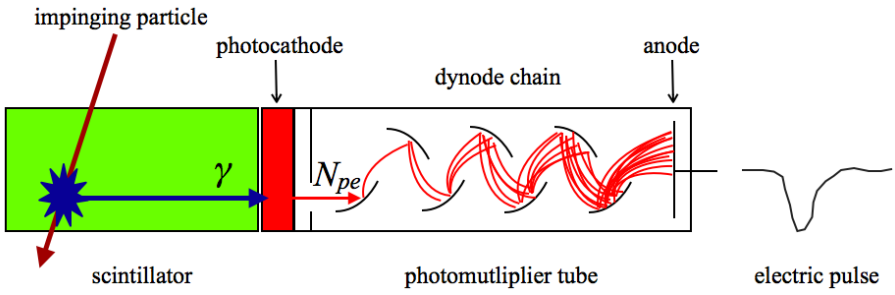

Figure 2.3: Scintillation detector assembly.

Plastic scintillators are the most widely used in detectors assemblies. Densities range from 1.03 to 1.20 g/cm^{-3} and typical photon yields are in the order of 1 photon per 100 eV of energy deposited[43]. A 1 cm thick scintillator traversed by a MIP will therefore yield approximately 2×10^4 photons. The resulting photoelectron signal and yield of a given scintillation detector will depend on the collection and transport efficiency of the optical package and the quantum efficiency of the photodetector. In the case of a PMT, the scintillation photons that reach the photocathode excite its electrons so that a number N_{pe} of photoelectrons are emitted in the vacuum tube (see Section 2.4.1).

These photoelectrons are accelerated and focused onto the first dynode where they are multiplied by means of secondary electron emission. This secondary emission is repeated at each of the successive dynodes. The multiplied secondary electrons emitted from the last dynode are finally collected by the anode and an electric pulse is transmitted to an external circuit. To read-out the light from bundles of scintillating fibres, position-sensitive photodetectors such as multi anode photomultiplier tubes (MAPMT) can be used, as described in Section 2.4.3. The photoelectrons are emitted from a region of the photocathode corresponding to a given fibre and they are focused into different dynode chains and anodes.

2.4.1 Photoelectric yield

The photoelectric yield[44] of a scintillator-photodetector assembly, expressed as the average number $\bar{N}_{pe}$ of photo-electrons per impinging particle, can be estimated as follows

$$\bar{N}_{pe} = N_{scint} \cdot \varepsilon_{coll} \cdot \varepsilon_{refl} \cdot \varepsilon_{att} \cdot \varepsilon_{in} \cdot \varepsilon_{Q_{eff}} \tag{2.3}$$

where:

- N_{scint} is the number of isotropically generated scintillation photons,
- ε_{coll} is the geometrical collection efficiency factor of the scintillator,
- ε_{refl} is the gain due to reflections on the opposite sides of the detector,
- ε_{att} is the transport efficiency due to optical absorption,
- ε_{in} is the transmission at the interface between the scintillator and the photodetector, and
- $\varepsilon_{Q_{eff}}$ is quantum efficiency of the photodetector.

The typical charge spectrum obtained with a scintillator-photodetector assembly is shown in Fig. 2.4. It can be fitted with the sum of a Gaussian G_{ped}, describing the pedestal, and the convolution of a Poisson distribution P_{det} with Gaussian terms G_{det} describing the detector's response

$$F(x) = G_{ped} + P_{det} \otimes G_{det} \tag{2.4}$$

The Poisson distribution P_{det} describes the fluctuations in the production of photoelectrons at the level of the photocathode for a given number of photons coming from the scintillator and the Gaussian term G_{det} describes the response of the read-out electronics to a given number of photoelectrons.

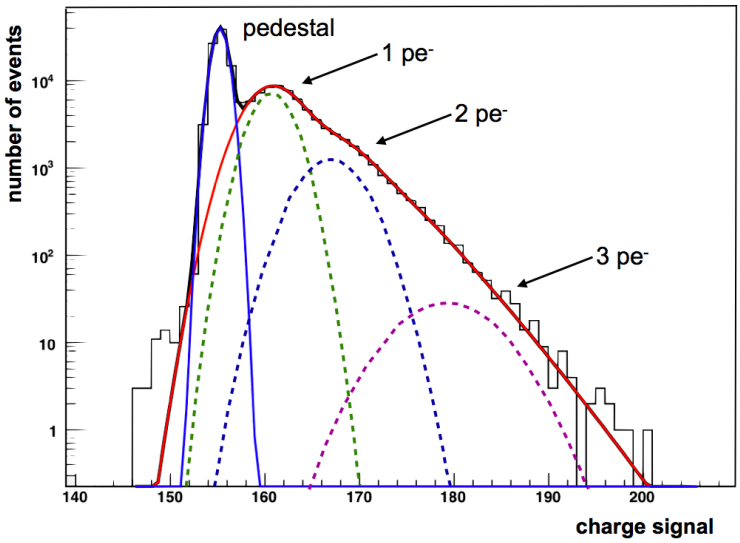

Figure 2.4: Fit of a typical spectrum obtained with a scintillation detector assembly. The pedestal is fitted with a Gaussian and the response of the scintillation-photodetector assembly is fitted with a Poissonian convoluted with Gaussians. The Gaussian distributions corresponding to the 1, 2, and 3 photoelectrons contributions are shown in dashed lines.

In more details the fit can be expressed as follows

$$F(x) = N_0 \cdot G\left(x, x_0, \sigma_0\right) + N_{sig} \cdot \sum_{N=1}^{\infty} \left(P\left(N, \bar{N}_{pe}\right) \cdot G\left(x, x_N, \sigma_N\right) \right) \tag{2.5}$$

where:

- N_0 is the number of pedestal counts,
- x_0 is the pedestal mean value,
- σ_0 is the sigma of the pedestal distribution,
- N_{sig} is the number of signal counts,
- $\bar{N}_{pe}$ is the average number of photoelectrons measured per event,
- $x_N = N \cdot x_1$ is the average number of counts above the pedestal, with x_1 being the number of counts for a single photoelectron, and

- σ_N is the standard deviation of the distribution of the photoelectron counts with $\sigma_N^2 = \sigma_0^2 + N \cdot \sigma_1^2$ and σ_1 being the standard deviation for a single photoelectron.

If one develops Eq. 2.5 it leads to

$$F(x) = N_0 \cdot \frac{1}{\sigma_0\sqrt{2\pi}} \cdot e^{-\frac{(x-x_0)^2}{2\sigma_0^2}} + N_{sig} \cdot \sum_{N=1}^{\infty} \left(\frac{\bar{N}_{pe}^N e^{-\bar{N}_{pe}}}{N!} \cdot \frac{1}{\sigma_N\sqrt{2\pi}} \cdot e^{-\frac{(x-x_N)^2}{2\sigma_N^2}} \right) \quad (2.6)$$

2.4.2 Detection efficiency

An average photoelectric yield of $\bar{N}_{pe}$ photoelectrons leads to a detection efficiency ε_{det} derived from

$$\varepsilon_{det} \approx 1 - P\left(0, \bar{N}_{pe}\right) = 1 - e^{-\bar{N}_{pe}} \quad (2.7)$$

where $P(0, \bar{N}_{pe}) = e^{-\bar{N}_{pe}}$ corresponds to the Poissonian probability to have zero photoelectrons when the average number is $\bar{N}_{pe}$. This estimate assumes that a single photoelectron can be detected with 100% efficiency by the read-out system.

2.4.3 Scintillating fibre detectors

A scintillating fibre consists of a core, in which the scintillation light is generated through an interaction with the incident radiation, surrounded by a cladding material with an index of refraction lower than the index of the core. Light rays that arrive at the core-cladding interface with an angle of incidence that is greater than the critical angle for total internal refraction (TIR) are guided inside the fibre.

Scintillating fibre detectors are usually read-out by photodetectors such as position-sensitive photomultiplier tubes[45;46], image intensifier tubes viewed by CCDs[47], avalanche photodiodes[48;49] (APD), Geiger-mode avalanche photodiodes[50;51] (GM-APD) also known as silicon photomultipliers (SiPM), and CMOS-based single photon avalanche diodes[52] (SPAD).

2.4.3.1 Plastic scintillating fibres

A typical configuration consists of fibres with a PS core, with an index of refraction $n_{core} = 1.59$, surrounded by a PMMA cladding with an index of refraction $n_{clad} = 1.49$ and only a few μm thick. For added light capture an additional cladding of fluorinated

PMMA with $n_{clad} = 1.42$ can be added. Typical dimensions of the fibres are 0.5 to 1 mm. The fraction of light that is guided along the fibre is known as the capture fraction and it amounts to about 6% for single-clad fibres and 10% for the double-clad fibres.

The number of photons produced by a MIP traversing a 1 mm fibre is of the order of 2000 of which only about 200 are captured. Approximately 95% of these photons are typically lost due to attenuation along the fibres in a large detector[4]. Scintillating fibres are often characterized by their attenuation length over which the light is attenuated by $1/e$ of the original value.

2.4.3.2 Liquid scintillator capillaries

A glass capillary tube filled with liquid organic scintillator can also function in much the same way as a scintillating fibre if there is a significant reduction in index of refraction from the liquid to the glass[53;54;55]. This approach benefits from the good light yield and fast decay time of liquid scintillators[56], similar to that of plastic scintillators. Furthermore liquid scintillators exhibit less susceptibility to radiation damage effects compared with plastics[40;57]. The excellent optical quality of the liquid-glass interface can have light losses as low as 10^{-6} per reflection[58] and capillaries with inner diameter as small as 20 μm can have attenuation length of up to 3 m[59].

Scintillating fibres are often grouped together to form ribbons or bundles and glass can also be fused together as bundles as shown in Fig. 2.5.

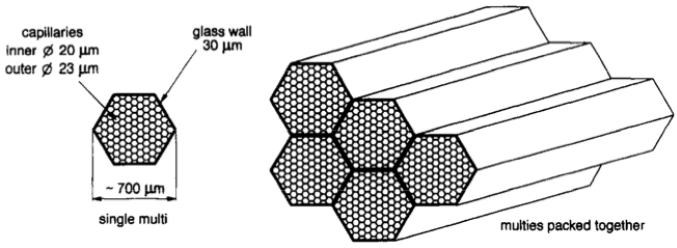

Figure 2.5: Glass capillaries fused into bundles and filled with liquid scintillator[47].

2.4.3.3 Scintillating glass fibres

Glass materials which are commonly used as scintillators can be easily drawn into small diameter fibres as small as 10 μm. A typical cerium activated glass scintillator will have an index of refraction of about 1.59. A cladding glass is then chosen with a lower refractive index, typically in the order of 1.51. If an extramural absorber is required it can be a coating of black glass or polymer material.

The energy transfer required from the glass matrix to the activator sites occurs over much smaller distances than in plastics and the drop in efficiency for small diameter plastic fibres is not observed in glass. The absolute scintillation efficiency of glasses is lower than that of plastics so the light yield is less and the decay time of 50-80 ns is substantially longer. Glass fibres incorporating ^{6}Li can be used in some specialized neutron detection applications. Glass fibres can also be fused into bundles or large diameter plates that have very different optical properties than bulk scintillators with the same outer dimensions. The scintillation light being confined in the individual fibre in which it originated, the loss of spatial resolution caused by the spread of light in the bulk scintillator is avoided. Such glass fibre plates have been used for X-ray imaging[60;61;62], particle tracking[63] and neutron imaging[64].

2.5 Applications of scintillation detectors

Scintillation detectors can be found in a wide variety of scientific and industrial applications. They are routinely used for tracking and calorimetry in HEP experiments, for diagnostic imaging and analysis in medicine, and also for many industrial and security applications such as oil-well logging and non-destructive measurements.

High energy physics In particle physics, scintillators find extensive application in fixed-target and collider experiments where they can be used for tracking, calorimetry, triggering, and time-of-flight measurements. Scintillating tracking detectors typically consist of many flat, parallel, plastic scintillators or fibres coupled to multi-channel photomultipliers. The usual information required from each scintillator is a simple yes or no in order to reconstruct the tracks of the particles. Scintillators are also used in calorimetry. Electromagnetic and hadron calorimeters often consist of plastic scintillator tiles interleaved with materials with high atomic number (high stopping power) such as lead, iron, and copper. Calorimeters can also be produced from scintillating fibres uniformly stacked through the high-Z material. Alternative constructions may use lead-glass blocks or inorganic scintillators, such as lead tungstate ($PbWO_4$), with high stopping powers and short decay times coupled directly to photomultipliers[27]. In HEP experiments, it is also important to obtain time-triggering information. This is usually done with long rods of very fast plastic scintillators observed from both ends by fast photomultipliers whose outputs are compared in time as well as in amplitude.

Medical field The information sought in most medical applications of scintillation detection is a clinically significant internal image of the body. Radioactively labelled substances are administered to the patient. These substances are chosen for their affinity to the specific organs or tissues to be studied. From the local radiation intensities registered by scintillation detectors, it is then possible to reconstruct images of the organs and tissues under investigation. A major application is single-photon emission computed tomography (SPECT), in which cross-sectional images of the body are generated by detectors rotating around the patient. Another significant application is positron emission tomography (PET). In this case, a positron-emitting isotope is administered to the patient and the body region under investigation is surrounded by rings of small scintillators, typically BGO or LSO, and photomultipliers. A computer reconstructs cross-sectional metabolic images based on the detection of the two coincident photons which are emitted at 180° from each other when a positron annihilates with an electron in the patient's body. Recently, miniaturized PET scanners have been used to study the influence of pharmaceuticals on rodents such as mice. Scintillating fibre trackers, identical to the ones used in HEP experiments, have successfully been transferred to hadrontherapy where they are used as beam monitors. This allows to precisely control the intensity and shape of the beam reaching the tumor in critical parts of the patient's body such as the eyes and the brain.

Analytical applications Scintillation counting permits to measure specific biochemical levels in body tissues and fluids with the aid of radioactive tracers. Liquid scintillation counting (LSC) and radio-immuno assay (RIA) are among the most widely used methods. The aim of LSC is generally to trace the pathways of specific substances in the body or to measure their tendency to concentrate in specific tissues or fluids. A quantity of the substance in question is labelled with a radioactive tracer. After it has been assimilated, a sample of the body tissue, or fluid, of interest is taken and the concentration of the labelled substance is determined by measuring its radioactivity. To detect such radiation it is necessary to incorporate the sample in the scintillation medium itself, hence the choice of a liquid. The scintillator is observed by two photomutlipliers. Whenever a scintillation is observed by both tubes in coincidence it is passed to a counter. RIA is a technique for measuring minute concentrations of substances, such as hormones, in biological fluids. Liquid samples, containing radioactive tracer, are inserted in wells dug in scintillators coupled to individual PMTs. The concentration of the substances under study contained in each samples are then simply obtained by scintillation counting.

Industrial and security applications Scintillation detectors have many industrial applications. They are used for non-destructive analysis, thickness and density measurement, oil-well logging, and homeland security. Two widely used methods in non-destructive analysis are activation and X-fluorescent analysis. In the first case the specimen is exposed to nuclear radiation so that its constituent elements become radioactive and can be identified and quantified by scintillation counting of their own radiation. X-fluorescent analysis is similar but it is based on the characteristic X-ray emission spectra of the elements constituting the specimen. The emission may be stimulated by bombardment with charged particles or irradiation with gamma rays or X-rays. Thickness and density measurements with scintillation detectors can be performed either by transmission or backscattering of ionizing radiation bombarded on a sample. In the first case, the scintillation detector is on the other side of the sample with respect to the source and it measures the transmitted radiation while in the latter, they stand on the same side and the scattered radiation is measure. In exploratory drilling, a bore-hole probe containing an ionizing source and a scintillation detector can aid in assessing the probability of hydrocarbon deposits. The detectors are shielded from the direct radiation of the source and responds only to scattering from the walls of the hole. By analyzing the count rate as the probe descends, information about the structure and composition of the ground can be gathered. As a last example of the many applications of scintillation detectors, one can mention homeland security. Several products have been introduced in the market making use of scintillation for the detection of potentially dangerous radioactive materials. These include scintillation counters for border security, freight terminals, harbors, nuclear sites, and HEP experimental areas. There are also variants of such detectors mounted on vehicles and hand-held units.

Chapter 3

Absolute Luminosity For ATLAS

This chapter gives on overview of the scintillating fibres tracking system proposed for the measurement of the absolute luminosity of the CERN LHC collider at the ATLAS interaction point. After outlining the requirements for this measurement, the design and concept of the scintillating fibre detectors inserted in roman pots located at 240 m from the interaction point are presented.

3.1 Introduction

New physics at the CERN Large Hadron Collider[65] (LHC) might manifest itself as deviations from the Standard Model predictions of cross sections. Therefore it is crucial to normalize their measurement. The uncertainty of the absolute luminosity is one of the main factors limiting the measurement precision. Traditionally, the absolute luminosity at hadron colliders was determined via elastic scattering of protons at small angles. This is also one of the approaches pursued by the ATLAS[66] (A Toroidal Large ApparatuS) experiment at the LHC (see Sections 3.2 and 3.3). The tracking system ALFA[67;68] (Absolute Luminosity For ATLAS) will measure elastic proton-proton (pp) scattering at such small angles that it becomes sensitive to the well-known electromagnetic amplitude (see Section 3.4). It is based on the scintillating fibre technology, as used in several high energy physics experiments before[69;70]. Fibre tracker modules will be inserted in Roman Pots above and below the LHC beam axis at a distance of 240 m on each side of the ATLAS interaction point (IP1) (see Section 3.5).

In addition to determining the absolute luminosity of the LHC at IP1, other interesting physics topics can be explored with the scattering data measured with the ALFA detectors.

3.2 The Large Hadron Collider

The Large Hadron Collider[65] (LHC) is a two-ring-superconducting-hadron accelerator and collider (see Fig. 3.1) installed in the existing 26.7 km tunnel that was constructed between 1984 and 1989 for the Large Electron-Positron Collider[71] (LEP). Its aim is to provide an insight in particle physics at the TeV scale and to investigate physics beyond the Standard Model (SM).

The LHC has two high luminosity experiments, ATLAS[66] (A Toroidal LHC ApparatuS) and CMS[72] (Compact Muon Solenoid), both aiming at a peak luminosity of 10^{34} $\mathrm{cm}^{-2}\mathrm{s}^{-1}$ for pp collisions at centre of mass energy E_{CM} up to 14 TeV. There are also two low luminosity experiments, LHCb[73] (LHC beauty) for B-physics and TOTEM[74] (Total Cross Section Elastic Scattering and Diffraction Dissociation at the LHC) for the detection of protons from elastic scattering at small angles. In addition to the proton beams, the LHC will also be operated with ion beams with one dedicated ion experiment ALICE[75] (A Large Ion Collider Experiment).

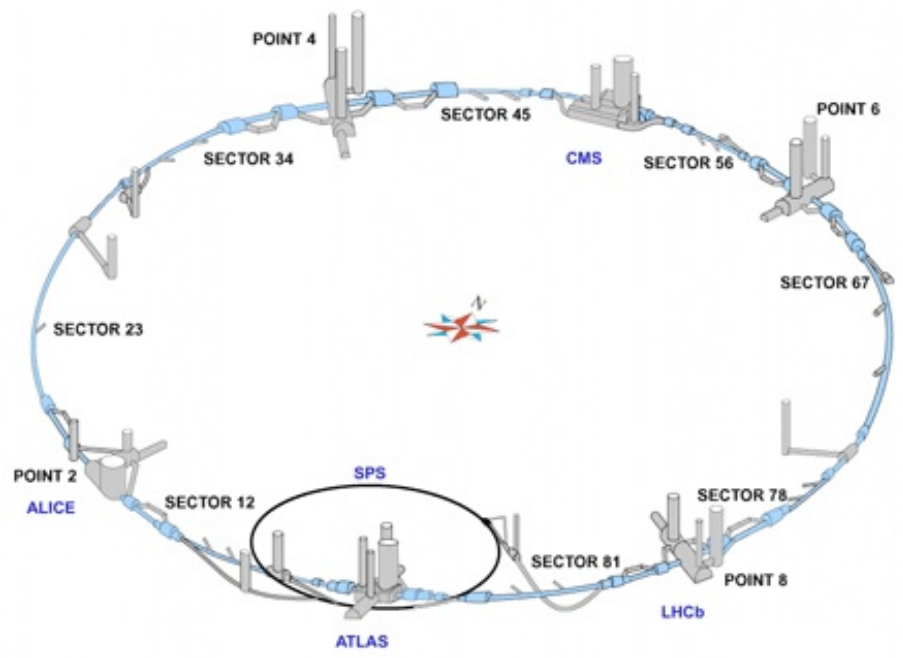

Figure 3.1: The Large Hadron Collider.

3.3 The ATLAS experiment

The ATLAS detector[66] is illustrated in Fig. 3.2. It is nominally forward-backward symmetric with respect to the LHC IP1. It provides a full ϕ coverage which extends to a high value of pseudorapity η. The pseudorapidity η is defined in terms of the polar angle θ as $\eta = -\ln\tan(\theta/2)$.

The magnet configuration comprises a thin superconducting solenoid surrounding the inner-detector cavity, and three large superconducting toroids (one barrel and two end-caps) arranged with an eight-fold azimuthal symmetry around the calorimeters. This fundamental choice has driven the design of the rest of the detector.

The inner detector is immersed in a 2 T solenoidal field. Pattern recognition, momentum and vertex measurements, and electron identification are achieved with a combination of discrete, high-resolution semiconductor pixel and strip detectors in the inner part of the tracking volume, and straw-tube tracking detectors with the capability to generate and detect transition radiation in its outer part.

High granularity liquid-argon (LAr) electromagnetic sampling calorimeters, with excellent performance in terms of energy and position resolution, cover the pseudorapidity range $|\eta| < 3.2$. The hadronic calorimetry in the range $|\eta| < 1.7$ is provided by a scintillator-tile calorimeter (TileCal), which is separated into a large barrel and two

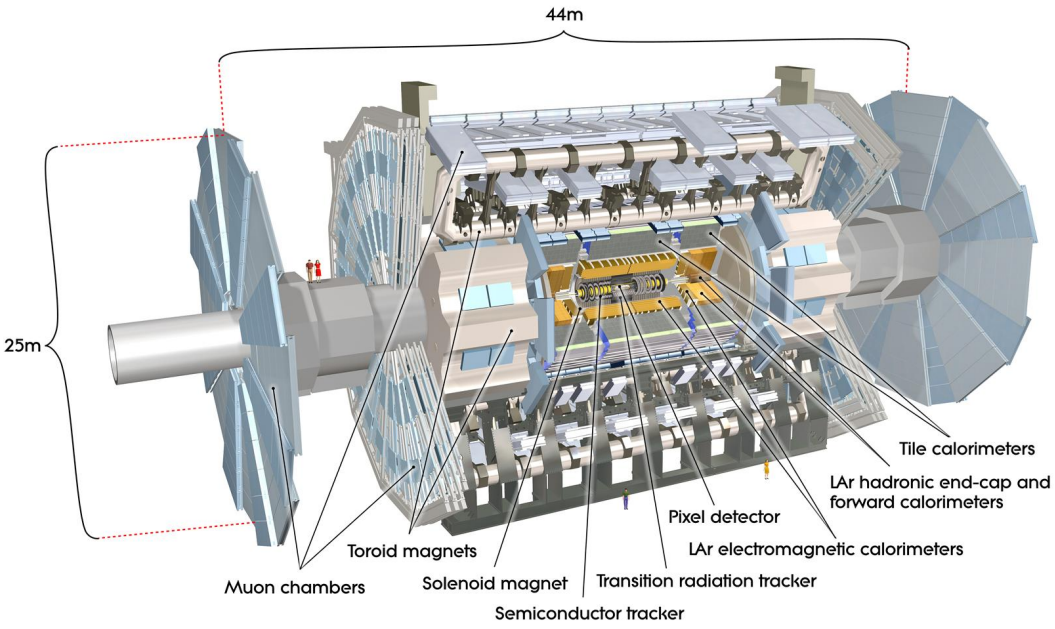

Figure 3.2: Cut-away view of the ATLAS detector. The dimensions of the detector are 25 m in height and 44 m in length. The overall weight of the detector is approximately 7000 tons.

smaller extended barrel cylinders, one on each side of the central barrel. In the end-caps ($|\eta| > 1.5$), LAr technology is also used for the hadronic calorimeters, matching the outer $|\eta|$ limits of end-cap electromagnetic calorimeters. The LAr forward calorimeters provide both electromagnetic and hadronic energy measurements, and extend the pseudorapidity coverage to $|\eta| = 4.9$.

The calorimeter is surrounded by the muon spectrometer. The air-core toroid system, with a long barrel and two inserted end-cap magnets, generates strong bending power in a large volume within a light and open structure. Multiple scattering effects are thereby minimised, and excellent muon momentum resolution is achieved with three layers of high precision tracking chambers. The muon instrumentation includes, as a key component, trigger chambers with timing resolution in the order of 1.5 to 4 ns. The muon spectrometer defines the overall dimensions of the ATLAS detector.

Three smaller detector systems[67;68;76] cover the forward regions on both sides of the ATLAS detector near the beam line, with the aim of measuring and monitoring the LHC luminosity, as well as providing physics measurements in the very forward regions. The main function of the first two systems is to determine the luminosity delivered to ATLAS. At ± 17 m from IP1 lies LUCID[67] (LUminosity measurement using Cherenkov Integrating Detector) providing coverage of $5.6 < |\eta| < 6.0$. It detects inelastic pp

scattering in the forward direction, and is the main online relative-luminosity monitor for ATLAS. The second detector is the absolute luminosity detector ALFA[68]. It consists of scintillating fibre trackers housed inside Roman Pots located at ±240 m from IP1 which are designed to approach as close as 1 mm to the beam. The third system is the Zero-Degree Calorimeter[76] (ZDC), its primary purpose is to detect forward neutrons in heavy-ion collisions. It is located at ±140 m from IP1. This corresponds to the location where the LHC beam-pipe is divided into two separate pipes. The ZDC modules consist of layers of alternating quartz rods and tungsten plates which will measure neutral particles at pseudorapidities $|\eta| \geq 8.2$.

Additional proton-tagging detectors are being considered at an even greater distance of about ±420 m from IP1[77]. These detectors, together with new radiation hard-detectors[78] at ±220 m are part of a possible upgrade program.

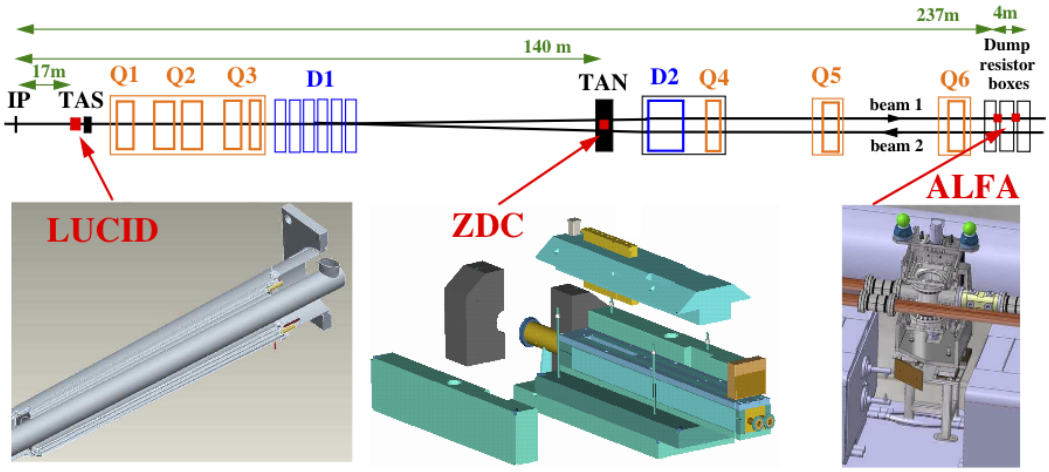

Figure 3.3: Placement of the forward detectors along the beam-line around IP1. At ±17 m from IP1 lies the luminosity monitor LUCID based on Cherenkov tubes, at ±140 m is a ZDC for detecting photons and neutrons mainly in heavy ion collisions, and at ±240 m precision tracking detectors (ALFA) in roman pots for the measurement of elastic scattering at very small angles for total cross section determination and absolute luminosity measurement.

The *pp* interaction rate at the design luminosity of 10^{34} cm^{-2}s^{-1} is approximately 1 GHz, while the event data recording[79], based on technology and resource limitations, is limited to about 200 Hz. This requires an overall rejection factor of 5×10^6 against minimum-bias processes while maintaining maximum efficiency for the new physics. The trigger system has three distinct levels: L1, L2, and the event filter. Each trigger level refines the decisions made at the previous level and, where necessary, applies additional selection criteria. The Level-1 (L1) trigger system uses a subset of the total detector information to make a decision on whether or not to continue processing an

event, reducing the data rate to approximately 75 kHz. The subsequent two levels, collectively known as the high-level trigger, are the Level-2 (L2) trigger and the event filter. They provide the reduction to a final data-taking rate of approximately 200 Hz.

3.4 Luminosity measurement in ATLAS

ATLAS has two dedicated luminosity detectors. The Roman Pot detector ALFA instruments the forward region around 240 m to measure small-angle elastic scattering and determine the absolute luminosity while the Cherenkov counter LUCID monitors the relative luminosity over several orders of magnitude by detecting inelastic pp scattering in the forward direction[80]. It provides both a measure of the integrated luminosity and online monitoring of the instantaneous luminosity and beam conditions.

The ALFA[68] system will measure the absolute luminosity via Coulomb scattering in dedicated luminosity runs to calibrate the instantaneous luminosity measurements performed by LUCID[67]. The luminosity calibration will be obtained from the measurement of the t-spectrum* down to scattering angles of the order of 3.5 μrad covering the rise of the spectrum induced by Coulomb interaction, from which the absolute luminosity is extracted independent of the total cross section using the optical theorem (see Appendix A).

The rate of elastic scattering is linked to the total interaction rate through the optical theorem, which states that the total cross section σ_{tot} is directly proportional to the imaginary part of the forward elastic scattering amplitude extrapolated to zero momentum transfer squared $-t$. At small values of $-t$, $-t = (p\theta)^2$, with p being the beam momentum and θ the forward scattering angle:

$$\sigma_{tot} = 4\pi \cdot Im\left(f_{el}\left(0\right)\right) \tag{3.1}$$

This implies that a measurement of elastic scattering in the forward direction will always provide information on the luminosity. This fact can be used in several ways. By measuring the total interaction rate R_{tot} and the elastic rate $dR_{el}/dt|_{t=0}$ in the forward direction simultaneously, both the luminosity L and the total cross section σ_{tot} can be determined. This method is followed by the TOTEM[74] collaboration to determine the LHC luminosity at the CMS[72] interaction point (IP5). It requires a precise measurement of the inelastic rate with good coverage in $|\eta|$. To make an accurate extrapolation over the full phase-space an $|\eta|$-coverage up to 7-8 is needed. The ATLAS

* $-t = (p \cdot sin\theta)^2$

forward coverage is not good enough for this purpose. Instead ATLAS intends to follow a different approach consisting in measuring elastic scattering down to such small t-values that the cross section becomes sensitive to the electromagnetic amplitude via the Coulomb interference term. If the Coulomb region can be reached an additional constraint is available from the well-known electromagnetic amplitude as can be seen from Eq. 3.2 that describes elastic scattering at small t-values:

$$\frac{dN}{dt} = L\pi \left(f_C + f_N\right)^2 \approx L\pi \left(\frac{2a_{EM}}{|t|} + \frac{\sigma_{tot}}{4\pi}\left(i+\rho\right)e^{-\frac{b|t|}{2}}\right)^2 \tag{3.2}$$

where the first term f_C corresponds to the Coulomb amplitude and the second f_N to the strong interaction amplitude. Using this additional constraint together with the optical theorem allows the determination of both the luminosity and the total cross section without a measurement of the inelastic rate.

This method was used by the UA4 collaboration at the CERN $Sp\bar{p}S$ where a precision of 3% on the absolute luminosity was achieved[81]. For ATLAS, such a precision would be adequate for most analyses. At the LHC nominal energy of 7 TeV the strong amplitude is expected to equal the electromagnetic amplitude to a scattering angle of 3.5 μrad whereas at the $Sp\bar{p}S$ collider the Coulomb region was reached at scattering angles of 120 μrad. The need to reach small scattering angles imposes very stringent requirements on the beam optics and the beam conditions, as well as on the detectors themselves.

3.4.1 Requirements on the beam

The calibration of the absolute luminosity from elastic scattering requires a special optics with a large β^* and a betatron phase advance yielding parallel-to-point focusing. As shown in Fig. 3.4, such a parallel-to-point focusing optics allows to reconstruct the scattering angle θ_y^* at the interaction point by measuring the transversal displacement at the detector plane y_{det}. The scattering angle allows then to reconstruct the t-value required to determine the luminosity if the Coulomb interference region is reached (see Section A.2.3). The minimal t-value reachable depends essentially on three parameters; the normalized emittance of the beam ε_N, the beta value at the interaction point β^* and the normalized distance between the sensitive part of the detector and the beam axis k

$$t_{min} \propto k^2 \varepsilon_N / \beta^* \tag{3.3}$$

The normalized distance k refers to the distance expressed in units of rms size of the beam spot at the detector σ_d.

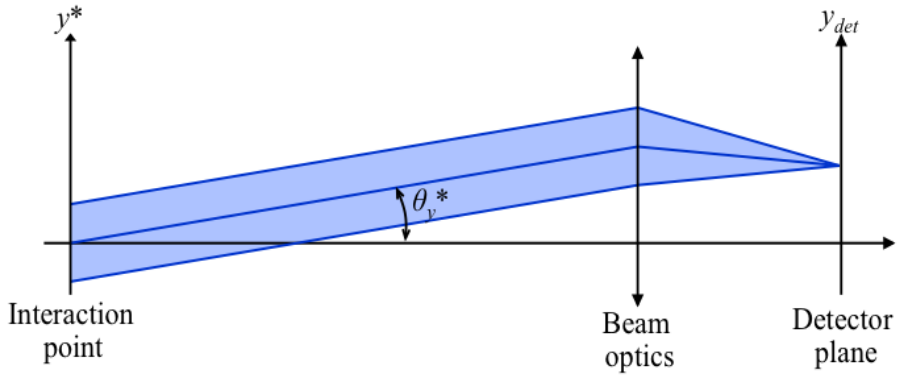

Figure 3.4: Parallel-to-point focusing optics.

The required beam conditions allow only for a running at very low luminosity around 10^{27} cm^{-2}s^{-1}. Given the large cross section of about 30 mb in a week of running sufficient statistics is accumulated. During that period, LUCID will also take data and its integrated rate will be calibrated to the measured luminosity.

3.4.2 Requirements on the detector

The quality of the luminosity measurements depends on the performance of the detectors. With parallel-to-point optics, the distance from the beam axis at the detector is proportional to the scattering angle at the interaction point. A given beam divergence translates to a certain beam spot size at the detector position σ_d and in order for the measurement not to be limited by the detector, its spatial resolution should be significantly smaller than σ_d. The beam spot size with the proposed optics is in the order of 130 μm. A spatial resolution in the order of 30 μm is considered adequate. Moreover, to remove background beam-gas and beam-wall interactions, it is necessary to measure the direction of the protons. With a lever arm of about 4 m between adjacent pots, a spatial resolution in the order of 30 μm is considered sufficient.

The minimum t-value t_{min} is determined by the distance of closest approach of the detector to the beam centre. It is therefore of crucial importance to minimize the dead space at the edge of the detector (*i.e.* the size of the insensitive region of the detector and the amount of material between beam vacuum and detector edge). In order to approach the beam at mm distance the maximum insensitive region at the edge of the detector should be in the order of 100 μm. Outside the dead space, the efficiency of the detector should be close to 100% with little variation as a function of the position.

In addition to the dead space of the detector, one also has to consider the thickness of the window that separates the detector from the ultra high vacuum of the machine. Minimizing the thickness of this window may require that the detectors work in a secondary vacuum.

A precise alignment of the detectors relative to each other is of great importance for measurements at small t-values. Front and back parts of the same telescope can be aligned using tracks from elastic scattering events. Similarly, elastic events can be used to align the opposing telescopes on each side of the interaction point. However it is not possible to align the top and bottom detectors using tracks. This relative alignment is of outmost importance because it sets the angular scale and thus the t-scale. A 10 μm position error at a distance of 1 mm from the beam implies a 1% error in the angular scale which in turn means a 2% error in the t-scale and translates to a 2% error in $d\sigma/dt$[82]. The two detectors can be aligned precisely relative to each other by using halo tracks if an overlap region is provided outside of the beam area.

For normal LHC operation at a luminosity of 10^{34} cm^{-2}s^{-1} and β^*= 0.5 m, calculations indicate accumulated dose levels up to 10^5-10^6 Gy/yr at a distance of 15 σ_d from the beam axis and 215 m away from IP1[68]. These calculations only take into account the contribution from the interactions at the interaction point, which dominates at high luminosity. This contribution can thus be scaled as the luminosity. Scaling down to a luminosity of 10^{27} cm^{-2}s^{-1} gives accumulated doses of 0.01-0.1 Gy/yr. Here one should further note that a realistic running scenario for elastic scattering is of the order of one week. There is also a contribution to the radiation from the beam halo in the order of 10-100 Gy/yr[68]. Thus, the halo contribution dominates completely and a total radiation hardness up to 100 Gy/yr is sufficient.

The magnetic field at the location of the luminosity detectors is generated by the terminals of the LHC dump resistors only during discharge when the detectors will not be operating. Measurements have been performed to determine the strength of the field[83]. Peak values up to 90 G can be reached during an energy extraction. They will immediately decay and disappear after 6 minutes maximum. During the resistors' dumps no data will be taken and during normal operation the magnetic field will be negligible. The magnetic field interference should thus not be a problem at the location of the detectors.

For detectors and electronics operating close to the beam the electromagnetic radiation from the circulating bunches induces pick-up noise. Thus it is important to have detectors with low sensitivity to the electromagnetic pick-up or to install adequate

electromagnetic shield. In the latter case the shielding contributes to the dead space between the beam and the sensitive part of the detector and will limit t_{min}.

3.5 The ALFA system

A set of tracking detectors based on plastic scintillating fibres fulfill the requirements in a simple and cost effective way. The ALFA scintillating fibre trackers are located 240 m on each side of IP1 (see Fig. 3.5). Unlike other detectors, they are not fixed relative to the beam. At beam injection, the ALFA detectors are in a withdrawn position far from the beam. After the beam has stabilized, the detectors are moved close to the beam for data taking. The device allowing the independent movement of the top and bottom pots is called a roman pot unit. Two roman pot units separated by a distance of 4 m are installed at each side of the interaction point. The complete ALFA system thus comprises in total 4 separate units and a total of 8 pots. The space for the roman pot units are limited by dump resistor boxes (DQR) that are necessary for dumping the current of the main magnets in case of quenches.

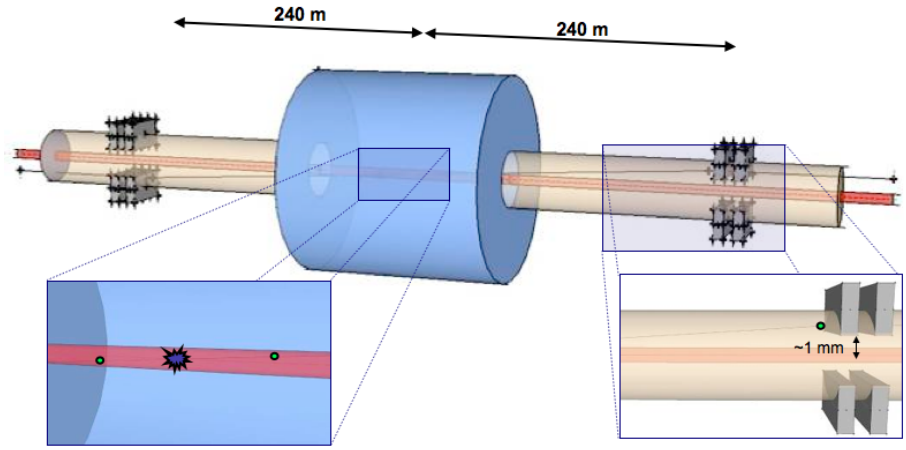

Figure 3.5: Luminosity measurement of the LHC at the ATLAS experiment with roman pot detectors located 240 m away from IP1.

As shown in Fig. 3.6 the trackers are inserted in roman pots (see Section 3.5.1) together with a set of overlap detectors (OD) that are also scintillating fibre trackers that reconstruct only the vertical coordinate of beam halo particles for the precise relative alignment of the top and bottom pot (see Section 3.5.3). Trigger scintillators define the active areas of the tracker and the ODs (see Section 3.5.4). The baseline fibres of the ALFA trackers and of the overlap detectors are coated with an Al film to reduce light losses and optical cross-talk. They are routed inside the roman pot to fibre connectors

and coupled to the pixels of MAPMTs (see Section 3.5.5). The fibre connectors are inside the vacuum flange that closes the roman pot and the MAPMTs are inside a mu-metal shield. The very compact front-end electronics is mounted directly on the back of the MAPMT (see Section 3.5.6).

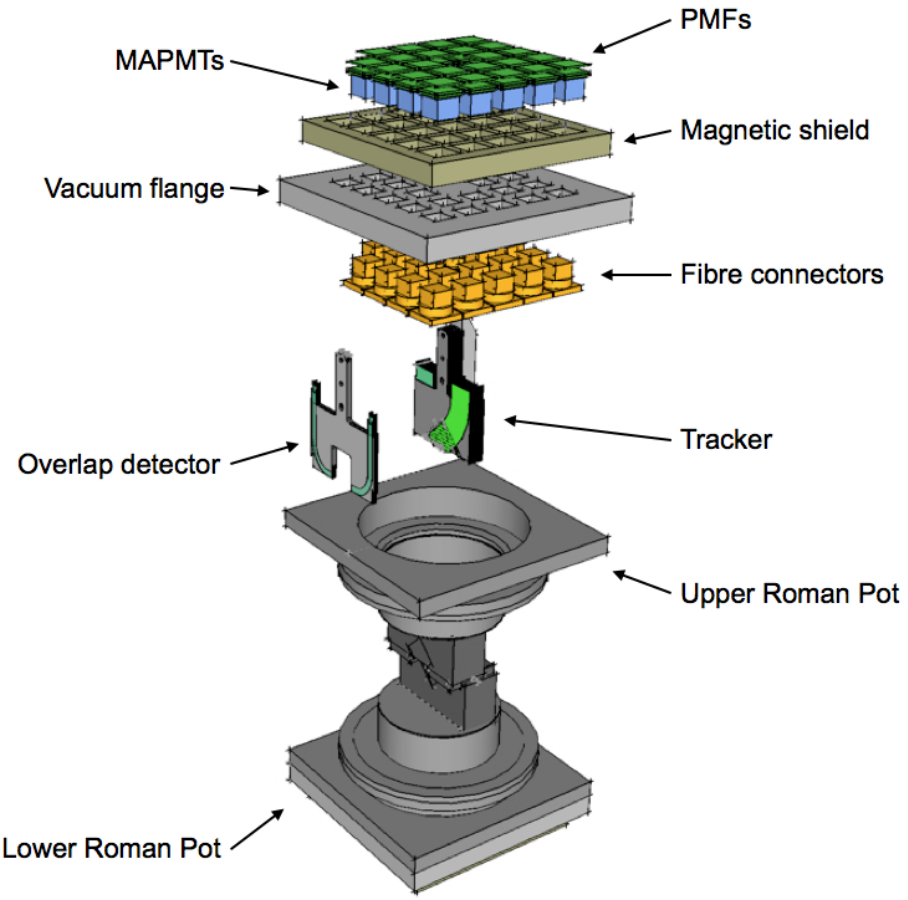

Figure 3.6: Exploded view of the top pot of one detector unit of the ALFA system. From bottom to top one sees the Roman Pot, the overlap detector and the tracker, the fibre connectors, the vacuum flange, the magnetic shield and the MAPMTs with the PMFs. Not shown on the drawing are the trigger scintillator tiles and the scintillating fibres routed from the detectors' plates to the connectors.

3.5.1 Roman pots

The ALFA detectors will approach very close to the LHC beam using the Roman Pot technique. It originates from the CERN-Rome group that invented this technique in the early 70's to study elastic scattering at the ISR[84]. They were the first to use pots inserted in the beam pipe to bring detectors close to the beam axis. The Roman Pots are vessels, which are separated from the machine vacuum and equipped with bellows that allow the pots to approach the beam (see Fig. 3.7). The Roman Pot technique

has been successfully used for measurements very close to the circulating beams in a number of experiments at different accelerators. It was used by UA4[81;85;86] at CERN when the $Sp\bar{p}S$ was used as a collider and later Roman Pots have been installed at the Tevatron[87;88;89], in RHIC[90] and in HERA[91;92]. In the LHC this technique is used by ATLAS[66] and TOTEM[74]. It allows approaching the ALFA tracking detectors at about 10 σ (*i.e.* ∼1 mm) from the circulating beams as shown in Fig. 3.7b. It will also move the pots away from the beam, at about 45 mm from the beam axis, in garage position (see Fig. 3.7a) during the filling periods because the LHC beam is bigger during injection.

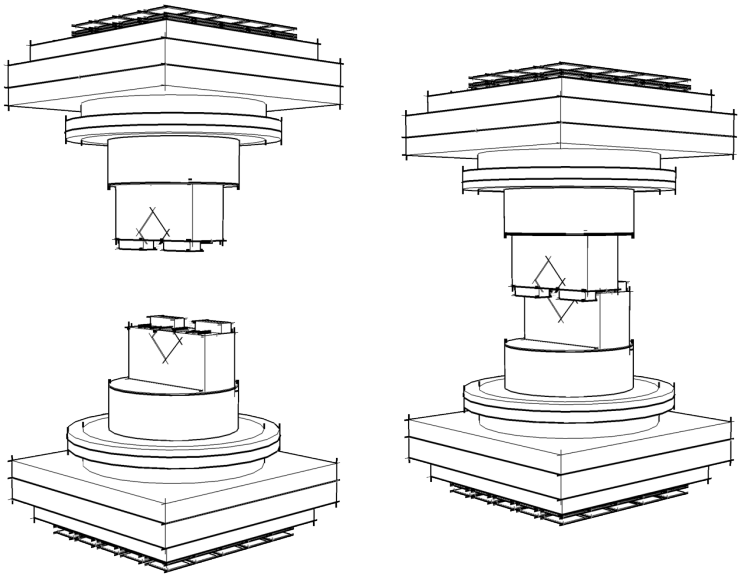

(a) **(b)**

Figure 3.7: Roman pots in garage position (a) at about 45 mm from the beam and (b) in working position at approximately 1 mm from the beam axis.

3.5.2 Tracking detectors

The design of the ALFA tracking detectors comprises plastic scintillating fibres of square cross section (0.5×0.5 mm^2) arranged in UV, or stereo, geometry (see Fig. 3.8). Two layers of 64 fibres are glued on each side of a substrate with a relative angle of 90°. The U fibres are positioned on the front of the plate at an angle of 45° while the V fibres stand on the backside with an angle of -45°. In order to approach the beam at very small distances, some fibres are cut at 45° to create a virtually edgeless detector. The active area of the tracker is limited to the overlap region of the fibres and it is defined by the coincidence of two plastic trigger scintillators placed in front of the detector (see

Section 3.5.4). It has a diamond shape and is somewhat smaller than 32 × 32 mm^2 due to the way the fibres are cut close to the beam.

A spatial resolution better than the 30 μm required for the elastic scattering measurement (Section 3.4.2), 10 plates of fibres are horizontally staggered in depth by multiples of a tenth of the effective fibre pitch (*i.e.* 500 μm / 10 × $\sqrt{2}$ = 70.7 μm). This pitch leads to an ultimate spatial resolution in x and y, ignoring any geometrical imperfections, of the order of 14.4 μm (= 50 μm / $\sqrt{12}$). The staggering of multiple fibres overlapping in the particle path increases the spatial resolution and it also guarantees a uniform detection efficiency.

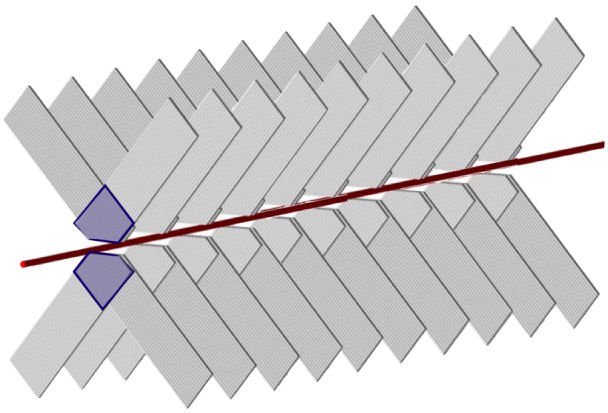

Figure 3.8: Principle of a scintillating fibre detector with 10 planes in UV geometry above the beam and 10 planes below. Each plane consists of 64 fibres at an angle of 45◦ and 64 fibres at -45◦. The active area is limited to the overlap region of the fibres.

3.5.3 Overlap detectors

The vertical distance between the upper and lower roman pot of a given station will be determined by so-called overlap detectors[82] (OD) which are also scintillating fibre trackers reconstructing only the vertical position of particle tracks. They are housed in special extrusions at the bottom of the roman pots. When the pots approach the beam axis the extrusions overlap (see Fig. 3.7b) and the relative vertical distance d between the two pots is derived from the averaged difference between the position of the hit fibres from the two overlap detectors

$$d = \frac{1}{N}\sum_{i=1}^{N}(y_{OD2,i} - y_{OD1,i}) \tag{3.4}$$

where N is the total number of hits, $y_{OD1,i}$ and $y_{OD2,i}$ are the positions of the fibres hit on the first overlap detector OD1 in one pot and on the second overlap detector

OD2 in the other pot for each event i. The precision of this measurement is obtained by accumulating large statistical samples[82].

Two ODs instrument each pot on both sides (left and right) of the main tracker (see Fig. C.14). They consist of 3 planes of 30 horizontal fibres of the same type of the trackers staggered by multiples of a third of the effective fibre pitch (*i.e.* 500 μm / 3 = 166.7 μm). This pitch leads to an ultimate spatial resolution in y of the order of 48.1 μm (= 166.7 μm / $\sqrt{12}$). Their active area is defined by a 6 $\times$ 15 mm^2 trigger scintillator (see Section 3.5.4). The inner dimensions of the roman pot limits the space available for the routing of the fibres from the detection area at the bottom of the pots to the MAPMTs at the top. For this reason the fibres have to be bent to very small radiuses. The stack of 30 fibres is split in two, 15 fibres are glued on one side of a support plate and the 15 others are glued on the backside. With this configuration the bending radiuses of the fibres in each stack are maximised, ranging from 22.5 to 37.5 mm.

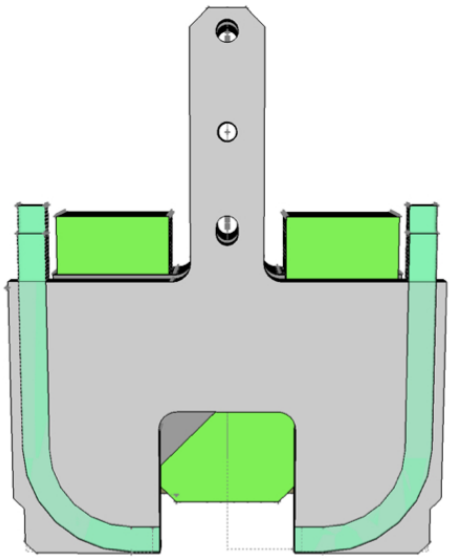

Figure 3.9: Overlap detectors in front of the main ALFA tracker. Only the lower half of the vertical stack of fibres are visible. To keep the bending radiuses as large as possible 15 fibres are glued on the front side of the plate and the other 15 are glued on the backside.

3.5.4 Trigger scintillators

The active areas of the ALFA tracking detectors are defined by two trigger counters in coincidence for the main detector and two independent counters for the overlap

detectors. The trigger tiles consist of plastic scintillator tiles coupled to bundles of plastic optical fibres to guide the light to single channel PMTs (see Section 3.5.5).

The trigger counter tiles of the main tracking detector consist of 3 mm thick diamond-shaped plastic scintillators (EJ-200 by Eljen Technology) with a side length of 32 mm and a height of 31 mm matching the overlap area of the 2 × 64 fibres of the tracking detector. They require a very uniform detection efficiency in order not to bias the measurement. The trigger tiles of the overlap detectors consist of 3 mm thick rectangular plastic scintillators with an area of 6 × 15 mm^2. The precise relative position reconstruction between two pots from a station with the overlap detectors is obtained by accumulating large samples of halo particles. This measurement is less sensitive to the trigger efficiency.

3.5.5 Photodetectors

The large number of scintillating fibres of the main tracker and overlap detectors require about 1500 read-out channels per pot. MAPMTs represent a well established commercially available and robust technology used in numerous high energy physics (HEP) experiments[93;94;95;96;97;98], astrophysics detectors[99] and space applications[100;101;102]. The baseline MAPMT selected for the ALFA detectors is the Hamamatsu R7600-00-M64 with 64 channels. A single MAPMT is used to read-out all the 64 fibres of a single layer of the tracker and the 60 fibres from the two layers of a single plate of the overlap detectors. In total 20 MAPMTS are required for all the fibres of the 10 plates with 2 layers of 64 fibres of the main tracker and 3 MAPMTS for the 3 plates with 60 fibres each of the overlap detectors. The 23 MAPMTs required to read-out all the scintillating fibres from the detectors in one roman pot are arranged in a 5 × 5 grid defined by a moulded epoxy which contains a mu-metal structures acting as a magnetic shield for the photodetectors. The central position of the grid does not house any MAPMT because it corresponds to the location where the fibre plates are connected to the baseplate of the pot through a metallic arm. The other unused slot houses the 4 single channel PMTs (R7400 by Hamamatsu) for the 4 trigger counters (see Section 3.5.4).

Even though SiPMs are a very appealing alternative for reading out scintillating fibres, they were not commercialized at the time of the design of the ALFA system. Nevertheless their development is still closely followed for future upgrades and the first single channel devices commercialized by Hamamatsu were tested at CERN and used to study irradiated scintillating fibres[103] (see Section 4.2.3).

3.5.6 Read-out electronics

In order to reconstruct the tracks in the fibre detector, the knowledge of the fibre hit is sufficient, as long as the fraction of cross-talk and induced noise are small. The average detected signal for a proton traversing a 0.5 mm scintillating fibre read-out by an MAPMT channel of the ALFA detector is about 4 photoelectrons. The 10 dynode stages of the MAPMT R7600-00-M64 lead to a gain of about 10^6 at a bias voltage in the order of 1 kV which in turns produces output signals of about 0.5 pC. The gain uniformity between the 64 channels is rather limited and variations up to a factor 3 are observed. Moreover the gain between two MAPMTs can also vary within a factor 2.

Each MAPMT is coupled to a dedicated photomultiplier front-end electronics[104] (PMF) module which performs the signal processing for each fibre. Due to space limitations the PMF is very compact. It consists of three PCBs and it is mounted directly on top of the MAPMT. The first board provides the high voltage distribution to the dynodes of the MAPMT. A socket adaptor board is plugged on top of the HV board to redistribute the signals to the third board which contains the MAROC chip[105] (Multi-Anode Read-out Chip) and an FPGA called ALFA-R[106] (ALFA read-out). The MAROC chip contains variable gain amplifiers to correct for the MAPMT non-uniformity and transmits binary information to the ALFA-R which stores it in a pipeline until it receives a trigger signal. The data is the sent to the RP mother-board which formats it and sends it to the common ATLAS read-out system[79] (see Section 3.3).

3.6 Conclusions and outlook

The ALFA system consists of scintillating fibre trackers approaching the beam within 1 mm. Elastic and diffractive protons which are not in the beam pass through the fibres of the trackers, which measure the distance of these protons to the beam. This is primarily to determine the absolute luminosity in ATLAS, but also other physics studies are foreseen, such as measuring the total pp cross section measuring elastic scattering parameters and, potentially, also to tag protons from diffractive studies. For a maximum precision in the luminosity measurement, the goal is to measure elastic scattering in the Coulomb interference region, which requires a measurement of scattering angles down to approximately 3.5 μrad. To reach such small angles the LHC has to run at low luminosities with special high β^*-optics.

The operation of the ALFA detectors in roman pots very close to the LHC beam will provide useful experience for future program of forward physics at high LHC luminos-

ity[77;107]. The experience achieved by operating the ALFA roman pot detectors will be valuable for learning about the possibilities and difficulties in working close to the LHC beam. This will allow to later extend the physics program by placing additional detectors in suitable positions in the LHC lattice in order to increase the measurable kinetical range of the forward protons.

It should be noted that beyond the purpose of luminosity determination, running the ALFA detector will also provide precious knowledge of the beam conditions and gain of experience on the operation of forward detectors close to the beam, relevant for future detectors aiming for the observation of hard central diffraction. In addition to determining the luminosity, the measured t-spectrum will provide fundamental soft physics parameters like the total cross section σ_{tot}, the nuclear slope B and the ρ-parameter. In a later stage, the physics program could be extended to a broader program including a variety of aspects of diffraction and diffractive dissociation to be measured with the nominal luminosity and in conjunction with the main detector. Such an extended program at high luminosity would require considerably more measuring Roman Pots stations and different requirements on the detectors.

Chapter 4

Scintillating fibre detectors

This chapter presents the studies performed on plastic scintillating fibres in terms of light yield, radiation resistance and minimum bending radiuses. The beam test experiments conducted on prototype scintillating fibre detectors are described with an emphasis on the results validating the design of the ALFA trackers and overlap detectors. The construction of the detectors is presented and the methodology to bend fibres to very small radiuses for the overlap detectors is described.

4.1 Introduction

The design of the ALFA trackers and overlap detectors requires plastic scintillating fibres with a square cross section to be routed over short distances with relatively small curvatures within the limited space available in the roman pots. The basic properties of different types of fibres were investigated in a set of laboratory and beam tests (see Section 4.2). Radiation hardness studies of the fibres were also performed[103] to demonstrate their resistance up to the doses expected at the ALFA location and a procedure to bend them to small radiuses for the overlap detectors was developed[108]. The satisfactory results obtained with the fibres under study led to the fabrication of various prototype detectors which have been characterized in a series of beam test experiments (see Section 4.3). The focus of the first test beam[109] which took place in 2005 at DESY was on characterizing the key parameters of the detector concept like the light yield of the fibres, the cross-talk effects on various levels, the detection efficiencies of the fibres and of the detector, the track reconstruction efficiency, the spatial resolution and the edge sensitivity. The main purpose of the second test beam[110] performed at CERN in 2006 was to confirm the results with larger fibre detectors and to validate the fibre tracker together with the proposed front-end electronics and read-out system as close as possible to the final implementation. In addition the proposed vertical alignment method with overlap detectors was validated (see Section 4.4). In 2007, an irradiation campaign at CERN was dedicated to determining the radiation resistance of plastic scintillating fibres[103] (see Section 4.2.3) and a test beam was pursued at DESY in order to study different trigger configurations[111] (see Section 4.5). A magnetic shield for MAPMTs was developed[112] (see Section 4.6) and implemented to the first full scale detector which was tested in 2008 in the H8 beam line at CERN[113] (see Section 4.7).

4.2 Plastic scintillating fibres

Five types of plastic scintillating fibres with a square cross section (see Table 4.1) have been studied in a series of laboratory and beam tests to determine the best choice for the fabrication of the ALFA trackers and overlap detectors. Individual fibres were characterized in terms of light yield, attenuation and surface quality of the end cuts by exciting them with radioactive and UV light sources (see Section 4.2.1). Beam test experiments were carried on bundles of aluminum coated fibres read-out by an MAPMT to get a better understanding of the photoelectric yield of such an assembly and to estimate the cross-talk (see Section 4.2.2). A test beam was dedicated to irradiating the

fibres at different doses and measuring their light yield as a function of the accumulated dose to determine their detection efficiency at the levels of radiation expected at the location of the ALFA detectors (see Section 4.2.3). The routing of the fibres of the overlap detectors require small bending radiuses beyond which they are mechanically and optically degraded. A methodology to bend square plastic scintillating fibres to very small radiuses was developed and successfully implemented to Al-coated fibres (see Section 4.2.4). The results obtained during the characterization of the fibres led to the selection of the fibre SCSF-78-SJ manufactured by Kuraray as the baseline fibre for the ALFA trackers and overlap detectors (see Section 4.2.5).

Table 4.1: Characteristics and expected photoelectric yield of the plastic scintillating with square cross section investigated. The SCSF fibres are produced by Kuraray and the BCF-12 belong to the Bicron 612 series. All the fibres have a single cladding except the BCF-12MC which has a double cladding.

	λ_{max}	Cross section	Cladding	45°-cut		90°-cut	
Fibre type	(nm)	(mm^2)	(μm)	N_{pe}	ε_{det} (%)	N_{pe}	ε_{det} (%)
SCSF-78-SJ	430	0.5 × 0.5	10	3.89	98	4.33	99
SCSF-78-SJ-1	430	1.0 × 1.0	20	7.78	100	8.66	100
SCSF-3HF	530	0.5 × 0.5	10	1.95	86	2.17	89
BCF-12SC	430	0.5 × 0.5	20	3.73	98	4.15	98
BCF-12MC	430	0.5 × 0.5	30	6.21	100	6.91	100

4.2.1 Preliminary studies

Prior to the design and construction of the detector prototypes a number of laboratory tests were performed to characterize a series of different scintillating fibres in terms of light yield[114], attenuation length[115] and surface quality of the end cuts[116]. The fibres of interest are plastic scintillating fibres with a square cross section of 0.5 × 0.5 mm^2 and 1 × 1 mm^2 manufactured by Bicron and Kuraray. These fibres have a core of polystyrene and a cladding of PMMA (see Table 4.1). To determine their light yield they were excited with electrons from a ^{90}Sr radioactive source, considered as MIPs (see Appendix B), and read-out with an MAPMT (H7546 by Hamamatsu). It was measured to be of the order of 3.2 photoelectrons for the Kuraray SCSF78 0.5 mm, 3.6 photoelectrons for the Kuraray SCSF78 1 mm, 4.4 photoelectrons for the Bicron BC612 0.5 mm, and 3.4 photoelectrons for the Bicron BC612MC 0.5 mm. The light attenuation length was measured by exciting the fibre with a monochromatic UV light source at 350 nm at a defined distance from the photodetector. The results obtained on 30 cm long fibres, as foreseen for the ALFA detectors, are well described by an exponential with an attenuation length L_{att} = 70 cm. Even though this value is well

below the anticipated 400 cm for round fibres it remains acceptable for short fibres with a light yield of about 4 photoelectrons. The surface quality of the fibre end opposite to the photodetector is of primary importance. As 50% of the scintillation light is emitted in the direction away from the photodetector, the light reflected from the opposite fibre end can contribute significantly to the total light yield. The fibre ends are machined with a single point diamond tool on a low-vibration numerical control machine. A reflective aluminium coating is applied by vacuum evaporation to the fibre ends which were cut under an angle of 90°. For fibres of 30 cm length this increases the light yield by 58% compared to uncoated fibres. The reflectivity at the aluminium/polystyrene interface was found to be approximately 0.75. For fibres with a 45° end cut an uncoated surface was found to lead to the highest light yield. Based on these satisfactory results obtained with these types of fibres it was decided to further investigate them for the construction of the ALFA detectors.

4.2.2 Photoelectric yield

To determine the light yield of the scintillating fibres, they are tested with the same photodetector that will be used in the ALFA system, namely the 64 channels MAPMT R7600-00-M64 by Hamamatsu. The expected photoelectric yield of this assembly is estimated from Eq. 2.3

$$\bar{N}_{pe} = N_{scint} \cdot \varepsilon_{coll} \cdot \varepsilon_{refl} \cdot \varepsilon_{att} \cdot \varepsilon_{in} \cdot \varepsilon_{Q_{eff}} \tag{4.1}$$

Assuming an energy loss in polystyrene (the core material of the fibre) of 0.2 MeV/mm and a scintillation yield of 8300 photons/MeV in the fibres, the number of generated scintillation photons per mm is $N_{scint} = 1660\ \text{mm}^{-1}$. The geometrical acceptance factor of a rectangular fibre is $\varepsilon_{coll} = 0.042$. The transport efficiency due to optical absorption on 30 cm long fibres with an attenuation length of 70 cm is $\varepsilon_{att} = e^{-30/70} = 0.65$ and the gain due to reflection from the opposite fibre end is $\varepsilon_{refl} = 1.58$ (for end cuts of 90°) or 1.42 (for end cuts of 45°). The transmission efficiency at the fibre/air/glass interface without any grease is $\varepsilon_{in} = 0.9$ and $\varepsilon_{Q_{eff}} = 0.14$ being the effective quantum efficiency of the MAPMT. The latter is the product of the quantum efficiency at 450 nm (≈ 0.2) and the photoelectron collection efficiency of the order of 0.7 for the MAPMT[109]. The photoelectric yield $\bar{N}_{pe}$ of fibres and the corresponding single fibre detection efficiency ε_{det} are calculated with Eqs. 4.1 and 2.7 respectively. The results are summarized in Table 4.1 for different configurations. One sees that all the fibres are expected to give yield sufficient light leading to detection efficiencies of the order of 98% to 100%

except the fibre SCSF-3HF from Kuraray. The lower light yield of approximately 2 photoelectrons of this fibre is due to the fact that its wavelength of maximum emission, of the order of 530 nm, is shifted with respect to the maximum sensitivity of MAPMT situated around 430 nm. For this reason no prototype detectors were built with this type of fibre. Nevertheless to verify its increased radiation resistance[117;118] with respect to the other fibres they were all studied during a dedicated irradiation campaign at CERN (see Section 4.2.3).

4.2.2.1 Experimental set-up

To study the performance of the fibres SCSF-78 and BCF-12 four prototype detectors consisting of a single plane with 2 layers of fibres orthogonal to each other were built (see Table 4.4). Details of the fabrication of the detectors can be found in Section 4.3 Detectors 1_2_6 and 1_2_32 were built with the fibre SCSF-78-SJ, 1_2_6_1mm with the fibre SCSF-78-SJ-1 and 1_2_32_B with Bicron single and double cladded fibres BCF-12SC and BCF-12MC. All the fibres are read-out with the ALFA baseline MAPMT, operating at 950 V with a gain of the order of 5×10^6, and exposed to 6 GeV electrons from a beam line at DESY in 2005. Their performance was estimated according to the type of cladding (single or multiple), the cut angle of the fibre end (45° and 90°), the presence or absence of a reflective surface at the fibre end and finally the distance between the fibre and the MAPMT window.

The detectors under test are mounted on a motorized XY table which allowed to centre them with respect to the beam delivered by the DESY T22 facility[119]. This facility provides a low intensity electron (or positron) beam ($f \leqslant 1$ kHz) of up to 7 GeV energy. The beam is collimated to a spot of about 1 cm^2 and has a low divergence $\sigma_x \approx \sigma_y \approx 1$ mrad. A beam telescope consisting of three silicon microstrip detectors (one upstream and two downstream with respect to the detector under test) is used to determine the trajectory of the incident electrons with a spatial resolution in x and y of the order of 20-30 μm, depending of the amount of material in the beam[120;121]. The active area of the telescope was 32×32 mm^2. The beam trigger is defined by the coincidence of three 3 mm thick scintillators of 9×9 mm^2.

The MAPMTs of the ALFA prototype detectors were read-out in two different ways. High gain operation at a bias voltage of the order of 950 V with a gain of the order of 5×10^6 allowed to feed the signals directly into VME charge sensitive ADC modules (CAEN V792) via a twisted pair cable. Alternatively the signals were amplified, shaped and discriminated by the OPERA front-end read-out chip[122] operating the MAPMTs

at half the previous gain value. The OPERA chip is the predecessor of the MAROC[105] circuit used later for the final architecture of the ALFA system. A classical trigger and busy logic was implemented with standard NIM modules. The data taking rate was limited by the analog read-out electronics of the beam telescope to about 70 Hz.

To calibrate the charge amplitude of the MAPMTs, all channels were exposed to very low light levels from a pulsed LED emitting in the blue range. The charge spectra recorded with the ADC modules (CAEN V550) for different bias voltages (900, 950 and 1000 V) were fitted with a Poisson distribution convoluted with Gaussian functions as described by Eq. 2.3. Figure 4.1 shows a typical single photoelectron spectrum and the corresponding fit. The single photoelectron and the pedestal peak are well separated. One can also see the shoulder on the right corresponding to the second photoelectron contribution.

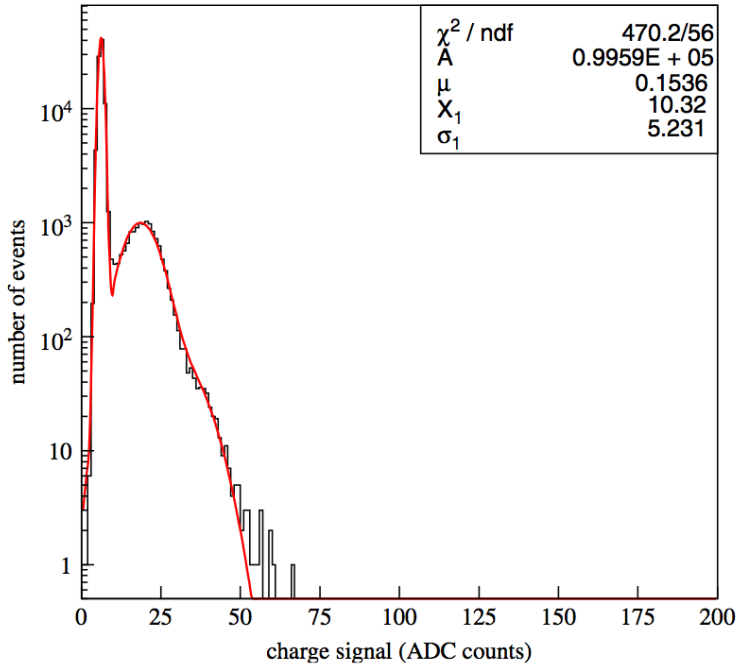

Figure 4.1: Single photoelectron spectrum obtained at 950 V. The shoulder around 33 ADC counts is due to the second photoelectron.

4.2.2.2 Results

The charge spectra obtained with fibres in the electron beam are fitted with the method described in Section 2.4.1 while keeping the pedestal and single photoelectron parameters on the values determined by the calibration. Even though the fit with Eq. 2.5 leads to satisfactory results it fails to describe a small non-Poissonian bump in the

charge distribution corresponding to an excess of primarily single and very few double photoelectrons which is consistently present in the spectra. This excess is attributed to cross-talk from adjacent MAPMT channels, described in detail in Section 4.3.5, and can be incorporated in the fit function by simply adding a second Poisson distribution with a small $\bar{N}_{pe_{CT}}$ parameter

$$F'(x) = F\left(x, \bar{N}_{pe}\right) + F_{CT}\left(x, \bar{N}_{pe_{CT}}\right) \tag{4.2}$$

This fit function describes the data well as can be seen by the fitted charge spectrum shown Fig. 4.2. The results are summarized in Table 4.2. The number of detected photoelectrons for the Kuraray SCSF-78-SJ fibre is of the order of 3.9 for 45° cut fibres and 4.4 for 90° cut fibres. The agreement with the expected photoelectric yield values reported in Table 4.1 is better than 3%. The relative cross-talk contribution defined as $\bar{N}_{pe_{CT}}/(\bar{N}_{pe}+\bar{N}_{pe_{CT}})$ is of the order of 3.4%. The Bicron fibres exhibit lower light levels than the Kuraray SCSF-78-SJ fibre while the SCSF-78-SJ-1 fibres have the highest yield as expected because of their bigger cross-section with respect to the other fibres. Adding an external mirror at the edge of the 45°-cut fibres naturally increases the light yield but also the cross-talk. Leaving a 0.5 mm gap between the fibre and the MAPMt window has a slightly beneficial effect but increases the cross-talk even more than the mirror. A gap of 1 mm has no advantage on the yield and almost triples the cross-talk. Based on these results, the fibre Kuraray SCSF-78-SJ is singled out as the baseline fibre for the ALFA detectors in a configuration without any external mirror nor any air gap between the fibre end and the window of the MAPMT.

Table 4.2: Results of the fits of signal spectra with a bias voltage of 950 V; photoelectric yield and cross-talk. The errors are RMS values

Fibre type	Configuration	$\bar{N}_{pe}$	Cross-talk contribution (%)
Kuraray SCSF-78-SJ	45°	3.93 ± 0.18	3.4 ± 1.3
Kuraray SCSF-78-SJ	90°	4.45 ± 0.50	3.4 ± 0.8
Kuraray SCSF-78-SJ	45°, mirror	4.87 ± 0.49	4.2 ± 1.8
Kuraray SCSF-78-SJ	45°, 0.5 mm gap	4.09 ± 0.25	6.9 ± 2.3
Kuraray SCSF-78-SJ	45°, 1.0 mm gap	3.88 ± 0.25	8.6 ± 2.4
Bicron 612 BCF-12SC	45°	3.02 ± 0.36	3.4 ± 2.1
Bicron 612 BCF-12MC	45°	3.20 ± 0.32	3.6 ± 1.8
Kuraray SCSF-78-SJ-1	45°	7.39 ± 0.44	4.3 ± 2.6

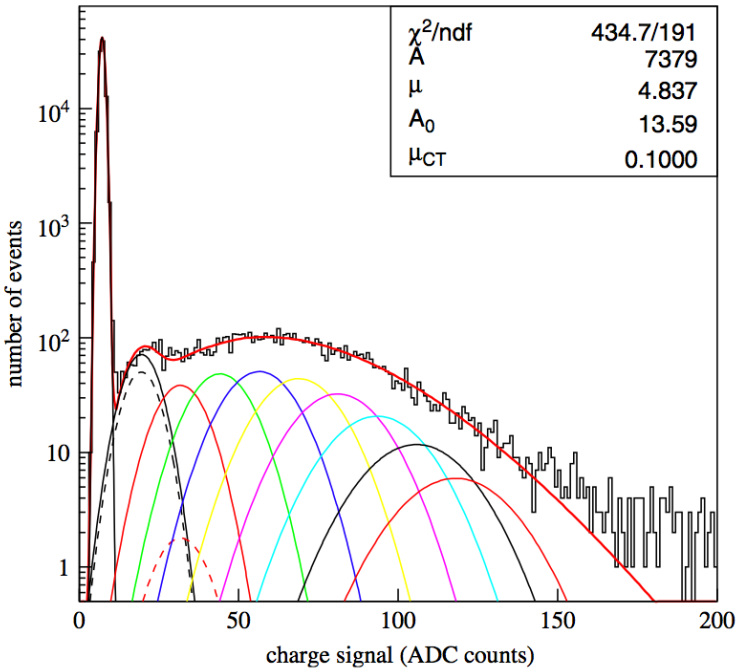

Figure 4.2: Photoelectron spectrum from a 0.5 mm fibre (45° cut) obtained at 950 V. The average number of photoelectrons is 4.8 and the cross-talk term contribute up to 0.1 photoelectrons. The Gauss curves represent the i^{th} photoelectron, with i = 1, 2,..., 9, and the dashed Gauss curves show the cross-talk contribution.

4.2.3 Radiation resistance studies

During normal operation, the fibres of the ALFA detectors will be exposed to radiation doses of the order of 100 Gy/yr (see Section 3.4.2). The Kuraray SCSF fibre series was developed for improved radiation resistance. It had previously been investigated in terms of radiation hardness for the development of a hodoscope for the COMPASS experiment[123] and for the possible use in the inner tracker of HERA-B[124]. These studies showed that these plastic scintillating fibres should not deteriorate significantly at the accumulated doses during ALFA operation. However since the magnitude of the damage effects in plastic fibres depends strongly on various parameters such as the nature of the radiation[38], the dose rate[125], the environment[30], the presence or absence of oxygen during[126] and after[33] irradiation, and the wavelength of emission[31] (see Section 2.3.3), the radiation resistance of the ALFA baseline fibre (Kuraray SCSF-78-SJ), together with other types of fibres (Kuraray SCSF-78-3HF and Bicron 612 BCF-12SC), was studied under realistic ALFA conditions[127]. The effects of radiation damage on scintillation light yield, wavelength shifter efficiency and optical transparency were determined for accumulated doses ranging from a few Gy up to 2 MGy[103].

4.2.3.1 Experimental set-up

The fibres were exposed to 24 GeV/c protons with fluences ranging from $6.78{\cdot}10^{11}$ to $8.40{\cdot}10^{15}$ p·cm^{-2} in the IRRAD1 facility[128] in the T7 beam line of the CERN PS accelerator. The irradiation campaign lasted one month and the fibres were irradiated to doses ranging from about 100 Gy to more than 2 MGy. The fibres irradiated are the Kuraray SCSF-78-SJ with and without aluminum coating, the Kuraray SCSF-3HF and the Bicron 612 BCF-12SC without coating.

Two sets of fibres, each containing samples of all the different types of fibres, were irradiated simultaneously. The first bunch was parallel to the beam axis and the fibres were fully irradiated. These fibres were intended for scintillation light yield studies (see Section 4.2.3.2.2). The second set of fibres was placed perpendicular to the beam and in this case they were irradiated only on a small section of approximately 10 mm determined by the beam profile. These fibres were then used to characterize the wavelength shifter and transparency degradation (see Section 4.2.3.2.1). A PMMA tool was fabricated to support carbon tubes in which the fibres were inserted. Fifteen tubes were parallel to the beam and fifteen other were perpendicular to it. The tool was placed on an XYZ translation table which was moved to irradiate the various sets at different doses without the need to enter the beam area. The dose accumulated in the fibres, due to beam protons as well as protons backscattered from the beam dump, was determined by spectrometric analysis of aluminum foils wrapped around the fibres during irradiation. The foils were positioned upstream and downstream at the two ends of the horizontal carbon tubes containing the fully-irradiated fibres.

4.2.3.2 Results

At doses of the order of tens of kGy the fibres turn yellow. Figure 4.3 shows pictures of cracks and blisters at the surface of the cladding caused by polymer chains breaking by scission[31] and swelling[129] under irradiation. Similar degradations have been observed on bare PMMA samples[130] which progressively turn brown with the accumulated dose, fading to yellowish-brown after irradiation. The cracks start forming one week after the irradiation for absorbed doses above 10 kGy and continue diffusing up to two months after the irradiation. The density of the final network crack increases with the deposited energy density. The coloration and the crack network could not be monitored during our campaign because there was no access to the irradiation zone but the post-irradiation observations confirm that the damage evolution of the fibres' PMMA cladding is comparable to the damage of bulk PMMA samples.

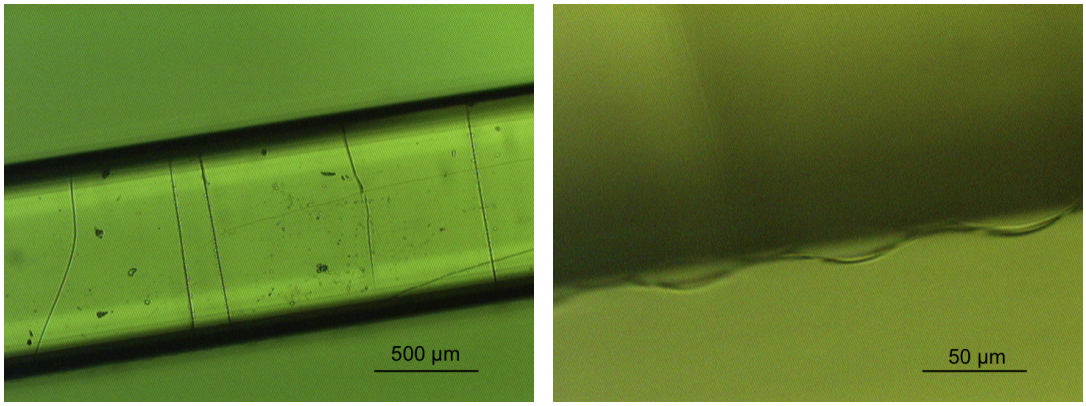

(a) **(b)**

Figure 4.3: (a) Cracks and (b) blisters observed on the cladding of the irradiated plastic scintillating fibres. In these pictures the damage to the cladding of a Kuraray SCSF-3HF fibre irradiated to an accumulated dose of 166 kGy is shown.

4.2.3.2.1 WLS and transparency degradation The degradation of the wavelength shifter efficiency and of the optical transparency is determined with a single set of measurements on the spot-irradiated fibres. The light output of these fibres is recorded with a spectrometer (Ocean Optics SD2000) while being excited by a LED, emitting around 355 nm (UVTOP 355 nm by Sensor Electronic Technology), at different positions along the fibres' axis. The measurements are normalized to the value measured closest to the spectrometer. As the LED approaches the irradiated spot, centered 7 cm away from the fibre edge, the light amplitude decreases as a consequence of both the wavelength shifter degradation and reduction of the optical transparency. At a distance of about 3 cm from the irradiated spot centre, the light amplitude increases but never recovers the initial value. The light produced in this non-irradiated part of the fibre is unaltered but it goes through the irradiated section where it is strongly attenuated. One can thus estimate the optical transparency degradation of the irradiated section of the fibre and disentangle the loss of wavelength shifter efficiency. The fibre 3HF exhibits a better resistance to radiation with respect to the fibre SCSF both in terms of wavelength shifter and transparency up to 166 kGy (see Fig. 4.4). The transparency degradation is proportional to the accumulated dose but the effect is less important for increasing wavelength[42]. For this reason the green-emitting 3HF fibres have a better radiation resistance than the other fibres emitting in the blue region as expected and reported before[117;118]. Above doses of the order of the MGy all the different types of fibres exhibit the same level of degradation.

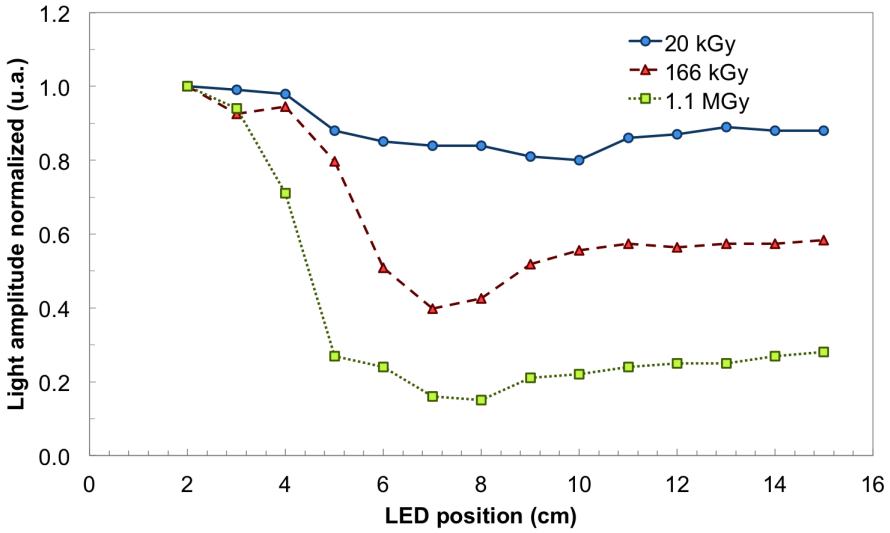

(a)

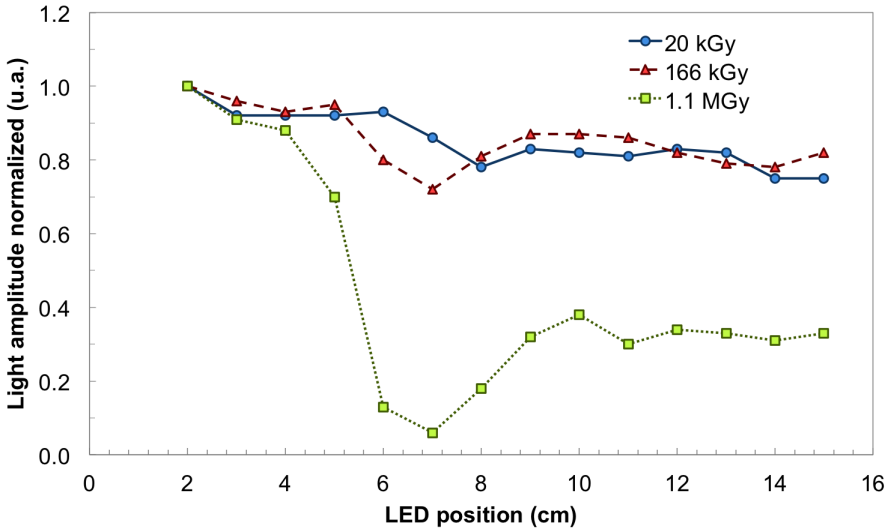

(b)

Figure 4.4: Light yield of (a) SCSF-78-SJ and (b) SCSF-3HF fibres irradiated on a 10 mm spot at accumulated doses of 20 kGy, 166 kGy and 1.1 MGy as a function of the LED position.

4.2.3.2.2 Scintillation light yield degradation The scintillation light yield of irradiated fibres is measured by exciting them with a ^{90}Sr source. The fibres under test are read-out by a GM-APD (Hamamatsu MPPC Multi Pixel Photon Counter S10362-11-100U). Triggering is performed by an Al-coated reference fibre placed underneath the irradiated fibre and coupled to a PMT (Hamamatsu R647-01). The charge spectra of the fibres are recorded with an oscilloscope (LeCroy WavePro 7100A) and analyzed with the software package PAW[131] by following the method described in Section 2.4.1.

The average number of photoelectrons is determined by fitting the charge spectra with Eq. 2.5 and the detection efficiency is calculated with Eq. 2.7. Both values are plotted in Fig. 4.5 as a function of the accumulated dose for all the fibres investigated. It should be noted that the emission spectrum of the Kuraray SCSF-3HF fibre peaks around 530 nm where the read-out diode has an efficiency of about 37.5% whereas the Kuraray SCSF-78-SJ and the Bicron 612 BCF-12 peak around 450 nm where the efficiency of the diode is of the order of 59%. This explains the low photoelectric yield obtained with non-irradiated 3HF fibres with respect to the other fibres. Nevertheless one sees in Fig. 4.5b that it shows a better behavior under irradiation. The yield is constant up to accumulated doses of the order of 20 kGy whereas for the other fibres it starts decreasing for doses as low as a few hundred Gy. The detection efficiency is by consequence lower for the 3HF fibres in this configuration up to accumulated doses of the order of 100 kGy where it is better than for the other fibres confirming its increased radiation resistance.

4.2.3.2.3 Detection efficiency degradation Table 4.3 summarizes the detection efficiency of the fibres investigated for low luminosity runs where the accumulated dose should be of the order of 100 Gy and for high luminosity runs with a foreseen accumulated dose in the fibres up to about 1 MGy. With a detection efficiency close to 100%, the Kuraray SCSF-78-SJ is fully suitable for ALFA operation in dedicated low luminosity runs. When reaching greater doses during high luminosity runs it could still potentially be used. However the fibre 3HF is slightly more efficient at such doses in spite of the non-optimal read-out with respect to its emission spectrum. For operation of the ALFA detector under these conditions, an alternative design with 3HF fibres read-out by photodetectors sensitive in the green could be envisaged for an increased detection efficiency. In both high and low luminosity scenarios the aluminum coating does not affect the performance of the fibres.

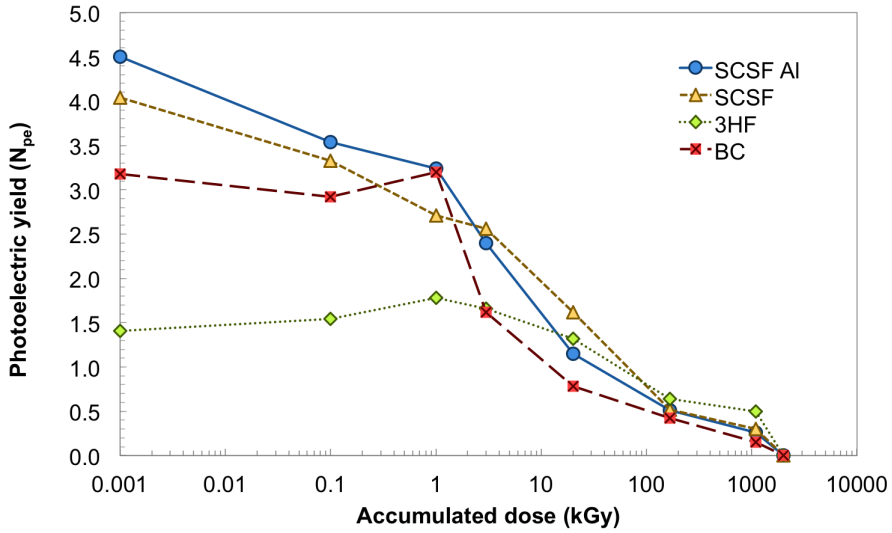

(a)

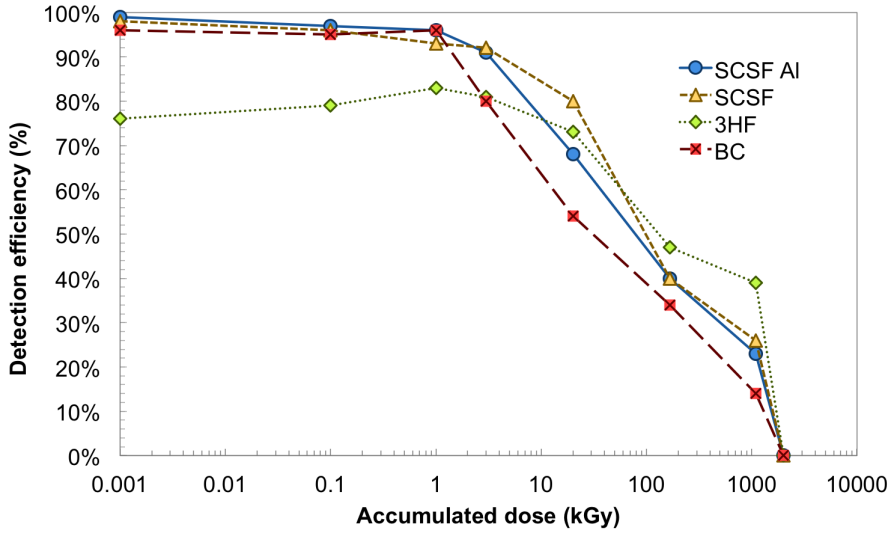

(b)

Figure 4.5: (a) Photoelectric yield (b) detection efficiency of the plastic scintillating fibres as a function of the accumulated dose.

Table 4.3: Detection efficiency of plastic scintillating fibres as a function of the accumulated dose

Fibre type	Low luminosity (10^2 Gy)	High luminosity ($10^5 - 10^6$ Gy)
Kuraray SCSF-78-SJ	96%	40%
Kuraray SCSF-78-SJ Al-coated	97%	40%
Kuraray SCSF-3HF	79%	47%
Bicron 612 BCF-12	95%	34%

4.2.4 Bending fibres to small radiuses

The fibres of the overlap detectors have to be routed from the small extrusions at the bottom of the pots to connectors in front of the MAPMT windows at the top (see Section 3.5.3). The necessity to keep fibres horizontal over 8 mm on both sides (left and right) of the tracker and the limited space available inside the pot requires to bend the fibres at 90° to very small radiuses of the order of 20 mm. This leads to significant degradation of the light transport performance due to mechanical damage if bending is performed at room temperature[115]. Cracks are formed in the cladding and possibly extend into the core. Light transmission along a cracked fibre is dramatically reduced as the light can either be reflected out of the fibre or backwards at the level of the cracks. Moreover the fibre damage and the associated transport losses evolve with time.

The plastic scintillating fibres of interest for the ALFA detectors consist of a polystyrene (PS) core wrapped by a poly(methyl methacrylate) (PMMA) cladding. Both materials are amorphous thermoplastic polymers in solid state at room temperature which soften and become malleable when heated above their glass transition temperatures T_g. They return to a solid state when cooled at room temperature again. They can thus be re-shaped repeatedly by going through thermal cycles. Mean values for the glass transition temperatures T_g of PS and PMMA have been reported to be of the order of 95°C and 105°C respectively[132]. A wide range of transition temperatures can be found in literature, depending on many parameters such as the exact composition of the products, their molecular weight distribution and the additives contained. Hence a study of the thermal characteristics of the ALFA baseline fibres was carried out to define the temperature above which they could be bent without any damage and used for the fabrication of the overlap detectors[108]. The tests were performed between 30°C and 180°C. The first series of tests consisted in bending bares fibres in a Teflon tool at an angle of 90° at different temperatures and measuring the residual angles once cooled. Figure 4.6 shows the results for bare scintillating fibres and aluminum coated fibres. In the case of non coated fibres one sees that the residual angle increases with the temperature. Angles of 90° are reached for temperatures between 90°C and 105°C. Above these temperatures the fibres deform beyond the required angle. These tests were repeated for aluminum coated fibres up to 105°C showing that they bend at smaller angles up to 80°C where an abrupt transition takes place and residual angles similar to those of bare fibres are obtained.

The second series of tests was dedicated to studying optical properties of bent fibres. Their light yield was measured before and after bending to investigate degradation

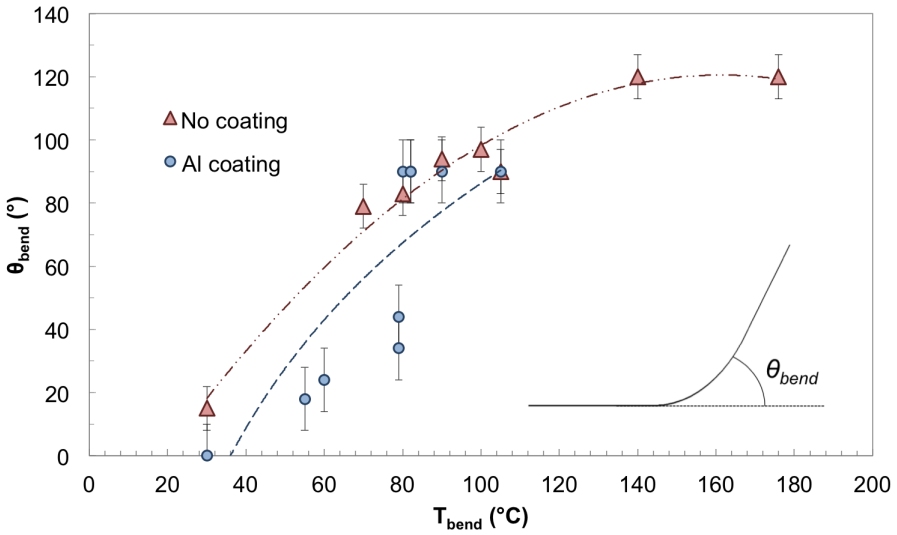

Figure 4.6: Residual angle of the bare fibres and aluminum coated fibres bent at temperatures ranging from 30°C to 180°C.

effects due to temperature and bending. The fibres were excited at one end with an LED (Bivar LED5-UV-400-30 series) and the fluorescence light was measured at the other end by a silicon photodiode (Newport 818-UV). The photocurrent was measured on straight fibres and it was measured again 10 minutes after bending and 20 days later. The normalized ratios of the photocurrents I_0 / I_t, measured before and after bending, are plotted in Fig. 4.7. It shows that fibres which are bent at temperatures between 70 and 120°C maintain satisfactory optical properties.

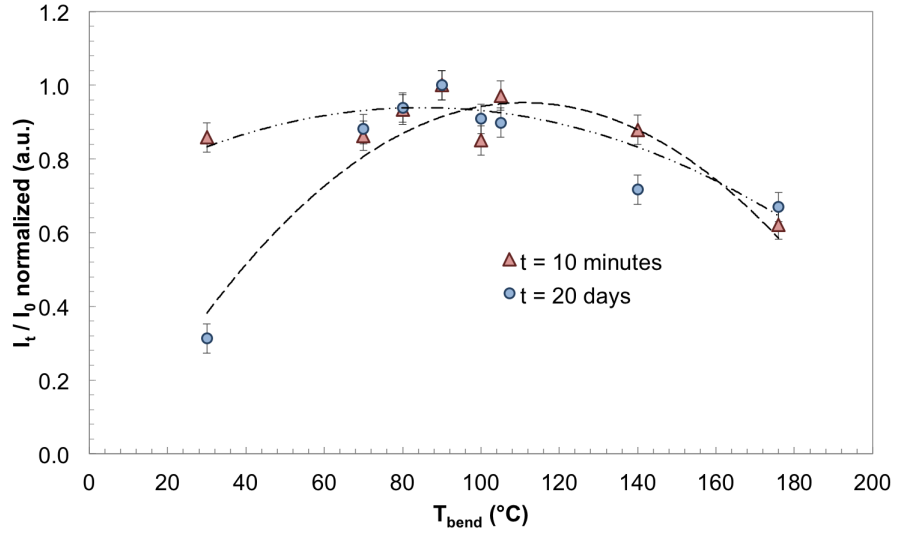

Figure 4.7: Normalized ratio of photocurrents measured before and after bending of the fibres.

A bending procedure with a dedicated Teflon tool has been defined to bend 30 aluminized scintillating fibres at once following a thermal cycle. The fibres are positioned in the tool at room temperature and kept straight until a temperature of 85°C is reached. At this point they are gently bent taking great care of leaving an 8 mm straight section at one end of the fibres. This straight section guarantees the 6 × 15 mm^2 region where the 30 horizontal fibres are vertically stacked to define the active area of the overlap detectors. The fibres are left at this temperature for about 20 minutes and slowly cooled down at room temperature. These fibres were characterized under the same conditions as straight fibres and identical photoelectric yields were measured validating the thermal cycle and the bending procedure.

The prototype overlap detectors characterized during the 2006 test beam campaign[110] at CERN were fabricated with fibres bent following the procedure presented here(see Section 4.4.1). The results obtained with these detectors during the beam test experiments were fully satisfactory (see Section 4.4.2) and no ageing effects were observed on their fibres when re-characterized 4 years later[133].

4.2.5 ALFA baseline fibre

In view of the results obtained with the plastic scintillating fibre Kuraray SCSF-78-SJ in combination with the 64 channels MAPMT R7600-00-M64 by Hamamatsu they have been selected as the baseline scintillator-photodetector assembly for the ALFA detectors. The high photoelectric yield of the order of 4 photoelectrons of this assembly and the radiation hardness of the fibres guarantee a detection efficiency close to 100% during dedicated low luminosity LHC runs. The SCSF-78-SJ fibre is a single-cladded 0.5 mm square fibre with a Polystyrene core and a 10 μm thick PMMA cladding. The fibre's emission spectrum expands from about 415 nm to above 550 nm with a maximum around 440 nm where the MAPMT sensitivity is the highest. The design of the ALFA detectors requires only relatively short pieces of fibres of about 30 cm and small bending radiuses of the order of 20 to 30 mm. The S-type fibres whose core consists of axially-oriented polymer chains represent the best compromise between light attenuation and minimum bending radiuses. The molecular orientation of the core along the drawing direction strengthens the fibres at the cost of transparency. The attenuation of this type of fibre is nearly 10% shorter than the standard type. However this is not an issue in the ALFA detectors' configuration. The fibres are relatively short and the light attenuation is not critical for such small distances with a photoelectric yield of the order of 4 photoelectrons with the MAPMT R7600-00-M64. Moreover the mechanical

strength is required to route the fibres inside the roman pots with small radiuses. In addition, the design of the overlap detectors requires even smaller bending angles which can be reached with these fibres by following a specially developed procedure. In order to minimize the optical cross-talk between the closely packed fibres of the ALFA detectors, their surface is coated with an evaporated aluminum film of about 100 nm thickness which also acts a high quality reflector with a reflectivity of the order of 0.8.

4.3 Tracking detectors

Before assembling a full scale prototype, eight detectors were fabricated with different configurations to validate the concept and design of the ALFA tracking system. Four detectors with single planes were dedicated to characterizing the different types of fibres. The Kuraray fibres were studied with detectors 1_2_6, 1_2_6_1mm and 1_2_32 while the Bicron fibres were investigated with detector 1_2_32_B . Two detectors consisting of 10 staggered planes with 2 × 6 fibres (10_2_6) and 2 × 16 fibres (10_2_16) were intended for spatial resolution studies. Larger detectors with 2 planes of 2 × 32 fibres (2_2_32) and 2 × 64 fibres (2_2_64) were useful to study cross-talk between fibres and between adjacent MAPMT channels. The detector 2_2_64, representing the final geometry with 64 fibres per layer, allowed to address the production and metrology procedures. Eventually a full-scale prototype detector (10_2_64) was built to study integration in the pots and operation with full-scale dedicated electronics architecture. The characteristics of the prototype detectors and the studies for which they have been used are compiled in Table 4.4.

Table 4.4: Prototype scintillating fibre tracking detectors built for beam test experiments.

Detector	Planes	Fibres	Fibre type	Studies
1_2_6	1	2 × 6	SCSF-78-SJ	Light yield
1_2_32	1	2 × 32	SCSF-78-SJ	Light yield
1_2_6_1mm	1	2 × 6	SCSF-78-SJ-1	Light yield
1_2_32_B	1	2 × 32	BCF-12SC(MC)	Light yield
10_2_6	10	2 × 6	SCSF-78-SJ	Resolution
10_2_16	10	2 × 16	SCSF-78-SJ	Resolution
2_2_32	2	2 × 32	SCSF-78-SJ	Cross-talk
2_2_64	2	2 × 64	SCSF-78-SJ	Cross-talk
10_2_64	10	2 × 64	SCSF-78-SJ	Full-scale proto.

4.3.1 Construction and metrology

The fabrication of the prototype tracking detectors took place in a class 10000 clean room at CERN. Whenever it was possible, the components were standardized. For example, the detector 10_2_6 consisted of 10 identical UV planes and the staggering was only introduced when the steel blade was glued on the plate (step 10 of the fabrication process). Simple but precise three-point alignment tools have been specifically designed and fabricated to a precision better than 10 μm. Optical surveys with an accuracy of about 3 μm were performed at three different stages during the fabrication process (see Appendix C). The sequence of steps is the following:

1. LASER cutting of the central and stiffener plates from Al_2O_3 ceramic sheets at a precision of about ± 30 μm.
2. Survey of the plates' geometry and selection of the best matching sets.
3. Glueing of left stiffener plates on front and rear side of support plates. Alignment via lateral and bottom edges.
4. Survey for control and determination of reference points.
5. Machining and aluminum coating of the fibre ends.
6. Aluminum coating of the fibre sides.
7. Positioning and glueing of the Al coated on the two sides of the plates. The fibres are aligned with the 45° edge of the left stiffener plate and gently compressed by the right plate. The end of the fibres with a 90° cut are precisely positionned while the fibres with the 45° cut are left a few mm longer than needed.
8. Machining with a single point diamond tool of fibre ends (only 45° cut fibres) to final length and surface quality.
9. Survey for control of the fibres position, pitch and angle.
10. Glueing of the support blade made of hardened steel. The position of the blade is chosen to produce the desired staggering. This step is done by means of an alignment plate which provides a specific position for each displacement and allows to partly correct for small geometrical errors accumulated in the sequence up to this point.
11. Survey of the fibres positions and angles relative to the precision holes of the steel blade.
12. Assembly of the planes on a support arm through two precision pins.

13. Threading of the fibres into the connector and subsequent glueing. A system has been adopted which avoids that adjacent fibres on the detector are not connected to adjacent channels on the MAPMT.
14. Machining with a diamond tool of the protruding fibre ends on the connectors.

Optical cement (Bicron BC-600) was used to glue both the fibres and the ceramic plates. The geometrical data measured during the final survey of each detector was recorded in geometry files and later used during the data analysis and in particular for the space point reconstruction (see Section 4.3.2). All prototypes were tested in a laboratory experimental set-up where the fibres were exposed to an ^{90}Sr source and read-out by an MAPMT. The results of these tests gave promising indications of light yield and uniformity of the detectors before the test beams.

4.3.2 Spatial resolution

The main purpose of the ALFA detector is the determination of the t-spectrum of elastically scattered protons through the measurement of the coordinates of their impact points in the transversal plane with a required precision of the order of 30 μm (see Section 3.4.2). Tracking studies were carried out on various prototype detectors (10_2_6, 10_2_16 and 2_2_32) to demonstrate the achievable spatial resolution. The space points were determined from the crossing area of fibres hit in the U and V planes and the spatial resolution was achieved by combining hits from the consecutive staggered planes.

The reconstruction of the impact point is performed in several consecutive steps. First, the hits are selected above a certain energy cut which is set to 0.9 photoelectrons. Ideally a particle traversing the ALFA detector perpendicularly hits 20 fibres (10 U and 10 V fibres). The hit multiplicity of 10_2_6 with 6 GeV electrons is on average higher than 20 (see Fig. 4.8a). This can be explained by multiple hits per layer due to δ-electrons as described in Section 4.3.5. Multiplicities lower than 20 are also recorded. In this case they are due to inefficiencies leading to layers without any hit as shown in the hit distribution per layer of Fig. 4.8b. On average 18 layers have at least one hit and only 14% of the recorded events have all 20 layers hit (see Fig. 4.8c).

A single layer has on average about 80% of single hits, 10% of zero hits and 10% of multiple hits. The presence of multiple hits in a layer complicates the reconstruction of tracks as the hits generated by the primary particle have to be selected and the secondary interactions and cross-talk signals have to be discarded. A track seed is

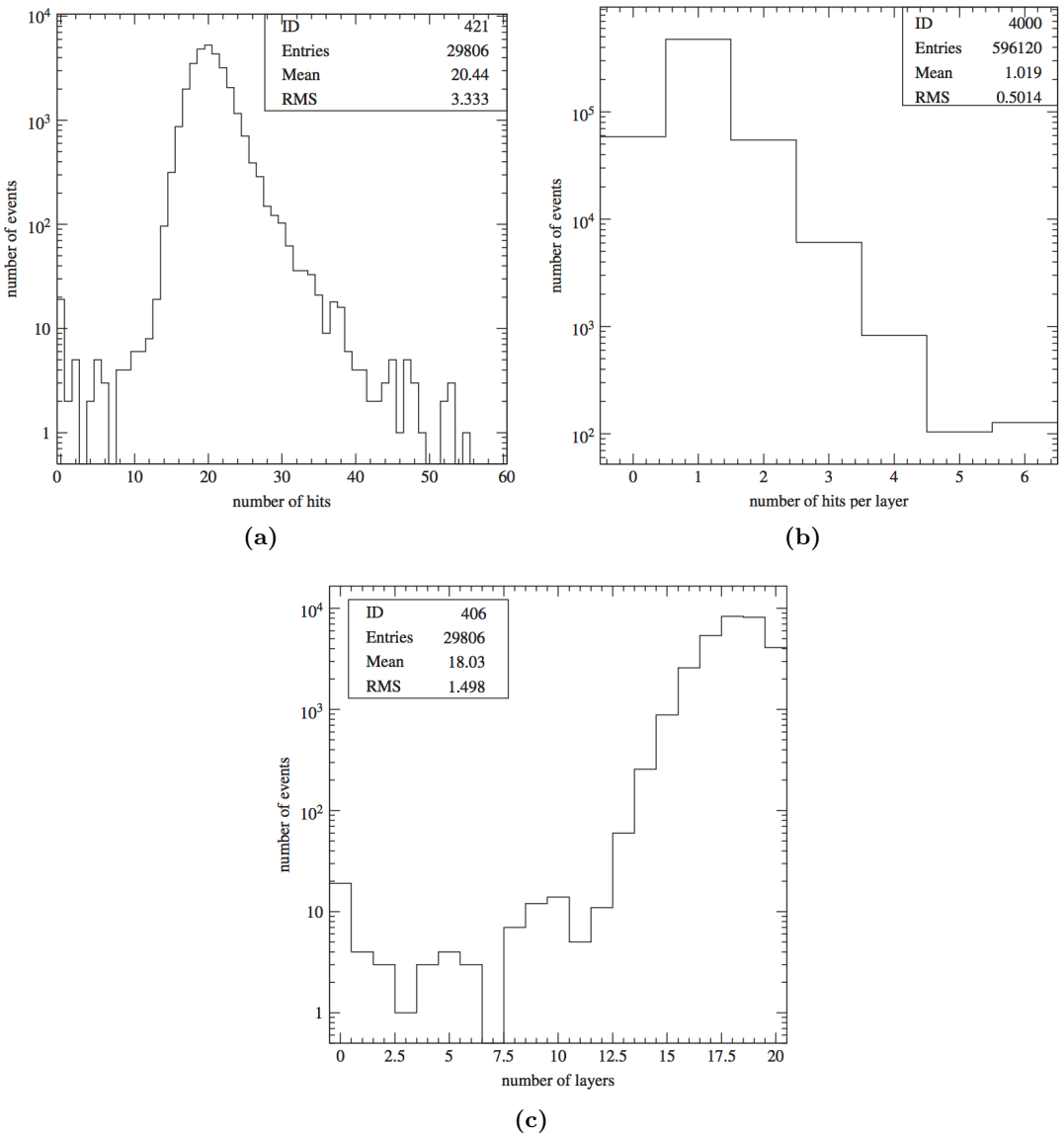

Figure 4.8: Hit multiplicity distribution (a) averaged over all layers, (b) for single layers and (c) layer multiplicity distribution in detector 10_2_6 for 6 GeV electrons.

determined with the minimum overlap algorithm by selecting only planes with single hits. The principle of this algorithm is to determine the point where the particle traversed the detector based on the overlapping area of fibres of interest for the U and V layers separately. The starting point of the procedure is a seed which is taken as the centre of gravity of the hits so that hit fibres away from the seed with no overlap are rejected. The centre of the overlap area, represented by a linear equation, is then used to calculate the crossing points of U and V fibres to define the x and y coordinates of the space point seed. The quality of the seed is quantified by a metrics Δ which measures the distance of closest approach of the centre of the fibres to the space point candidates, averaged over all participating fibres. The minimal overlap algorithm is then executed in a loop over the layers with more than one hit, iterating over all the hits in that layer. The hit fibre with the best Δ is retained. At the end of the iteration the final space point seed is thus based on the hit configuration with the highest quality track.

The space point resolution of the detector 10_2_6 is then determined by comparing the reconstructed x and y coordinates with the tracks measured by the telescope in the centre of the detector within a circle of 1 mm radius and with a polar angle below 1 mrad. In order to determine the total resolution the distribution of the residuals x_{ALFA} - $x_{telescope}$ is fitted by a Gaussian. The intrinsic resolution of the telescope is determined similarly by using the residuals from the central station. The spatial resolution of the detector is calculated from the quadratic subtraction of the telescope contribution to the total resolution. The resolution results obtained with the prototype detector 10_2_6 are of the order of 36 μm for x and y.

There is only a moderate dependance of the resolution to the number of hit planes in 10_2_6. For a fixed cut of 0.9 photoelectrons the resolution improves from about 37 μm for at least 12 hit planes to about 33.5 μm when all 20 planes are requested to be hit. On the other hand the tracking efficiency dramatically decreases from 99% for 12 planes to 10% for 20 planes.

A scan of the electron beam energy from 1 to 6.5 GeV showed that the resolution degrades with decreasing energy. For 1 GeV electrons the resolution is of the order of 100 μm. This degradation is due to the multiple scattering and shower processes generated by the relatively low electron energy[134] and the amount of material in the beam line corresponding to approximately 10% of X_0. However this is irrelevant for operation with protons at LHC energies in the TeV range.

The detector 2_2_32 was also used for spatial resolution studies with 6 GeV electrons[135]. In this case the MAPMTs were read-out with the OPERA electronics[122]. Custom designed read-out cards housing two OPERA chips, with 32 channels each, were plugged directly on the output pins of the MAPMTs. The discriminated signals as well as the charge amplitude of all the channels were accessible with this read-out and both are used to reconstruct the x and y coordinates of the position of the tracks and good correlation is found between the two. A spatial resolution of about 73.8 μm was measured. This is in good agreement with with the expected resolution of 72 μm ($= 500$ μm / 2 / $\sqrt{12}$).

Further spatial resolution studies were performed with the detector 10_2_16 in high momentum hadron beams (230 GeV p and π^+) such that multiple scattering becomes marginal. In this case, two methods are used to assess the spatial resolution of 10_2_16. Firstly, in the absence of a high resolution beam telescope the detector was sub-divided in 2 halves each consisting of 5 U and 5 V planes. The resolution is estimated from a comparison of the track segments in the 2 detector halves and the output of a Monte-Carlo simulation with the measured detector geometry. Based on this stand-alone method a full detector resolution of about 23 ± 2 μm is extracted. In a second stage a silicon telescope was used to predict the track position at the location of the detector. The residual distributions from the tracks of the full detector and tracks of the telescope lead to a spatial resolution of the order of 25 ± 3 μm.

Table 4.5 summarizes the results of the spatial resolution studies obtained with the different prototype detectors in various beam configurations.

Table 4.5: Spatial resolution obtained with different prototype detectors configurations.

		Spatial resolution (μm)	
Detector	Beam	Monte Carlo	Measured
10_2_6	6 GeV e^-	35[136]	33.5[109]
2_2_32	6 GeV e^-	72[109]	73.8[109]
10_2_16	230 GeV p/π^+	22[137]	25[110]

4.3.3 Detection efficiency

The efficiency of individual fibres is determined by selecting events with hits in their central area. Events with hits further than 200 μm from the centre of the fibres (*i.e.* 50 μm from the edge) are rejected. The efficiency is studied as a function of the cut applied

to the signal amplitude in photoelectrons. It is of the order of 98% for a zero photoelectron cut, as anticipated from the photoelectric yield calculated in Section 4.2.2, and it drops to about 92% for a 0.9 photoelectrons cut. This is the cut applied for the track reconstruction studies described in Section 4.3.2. Potential efficiency losses near the fibre edges, originating from insensitive cladding and glue remaining between the edges of the fibres, are investigated by scanning the fibres in slices of 50 μm (see Fig. 4.9). The efficiency is then evaluated both for individual fibres and for entire planes. The plane efficiency is rather uniform. It ranges from approximately 95% in the core of the fibres to about 80% in the inter-fibre region. The total efficiency, defined as the probability to have at least one hit per plane, thus amounts to 99.9%.

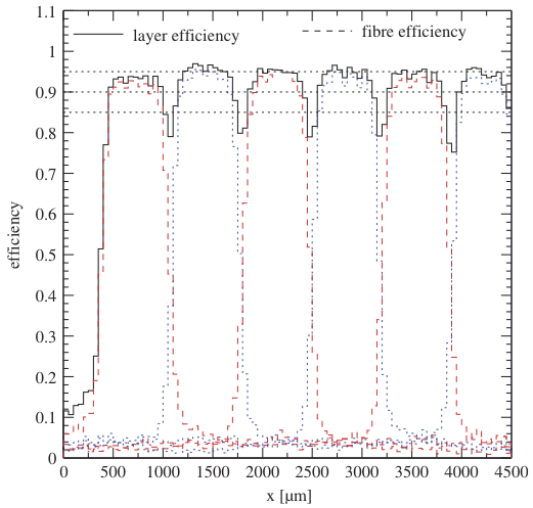

Figure 4.9: Layer efficiency (solid line) and fibre efficiency (dashed line) for a fixed cut of 0.9 photoelectrons as function of the horizontal beam position.

4.3.4 Edge sensitivity

The edge sensitivity was studied for the detectors 10_2_6 and 2_2_32 with their lower edge well inside the telescope trigger region. Dedicated runs were taken with a plastic scintillator counter, called S330, mounted below the detectors in contact with the edge defined by the 45°-cut fibres. The vertical coordinate of the particle tracks passing either through the fibre detector or through the scintillator is reconstructed using the telescope data. The histograms obtained are fitted by smeared-edge functions consisting of a Heavyside step function convoluted with a Gaussian. The fits provide an estimate of the edge location and of its Gaussian smearing. The histogram of Fig. 4.10a shows the y-coordinate from the tracks giving a hit in layer 3 or 4 of 2_2_32 and S330. The

fit determines the edge locations of the layers 3 and 4 at $y_3 = 15386 \pm 4$ μm and $y_4 = 15393 \pm 4$ μm and the edge location of S330 at y_{S330} 15371 $\pm$ 6 μm.

The reliability of this method is illustrated in Fig. 4.10b where the fitted edge locations of the 20 fibre layers of the 10_2_6 detector are plotted together with the optically measured positions of the edges. The agreement of the two data sets is very good with an rms deviation of the order of 6 μm.

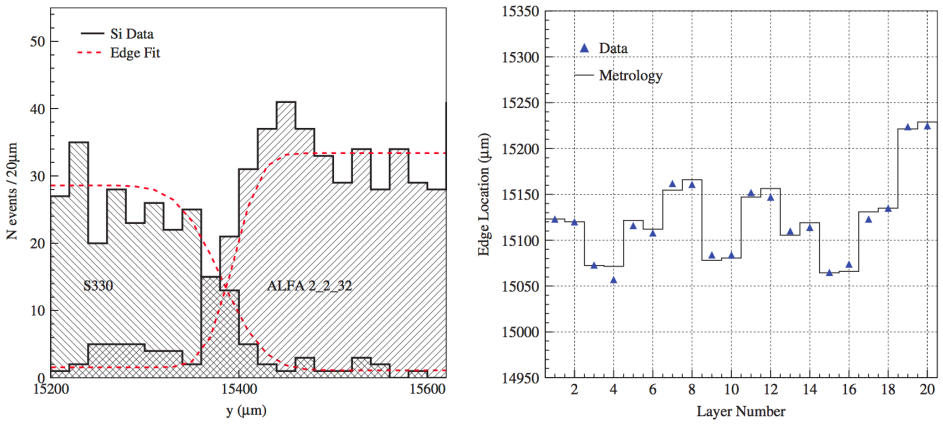

(a) (b)

Figure 4.10: (a) The histograms correspond to the y-coordinate distribution of tracks measured by the telescope on the detector 2_2_32 and the scintillation counter S330 edges. The dashed lines represent the smeared edge functions fitted to the histograms. (b) Comparison between the edge locations of ALFA 10_2_6 obtained by the fit and metrology.

4.3.5 Cross-talk

Two different phenomena giving rise to cross-talk effects are observed with prototypes tested in the 6 GeV electron beam. The first is caused by optical and electron-optical cross-talk while the second is attributed to physics phenomena (see Fig. 4.11).

The propagation of scintillation light from one fibre to the other at the level of the detector is efficiently suppressed by coating them with aluminum. However, optical cross-talk between adjacent MAPMT channels can arise from multiple reflections in the entrance window of the MAPMT and by direct emission of a small fraction of light from a fibre into an adjacent MAPMT channel. The latter is due to light diffusion at the fibre end together with the expansion of the light cone emitted from the fibre into the 0.8 mm thick MAPMT window. Moreover a very small amount of electron-optical cross-talk is due to charge sharing during the avalanche formation in the dynodes of the MAPMT. All these effects lead to cross-talk signals which are relatively small compared to the hit

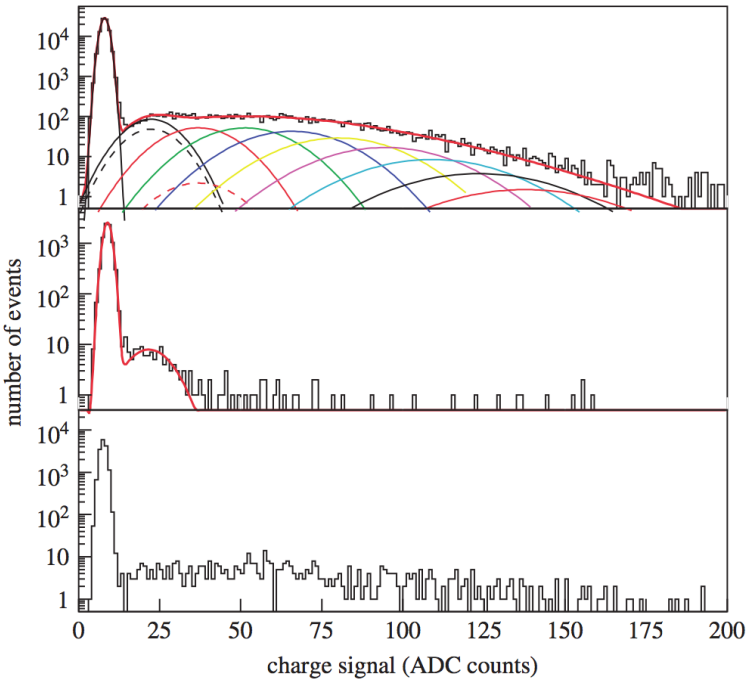

Figure 4.11: Typical spectra for normal hits (top), optical cross-talk (middle) and physics cross-talk (bottom).

signal. With the 6 GeV electron beam the signals are of the order of 4 photoelectrons and the cross-talk signals consist essentially of single photoelectrons (see top and middle histograms of Fig. 4.11). The optical cross-talk probability is determined by selecting hits above a 5 σ pedestal cut in an arbitrary MAPMT channel. The average number of photoelectrons in the adjacent 8 channels (4 direct and 4 diagonal) divided by the value in the arbitrary central channel defines the cross-talk contributions. For the baseline fibre they are of the order of 1.3% for direct neighbours and 0.4% for diagonal.

Table 4.6: Results of the cross-talk (CT) studies. The two optical CT values correspond to direct and diagonal neighbours on the MAPMT. The three values for the physics CT are for the first, second and third neighbouring fibres in the same layer. In the case of the SCSF-78-SJ 1 mm fibre the detector layer has only 6 fibres in total.

Fibre type	Optical CT (%)	Physics CT (%)
Kuraray SCSF-78-SJ	1.3, 0.4	3.7, 1.3, 0.9
Kuraray SCSF-78-SJ 45° 0.5 mm gap	1.4, 0.5	4.1, 1.4, 1.0
Kuraray SCSF-78-SJ 45° 1.0 mm gap	2.4, 0.8	4.4, 1.3, 1.2
Kuraray SCSF-78-SJ 1 × 1 mm^2 45°	1.6, 0.6	4.4, 2.2
Bicron 612 BCF-12SC	1.0, 0.4	2.8, 0.7, 0.5
Bicron 612 BCF-12MC	1.0, 0.4	1.8, 0.4, 0.3

The second phenomenon is observed as symmetric cross-talk from the hit fibre to the neighbours in the same layer. However, the signal spectra in adjacent fibres of the

same layer show amplitudes comparable to the amplitude in the central fibre (see top and bottom histograms of Fig. 4.11). The quantity of these subsidiary hits decreases rapidly with the distance from the central fibre. These cross-talk hits are attributed to δ-electrons hits which are produced by incident beam electrons upstream in the set-up and in the detectors (see Section 2.2). A detailed study of the knock-on probability[138] between a charged particle and quasi-free electrons in detector 10_2_6 with 6 GeV electrons has been performed[134]. It shows that a total of 4.54 δ-rays per 6 GeV electron crossing the detector is expected. This confirms that multiple scattering is in part responsible for correlated background. The physics cross-talk probabilities are determined by selecting hits in a central fibre with a 5 σ_{ped} cut, corresponding to approximately 0.7 photoelectrons, and calculating the ratio of hits, with the same cut, in the three adjacent fibres on both sides. For the baseline fibre, Kuraray SCSF-78-SJ, the adjacent fibres showed an average probability of about 3.7%, the second neighbours a probability of the order of 1.3% and the third approximately 0.9%.

Typical signal spectra showing normal hits as well as optical and physics cross-talk hits are shown in Fig. 4.11. The probabilities of cross-talk for different fibre types and detector configurations are presented in Table 4.6.

4.4 Overlap detectors

To verify the proposed alignment method with overlap detectors and to demonstrate the achievable resolution, two prototypes[108] were built and characterized in a high energy proton beam line at the CERN North Area H8 during the second ALFA beam test campaign[110].

The design of the prototype detectors follows the final design proposal but with only 2 planes per detector instead of 3 due to the limited number of MAPMTs available for the test beam. The prototypes are built with the baseline fibre (Kuraray SCSF-78-SJ) and MAPMT (Hamamatsu R7600-00M64). They are made of two sets of two planes with 30 horizontal fibres on each side of the planes (left and right). Their active area of 6 $\times$ 15 mm^2 is defined by two independent trigger counters placed in front of the fibres (see Section 4.5). A single set of two planes staggered vertically by 500 μm / 2 = 250 μm defines one overlap detector with an intrinsic spatial resolution in y of about 72.2 μm (= 250 μm / $\sqrt{12}$). The 60 fibres on each plane are read-out by a single 64 channels MAPMT leaving 4 channels unused on every photomultiplier.

4.4.1 Construction and metrology

The prototype overlap detectors are fabricated following the same procedure as for the trackers (see Section 4.3.1) with an additional step for bending the fibres. Details of the metrology campaign necessary to define the exact positions of the fibres for data analysis are presented in Appendix C. The construction sequence is the following:

1. LASER cutting of the central and stiffener plates from Al_2O_3 ceramic sheets at a precision of about ± 30 μm.
2. Survey of the plates' geometry and selection of the best matching sets.
3. Glueing of the ceramic plates.
4. Machining and aluminum coating of the fibre ends.
5. Aluminum coating of the fibre sides.
6. Bending of the coated fibres.
7. Alignement and glueing of the fibres.
8. Survey for control of the fibres position, pitch and angle.
9. Glueing of the support blades on the plates.
10. Survey of the fibres positions and angles relative to the precision holes of the steel blade.
11. Assembly of the two plates of OD1 on a support arm through two precision pins. The staggering between the plates is obtained by offsetting the precision holes in the two support blades.
12. Assembly of the two plates of OD2 on a micrometric translation table fixed on the support arm holding OD1.
13. Threading of the fibres into the connector and subsequent glueing. Mapping of the fibres in the connector avoids that adjacent fibres on the plates are connected to adjacent MAPMT channels.
14. Machining with a diamond tool of the protruding fibre ends on the connectors.

Optical cement (Bicron BC-600) is used to glue both the fibres and the ceramic plates. The geometrical data measured during the final survey of each detector was recorded in geometry files and later used during the data analysis for defining the tracks used for reconstruction the relative displacement of OD2 with respect to OD1 (see Section 4.4.2). All prototypes were tested in a laboratory experimental set-up where the bent fibres were exposed to an ^{90}Sr source and read-out by an MAPMT. The results of these tests showed that their light yield is equivalent to the light yield of the straight fibres

of the tracker prototypes. This gave promising indications of light yield and uniformity of the overlap detectors before the test beams.

4.4.2 Relative position monitoring

To validate the reconstruction method with overlap detectors, the two prototype overlap detectors were mounted one in front of the other in a test beam line at CERN[139]. A micrometric screw was used to move vertically the overlap detector upstream (OD2) with respect to the detector downstream (OD1). The relative displacement was monitored by means of a mechanical comparator with a precision of the order of 10 μm.

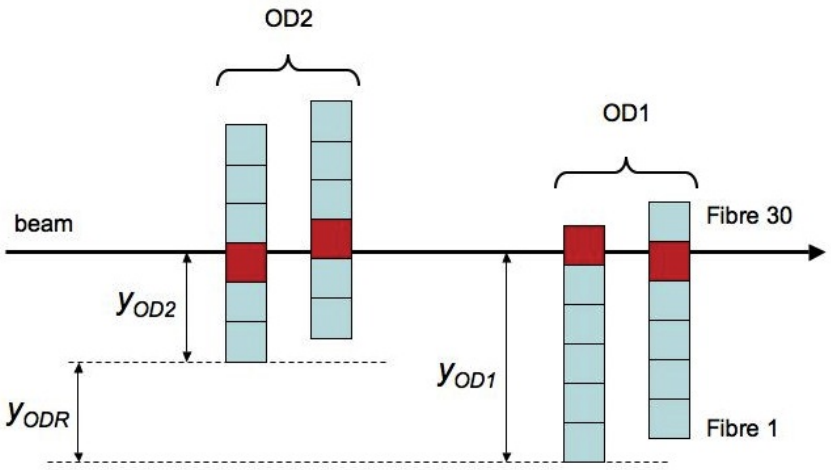

Figure 4.12: Position reconstructed from the relative position of the two overlap detectors.

The vertical distance between the two overlap detectors is reconstructed as the averaged difference between the positions of the fibres hit on each OD as shown in Fig. 4.12

$$y_{ODR} = \frac{1}{n} \cdot \sum_{i=1}^{n} \left(\frac{1}{2} \left(y_{OD2,1} + y_{OD2,2} \right) - \frac{1}{2} \left(y_{OD1,1} + y_{OD1,2} \right) \right)_i \tag{4.3}$$

where n is the number of selected events and $y_{ODk,l}$ is the position of the fibre hit in the layer l of the detector k. The n events are selected on the basis of the number of hit fibres. A tracking algorithm selecting only events with a total of four hits (one on each plane) was implemented. These tracks are then used for the position reconstruction. Good correlation is found between the reconstructed y_{ODR} and the set value y_{set} (see Fig. 4.13a). The difference between y_{ODR} and the straight line fit, plotted in Fig. 4.13b, is smaller than 20 μm. The results obtained in this test beam validate the concept of the

overlap detectors for the symmetric positioning of the ALFA detectors halves relative to the beam.

4.5 Trigger counters

Trigger counters for the ALFA tracking and overlap detectors consist of 3 mm thick plastic scintillators with dimensions corresponding to their active area. The scintillation light is transported to the photodetectors via light guides.

During the 2006 test beam[110] at CERN, detectors 2_2_64 was equipped with a prototype trigger scintillator whose shape matched the overlap area of the 2 × 64 fibres. The trigger counter was made of 3 mm thick plastic scintillator (Bicron BC-408) and it was connected to a PMT (Hamamatsu H3164 PMT assembly) with an active diameter of 8 mm via a specially formed PMMA light guide to cope with the limited space inside the pot. The PMT was mechanically attached to the detectors. Both the scintillator tile and the light guide were wrapped in a thin aluminum foil. The photoelectric yield of this assembly was measured to be of the order of 50 photoelectrons. Setting the threshold around 5 photoelectrons during the test beam guaranteed a very uniform trigger efficiency. Similar trigger counters were used with the overlap detectors. In this case the trigger were shaped into 6 × 15 mm rectangles. This configuration gave excellent results during the test beam both for the overlap detectors and for 2_2_64. However when preparing the full scale detector to be inserted in a roman pot for the 2008 test beam campaign (see Section 4.7), preliminary tests showed that the PMT could not be operated in the secondary vacuum of the pot of the order of 100 mbar due to discharges between the dynodes' pins.

Alternative configurations allowing the PMT to stand out of the pot were studied during a dedicated test beam campaign at DESY in 2007[111]. The trigger tiles under study consisted of the same 3 mm thick plastic scintillators (Eljen EJ-200) that were used in the 2006 test beam but instead of wrapping them in aluminum foils alternative coating solutions were studied. Some tiles were left uncoated, others were aluminum coated on the edges while the rest were fully coated either with a thin aluminum film or with white reflective paint (Bicron BC-620). The light guides consisted of bundles of 250 clear optical fibres (0.5 mm diameter clear-PSM from Kuraray) either glued or mechanically clamped against one or two of the non-coated edges of the tiles (see Fig. 4.14). A trigger tile entirely made of non-coated scintillating fibres (Kuraray SCSF-81) was also tested, in this case the fibres were routed directly to the PMT window with no intermediate optical fibres. Two PMTs of the same series were used (Hamamatsu

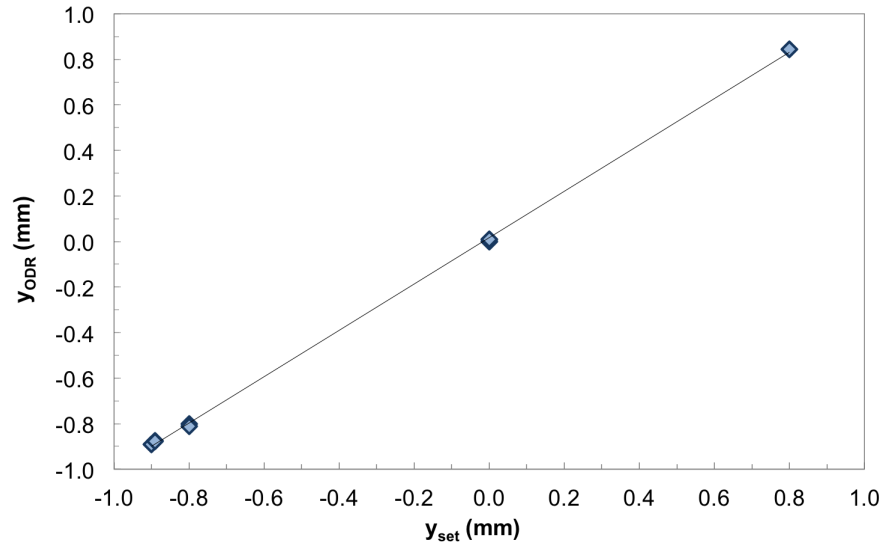

(a)

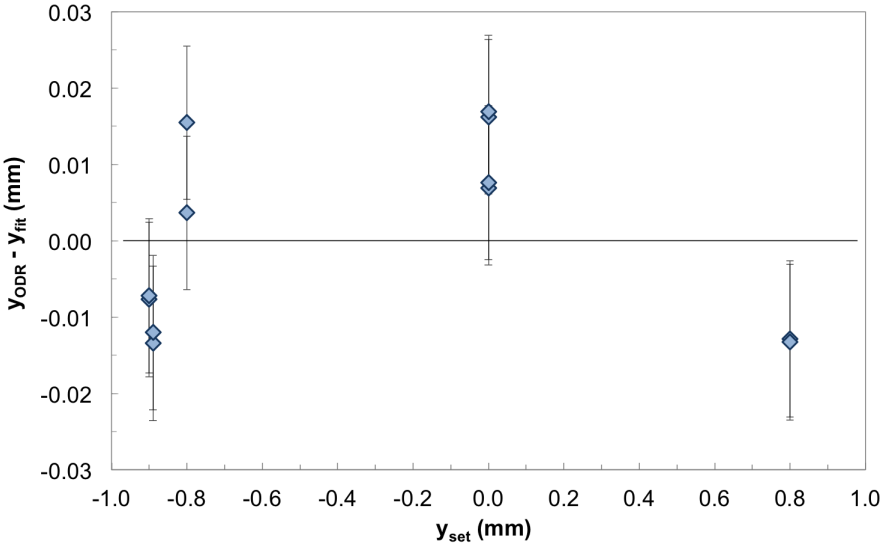

(b)

Figure 4.13: (a) Reconstructed vertical distance y_{ODR} between the two detectors as a function of the mechanically set distance y_{set}. The straight line is a linear fit to the points. (b) Difference between the reconstructed distance y_{ODR} and the fit for the same data. The error bars represent the quadratic sum of the errors from the reconstruction algorithm and the errors of the mechanical measurement.

R7400 and R7401). The only difference between the two PMTs being the effective photocathode size. R7400 has a 9 mm diameter photocathode and it can only read-out a single bunch of fibres, coming from one side of the trigger tile. The other PMT, R7401, is identical except for the fact that it has a lens in front of the photocathode which increases its effective size to 14 mm. It is thus possible with this PMT to read-out two fibre bundles coming from the two opposite sides of a tile. This read-out scheme gave surprisingly low light yields and it was discarded.

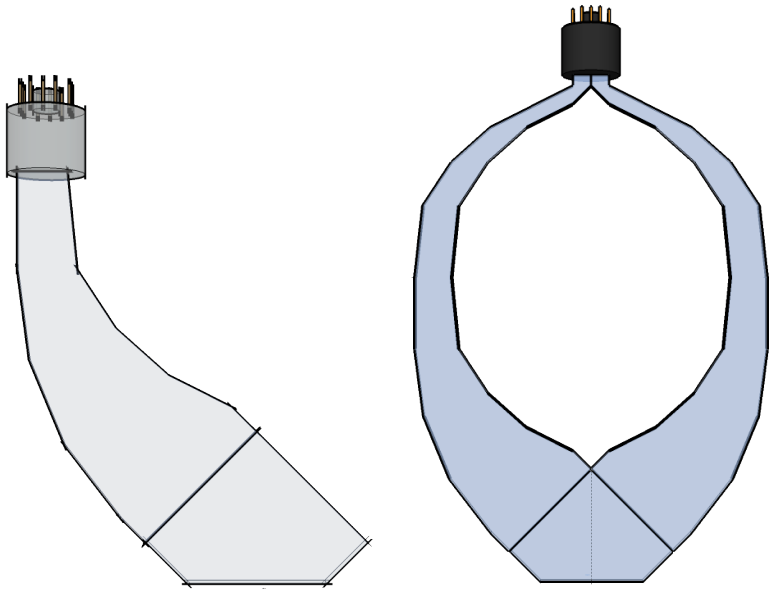

(a) (b)

Figure 4.14: Drawings, not to scale, of the scintillating trigger tiles read-out by (a) a single bunch of 250 optical fibres with the PMT R7400 and (a) a double bunch of fibres with PMT R7401.

Different combinations were assembled and exposed to a 6 GeV electron beam and to study their detection efficiency, uniformity and edge sensitivity. Best results were obtained with the white painted tiles which achieved light yields of the order of 40 photoelectrons (see Fig. 4.15). Bare tiles and aluminum coated tiles yielded approximately 30 photoelectrons while tiles made of scintillating fibres yielded only about 20 photoelectrons. These results were confirmed within 15% by measurements with cosmics at CERN.

Trigger counters consisting of white painted tiles with fibre bundles glued on their sides and read-out by R7400 PMTs were adopted for the 2008 full scale detector experimental campaign[113] both for the tracker and the overlap detectors.

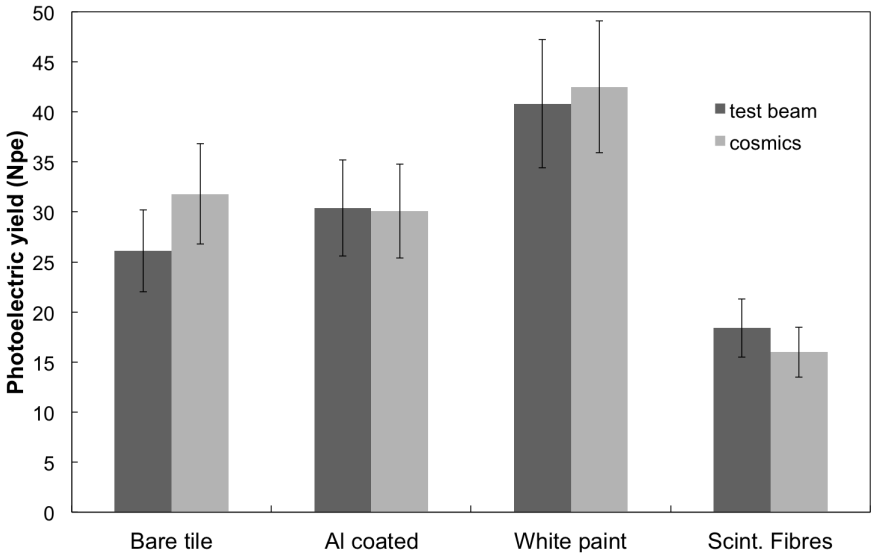

Figure 4.15: Photoelectric yield of various trigger counter configurations measured with 6 GeV electrons and cosmics. The best results are obtained with white painted trigger counter tiles.

Preliminary studies of alternative solutions consisting of the same 3 mm thick trigger tiles read-out by SiPMs, instead of PMTs, mounted directly on the sides of the trigger tiles show good results and are envisaged for future developments. This configuration has the advantage not to require any light guide to transmit the trigger scintillation light out of the roman pots since the photodiodes can operate in the secondary vacuum of the pots.

4.6 Magnetic shields for MAPMTs

As described in Section 3.4.2, the magnetic field during normal operation will be negligible at the location of the ALFA roman pots. However, given the high sensitivity of MAPMTs to magnetic fields, especially along the z-axis, the use of a magnetic shield will increase the safety margin and prevent any possible gain or efficiency loss.

Photomultiplier tubes are extremely sensitive to magnetic fields and exhibit output variations even from fields as weak as the earth's field (approximately 0.5 G). This sensitivity is due to the low average energy of the electrons traveling a long path in the vacuum of the tube. Exposure of PMTs to external magnetic fields result in distortion of the electron trajectories. This can lead the photoelectrons, emitted from the photocathode, away from the first dynode, resulting in losses of efficiency. In the case of MAPMTs this can also lead to cross-talk if the photoelectrons are deviated towards the first dynode of another channel. The magnetic field can also affect the gain

when secondary electrons are deviated from their trajectory before reaching the next dynode. Moreover, temporary exposure of phototubes to magnetic fields can lead to magnetization of their elements. To ensure stable operation of PMTs in magnetic fields, they are usually inserted into shielding cases which protect them from the influence of external fields. These shields are made of materials with very high permeability to guide the magnetic flux inside the material itself leaving regions of low field within the shield enclosure. The magnetic field inside the shield can be attenuated by factors up to 1/10000 of that outside. The shielding efficiency S is defined as the ratio between the magnetic field strength H_{out} outside the shield and the strength H_{in} inside of the shield

$$S = \frac{H_{out}}{H_{in}} \tag{4.4}$$

In general, a good shielding applies to the case in which the shield is sufficiently long with respect to the overall length of the PMT. Near the edges of the case the shielding efficiency is not good and the field attenuation is very low, as plotted in Fig. **??**. Since the effect of an external magnetic field can be most harmful on the photoelectrons traveling from the photocathode to the first dynode, this region of the vacuum tube has to be carefully shielded.

Due to the limited space available in the LHC tunnel around the roman pots, a perfect shield cannot be implemented around the MAPMTs. The maximum length available for the shields is limited to 22 mm which is not sufficient to perfectly shield the 30 mm long MAPMT. Figure 4.16 shows the field attenuation inside a 22 mm long square-shaped shield made of 1 mm mu-metal plates. One sees that for the ALFA MAPMTs, a perfect shielding is never achieved because the shield is too short. However, given the absence of a magnetic field during operation of the ALFA system in the LHC tunnel and the limited space available around the roman pots, placing the photocathode inside a shield, at a distance of 6 mm from the edge, should be sufficient. At this position, the attenuation is of the order of 50% both for longitudinal and transverse fields.

In order to optimize the design of magnetic shields, a finite element analysis with the MAFIA software package[140] was performed[112]. Three configurations with 25 individual housings have been studied (see Fig. 4.17). The first consists of 25 individual boxes for each MAPMT. The second configuration consists in a 5×5 grid made of 12 imbricated mu-metal plates and the third is identical but with two plates separating the MAPMTs instead of one. The configuration made of 12 imbricated plates is the less efficient while the 2 others give roughly the same results. However the individual cases are

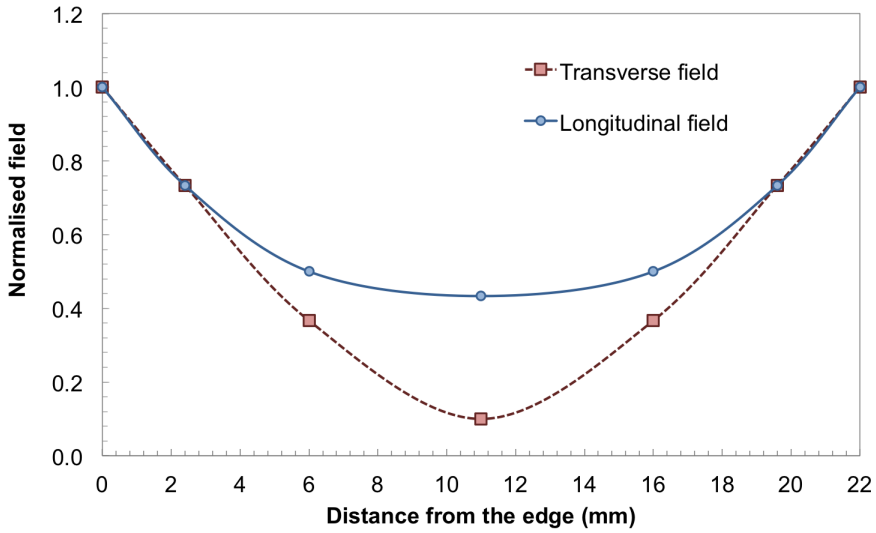

Figure 4.16: Normalised field inside a 22 mm long magnetic shield for tangential and transverse external magnetic fields. At 6 mm from the edge, corresponding to the nominal position of the photocathode, the intensity of external fields is attenuated to about 50%. This is sufficient to guarantee an increased safety margin at the location of the roman pots during ALFA runs.

quite complicated to fabricate. To obtain each one of the 25 cases a slab of mu-metal has to be bent 3 times and soldered. The mechanical stress induced in the mu-metal by bending the plates reduces its magnetic properties which can nevertheless be partly recuperated by applying a thermal annealing cycle. The adopted solution is the one with 20 imbricated plates giving the best shielding efficiency. It is fabricated by moulding a grid in a non-conductive epoxy frame (Ciba CW-229-3). This grid ensures electrical insulation of the metallic bodies of the MAPMTs which are biased to the same potential as the photocathode, typically of the order of 1 kV. Plastic spacers are screwed directly into the frame to precisely position the MAPMTs in front of the fibre connectors

Such a shield grid was fabricated and used to precisely position and shield the 23 MAPMTs during the 2008 ALFA test beam (see Section 4.7). All the shields used for the roman pots installed in the LHC were fabricated following these design and procedure.

4.7 Full scale detector in a roman pot

The first complete ALFA prototype was tested in a roman pot with hadrons in 2008 at CERN[113]. An ALFA station was equipped with the upper roman pot in which a full size tracking detector (10_2_64) consisting of 10 planes with 2 layers of 64 fibres each

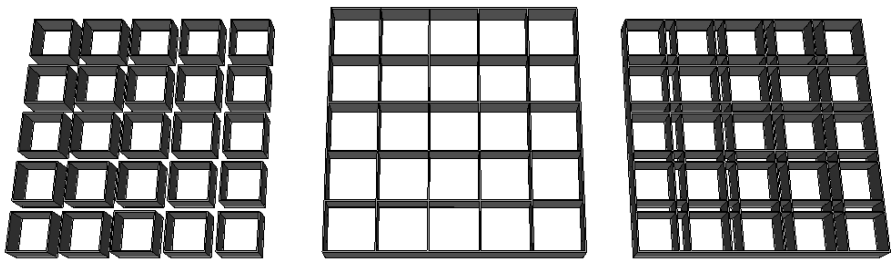

Figure 4.17: Magnetic shields grid configurations studied for the ALFA MAPMTs.

and a full size overlap detector with 3 planes containing 2 layers of 30 fibres on each side (left and right) of the tracker were inserted together with their respective trigger counters. The 23 MAPMTs necessary to read-out the 1280 fibres from the tracker and the 180 fibres of the overlap detector were housed in a mu-metal grid on top of the baseplate containing the fibre connectors. PMFs were mounted directly on top of each MAPMT and their signals were sent to the motherboard via flat Kapton cables. From the motherboard the formatted data was transferred to the central data acquisition. The full assembly was inserted the H8 beam line of the CERN SPS North Area with a 200 GeV π^+/p beam.

Due to problems with the motherboard the test beam started with data taken with two test boards only able to read 5 PMFs each. The layer efficiency was of the order of 90% and the resolution for the 10 layers, read-out by the 10 PMFs, out of the 20 layers available, was about 52 μm both for x and y coordinates. After intensive debugging the motherboard was patched and could be used with some remaining defects which lead to a layer efficiency not better than 70% and the possibility to read only 17 out of the 20 fibre layers. However due to the low layer efficiency in this case the tracks could not be reconstructed with a resolution better than about 55 μm in x and 53 μm in y. With both read-out scenarios the cross-talk was of the order of a few percent as expected with the biggest contribution coming from neighboring MAPMT channels.

Since only one pot was equipped with detectors the relative position reconstruction with the overlap detectors could not be studied during this test beam. Instead the efficiency and spatial resolution of the complete overlap detector with 3 layers in the upper pot was measured. The layer efficiency obtained was of the order of 90% as with the main detector but the spatial resolution was not better than 180 μm instead of the 48 μm (= 500 μm / 3 /$\sqrt{12}$) expected with 3 layers of fibres. Partly this can be attributed to the large noise and cross-talk levels due to the low threshold settings during the overlap detector runs. Mapping problems of the overlap detector fibres and channels might

also be a reason for the bad resolution but they could not be disentangled due to the limited statistics that we could accumulate with these detectors (only 50 000 events during three dedicated runs). Moreover deviations up to 250 μm from the nominal fibres positions were measured on the overlap detectors as well as on the main tracking detectors studied during this experimental campaign.

4.8 Conclusions

A series of experimental studies conducted on different types of plastic scintillating fibres have validated the choice of the 0.5 mm square fibre SCSF-78-SJ manufactured by Kuraray in combination with the MAPMT R7600-00-M64 by Hamamatsu as the baseline for the ALFA tracking detectors. Small-scale prototype detectors fabricated with these fibres have shown promising results. The spatial resolution of the prototype trackers was about 33.5 μm with 6 GeV electrons and 25 μm with 230 GeV protons in agreement with the 30 μm required. No significant dead space at the edge of the detector was identified. Prototype overlap detectors were tested with 230 GeV protons achieving a vertical relative alignment with a precision better than 20 μm. This result validates the proposed solution to monitor the position between the upper pot and the lower pot as they will approach the LHC beam with overlapping tracking detectors. The adopted trigger counters configuration for both the trackers and the overlap detectors consist of plastic scintillators placed in front of the fibres to define the active areas. They guarantee a very uniform trigger efficiency over the whole detection area.

4.9 Outlook

The results obtained with small-scale prototypes demonstrate the feasibility of building a tracking detector system, based on scintillating fibres, that would achieve a spatial resolution of 20-30 μm required for the precise measurement of the absolute luminosity of the LHC at the ATLAS interaction point. However the production difficulties related to the precise positioning and gluing of large sets of thin fibers on support plates, as well as to the insertion of assembled plates in the limited space inside the roman pots, make it very challenging to successfully assemble a full-scale detector with comparable resolution.

These challenges were first evidenced in 2008 with the results obtained with the first full-scale tracking detector[113] and in 2009 when a full roman pot station was tested in a hadron beam at CERN[141]. The spatial resolution of detector 10_2_64 was of the order

of 52 μm. This result should be compared to the resolution of about 25 μm obtained in a previous test beam with the smaller detector 10_2_16. Both detectors have 10 planes of 0.5 mm fibres leading to a theoretical resolution of the order 14.4 μm. The difference between the two detectors is the number of fibres per plane, 16 for detector 10_2_16 and 64 for 10_2_64. The difference in resolution has been attributed to the positioning of the fibers. Metrology studies indicated deviations from nominal positions of up to 250 μm in the planes of 64 fibres of detector 10_2_64, strongly impacting the spatial resolution.

On a larger scale the full roman pot station constructed for the 2009 test beam revealed other challenging aspects related to the limited space available inside the roman pots with respect to the size of the assembled detectors. The station was made of 2 roman pots with complete tracking detectors and partial overlap detectors from the series to be installed in the LHC. Only 2 of the 3 plates per overlap detector could be mounted because of a mismatch of the detector alignment and pot production precision problems.

Despite the difficulties described above the roman pot stations have been installed and connected to the LHC beam-line and vacuum system. Preliminary data was recorded from the LHC beams in 2010 with the first detector installed. The detectors of the three other stations have been installed during the LHC winter shutdown 2010-2011 and the first data from the complete ALFA system is expected in 2011.

Chapter 5

Scintillation particle detection based on microfluidics

This chapter reports on the design, fabrication and characterization of a novel type of liquid scintillation particle detector based on microfluidics and microfabriation technologies. It describes the results of the experimental investigation performed on two generation of prototype detectors that demonstrate the validity of the approach.

5.1 Introduction

A novel type of particle detector based on dense arrays of capillaries filled with liquid scintillators has been developed and studied. Microfabrication technologies have been employed to build thin microfluidic devices with dimensional resolutions of the order of micrometres with a single photolithographic step. Such devices provide a simple and efficient way to control the circulation of fluids inside capillaries overcoming the difficulties encountered with previous high spatial resolution liquid scintillation detectors made of capillary bundles. Moreover, the possibility to circulate and renew the liquid scintillator makes the active medium of the detector intrinsically radiation hard and by changing the type of scintillator in the microchannels the same device can be used for different types of measurements. The experimental results obtained with the prototype devices demonstrate the feasibility of a scintillation particle detector based on microfluidics.

5.2 Goals and Motivation

This work aims at developing a new scintillation detector with high spatial resolution for reconstruction of particle tracks, increased radiation resistance, and low material budget. The proposed approach combines the CERN expertise on the development of particle detectors with the advanced microfabrication techniques mastered at EPFL.

This development relies on the idea of combining two well-known technologies from two different fields. The proposal being to investigate the possibilities offered by the recent progress made in handling fluids in microfabricated devices with capillary-like channels in order to develop a liquid scintillator particle detector. The excellent performance of scintillating fibre detectors under development for the LHC together with the reported results obtained with capillaries filled with liquid scintillators are very promising in this context. In the nineties when tracking detectors based on capillaries filled with liquid scintillators were studied, advanced microfluidic fabrication processes were not accessible to the high energy physics (HEP) community. Even though these types of detectors were considered as good candidates for charged particle tracking in very high radiation environments[142], the difficulties encountered in their production and operation prevented them from overtaking on plastic scintillating fibres detectors. Modern techniques developed at the EPFL Microsystems Laboratory LMIS4 (lmis4.epfl.ch) make it possible today to overcome the practical limitations that stopped the previous developments.

The motivation to propose an alternative scintillation particle detector arises from the technological challenges related to using plastic scintillators, especially in high radiation environments. They suffer mainly from degradation under irradiation and relatively high material budgets inherent to the necessity of staggering multiple planes of fibres in order to increase the intrinsic spatial resolution of the detectors. Moreover the spatial resolution of a particle tracker is directly related to the precise positioning of the fibres and for large arrays of small fibres this can be quite challenging (see Section 4.9) especially in view of scaling the production to a large number of detectors with identical properties. Nevertheless the excellent performance of state-of-the-art scintillating fibre trackers lead this technology to be chosen for the ALFA system (see Section 3.5) while liquid scintillator capillary detectors were discarded for LHC detectors. However, based on the good results obtained with liquid scintillator capillary detectors (see Section 5.3) and recent developments in microfluidics, a new type of detector was investigated (see Section 5.4) and its feasibility was demonstrated (see Section 5.5).

5.3 Liquid scintillation capillary detectors

Several studies have shown that detectors based on capillary bundles filled with liquid scintillators are quite competitive with respect to plastic scintillating fibres devices[143]. They consist of capillaries manufactured out of a low refractive index material and filled with a higher refractive index liquid scintillator. With an appropriate choice of shape and an adequate difference in refractive indexes, one can make the capillaries act as waveguides to conduct the scintillation light to connected photodetectors. Liquid scintillators are fast, efficient and exhibit a good radiation resistance which makes them particularly interesting for particle tracking[59] and calorimetry[144] in HEP experiments.

Several attempts have been made in the past to produce complete devices[53;54;145]. The construction of these detectors started with the production of macro-capillaries of borosilicate glass with a diameter of the order of 1 mm (see Fig. 5.1). Many capillaries were packed together and drawn at high temperature to obtain a coherent array of micro-capillaries fused together. Several arrays were assembled together and drawn once more to give the final bundles with capillary diameter of the order of 20-30 μm. Capillary layers could then be constructed by aligning and gluing the bundles while trying to minimize the dead space in between. Finally the layers were cut for a good optical contact to the photodetector window and the capillaries were filled with a liquid scintillator. Even though good experimental results have been obtained with such capillary detectors (see Fig. 5.2), their implementation was rather complicated

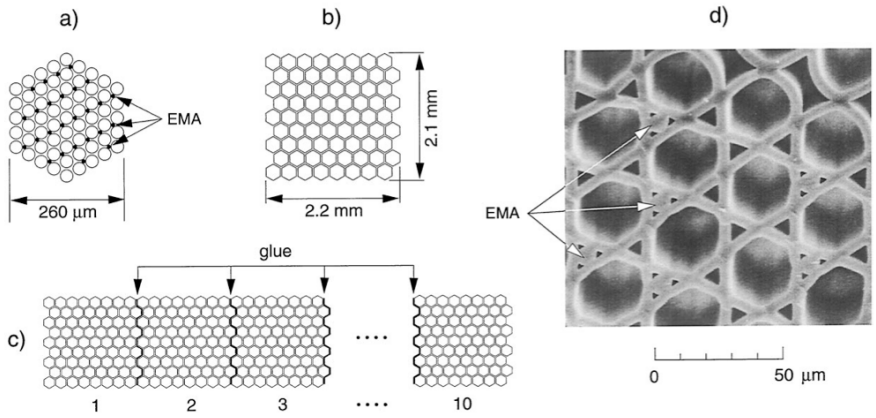

Figure 5.1: Cross sectional views illustrating layer construction: (a) a mini-bundle of 61 capillaries, with EMA present in a fraction of the inter-capillary spaces; (b) a layer element, consisting of 8Y9 mini-bundles; (c) a capillary layer, formed by gluing together 10 elements; (d) detail of a mini-bundle, photographed through an electron microscope[143].

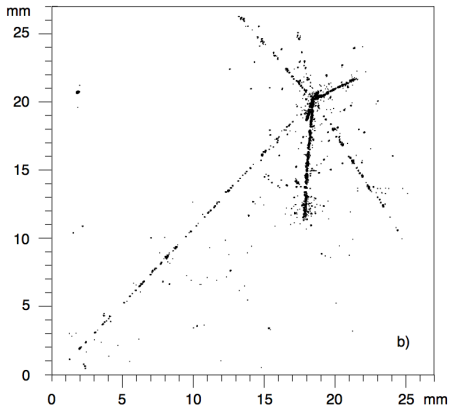

Figure 5.2: Neutrino interaction event[145].

and many imperfections could arise during each step of their fabrication process(see Fig. 5.3).

5.4 Microfluidic scintillation detection principle

As mentioned before, the main goals for the particle detector investigated are high spatial resolution for the precise reconstruction of particle tracks, high radiation resistance to operate in very high radiation environments and low material budget to minimize the interferences with impinging particles. Microfabrication and microfluidic technologies are appealing to develop such detectors. With a simple process it is possible to fabricate a single microfluidic channel defining a dense array of optically independent scintillating capillaries that can be coupled to dedicated photodetectors (see Fig. 5.4).

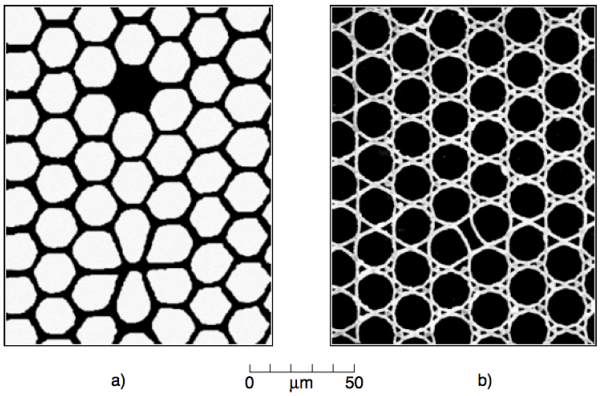

Figure 5.3: Microscope picture of the cross section of capillary arrays. Areas with defects have been selected[145].

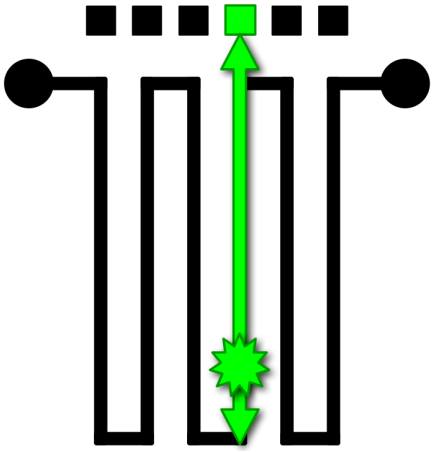

Figure 5.4: 2D schematic representation of the principle of operation of the microfluidic scintillation detector. A single microfluidic channel defines an array of optically separated waveguides. When a particle interacts with the liquid scintillator in one of the branches the scintillation light is guided towards the corresponding photodetector.

The design is based on the assumption that there is negligible light transmission between the different capillaries due to the sharp angles of the single fluidic channel. Fluidic operation of the microfluidic channel is straightforward and liquid scintillators can be circulated, renewed and exchanged.

5.5 Prototype detectors

The prototype detectors investigated consist of single layers of microfluidic channels with a thickness of the order of 200 μm. The microchannel design defines 50 μm wide waveguides separated by 10 μm wide SU-8 walls. Due to the fact that the only photodetector available for our experimental setup was the MAPMT H7546B by Hamamatsu

with a pitch of 2.3 mm, we had to implement an *ad-hoc* microfluidic layout, different from the nominal design with straight channels, to fan-out the light from the detection area to the photodetector window (see Section 5.5.2).

According to our design, the prototype had to fulfill several requirements. In order to get sufficient light from a single layer of microchannels the particles must interact with enough scintillator. Hence, the channels containing the liquid scintillator should be deep enough. Moreover, once the light is generated it has to be guided inside the microchannel from the interaction point to the photodetector. The walls of the channels should thus have a perfectly smooth surface. Lastly, the light yield has be identical along the channel and independent from the position of the hit. For this reason, all the channels must have identical and constant cross-sections and their walls have to be vertical.

Following these guidelines, various microfabrication processes have been investigated. Finally the prototype devices were fabricated by optimizing a standard SU-8 process, based on a single photolithography step, in order to produce precise vertical structures defining deep trenches in thick layers of photoresists (see Section 5.5.1). The key properties making this photoresist attractive for the fabrication of dense arrays of scintillating waveguides are the possibility to uniformly expose thick layers and obtain smooth vertical sidewall profiles with good dimensional control over the entire structure height. Of particular interest for this project is the high aspect ratio (up to 1:30) that can be achieved on thick layers of the order of 200 μm with low roughness vertical sidewalls[146;147]. Moreover, its high level of resistance to radiation damage, comparable to Kapton film, makes it a good candidate for novel microfabricated radiation detectors[148].

Other types of processes such as etching in silicon, Pyrex, and quartz substrates were discarded for the fabrication of single layer prototype devices for different reasons such as the roughness of the sidewalls and the insufficient depth of the channels. However they could be of interest for the fabrication of detectors in future developments.

5.5.1 Fabrication of metallized SU-8 microchannels

SU-8 is a versatile photosensitive material which is used in a wide range of applications (see Section 5.5.1.1). The processing of SU-8 is rather simple and straight-forward (see Section 5.5.1.2). It starts with the spin coating of the resin on a substrate followed by a soft bake, the exposure, and a final hard bake. Another bake is performed after the exposure before developing the resin. The various parameters of this fabrication process

have been optimized in order to obtain a dense array of thin walls of the order of 10 μm with high aspect ratios of about 1:20 over lengths up to 10 mm[149] (see Section 5.5.1.3). These 200 μm high structures are separated by 50 μm gaps which makes the fabrication process and in particular the development step rather challenging. The gap between the walls defines the actual size of the channel to be filled with liquid scintillator. Microfluidic chips with rectangular waveguides 50 μm wide and 200 μm high separated by 10 μm wide straight walls were obtained.

5.5.1.1 The SU-8 photoresist

SU-8 is a negative-tone epoxy based photoresist. It is prepared by dissolving an EPON SU-8 epoxy resin (from Shell Chemical) in an organic solvent like gamma-butyrolactone (GBL). The resin is photosensitized with a triaryl sulfonium salt. The amount of solvent determines the viscosity grade which allows a wide range of thicknesses from tens of nanometers to millimetres. Upon UV exposure and thermal treatment the highly cross-linked structure gives SU-8 a high thermal stability and good chemical resistance.

Polymerization of SU-8 is based on chemical amplification. A single photoevent, known as protolysis, initiates the cascade of subsequent chemical reactions inducing the polymerization (photo-polymerization). The chemical reactions in SU-8 involve the use of a strong acid upon UV-exposure which initiates the cross-linking reaction that takes place during a post-exposure bake step. The cross-linking is initiated by the cationic ring opening of epoxy groups by the Lewis acid to initiate several chains. The cross-linking process yields a dense, stable network where each epoxy oligomer is connected to other epoxy functions (see Fig. 5.5).

The main physical and optical properties of SU-8 are summarized in Table 5.1. Its photosensitivity is in the range between 300 to 400 nm and its transparency allows structuring with high aspect ratios and fabrication of near vertical sidewalls with very low roughness. SU-8 is chemically and thermally stable up to 200°C. It has a good adhesion on different types of substrates and a high mechanical strength.

SU-8 has been extensively investigated as a material for the fabrication of microstructures. It can be used as a negative photoresist to pattern other layers or as a structural material in micro-electro-mechanical systems[150;151] (MEMS) and microfluidic devices[152]. Recently it has also been employed for the fabrication of micro-pattern gas detectors[153], X-ray imagers[154] and microfluidic particle detectors[155]

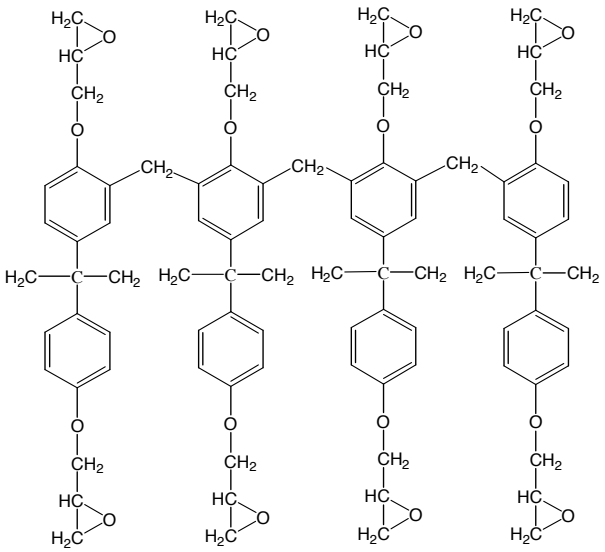

Figure 5.5: SU-8 oligomer.

Table 5.1: Physical and optical properties of SU-8.

Property	Value
Young's modulus E	4.02 GPa (Postbake 95°C)
	4.95 GPa (Postbake 200°C)
Bi-axial Modulus of Elasticity $E/(1-\nu)$	5.18 GPa
Film Stress	16-19 MPa (Postbake 95°C)
Max. Stress	34 MPa (Hardbake 200°C)
Friction Coefficient μ	0.19 (Postbake 95°C)
Glass Temperature T_g	50°C (unexposed)
	$>$ 200°C (fully cross-linked)
Degradation Temperature T_d	380°C (fully cross-linked)
Thermal Expansion Coefficient	52 ppm/K (Postbake 95°C)
Polymer Shrinkage	7.5 %
Refractive index n	1.59 (at 633 nm)
	1.67 (at 365 nm)

5.5.1.2 Standard SU-8 processing

SU-8 photoresist is a negative-tone photosensitive resin for which a standard UV lithography process can be applied to pattern it. Several steps are necessary to microfabricate structures as shown in Fig. 5.6 and detailed in Fig. 5.7.

The UV lithography steps (see Fig. 5.6) are:

- *spin-coating* to dispense the resin on a substrate,
- *pre-bake* (or soft-bake) to evaporate the solvent,
- *exposure* to UV light through a mask to polymerize the desired structures,
- *post-exposure bake* for polymerization,
- *development* to dissolve the non-polymerized resin revealing the structures,
- *hard-bake* (optional) to release the stress in the structures and to increase the level of reticulation.

Multiple layers of SU-8 can be superposed by consecutive spin-coatings after the post-exposure bake, the development or the hard-bake[156].

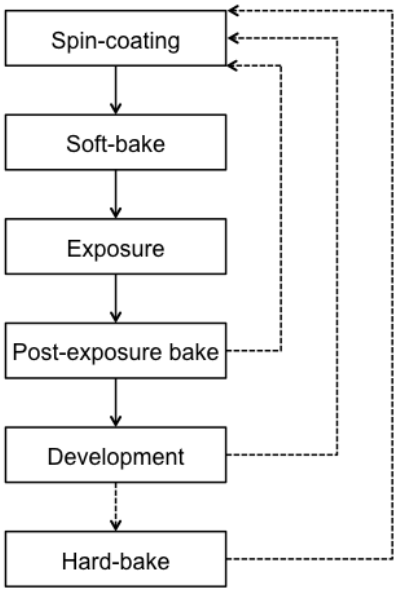

Figure 5.6: Schematic of the processing steps for the SU-8 technology. Dashed lines show alternatives for multi-layers spin-coating.

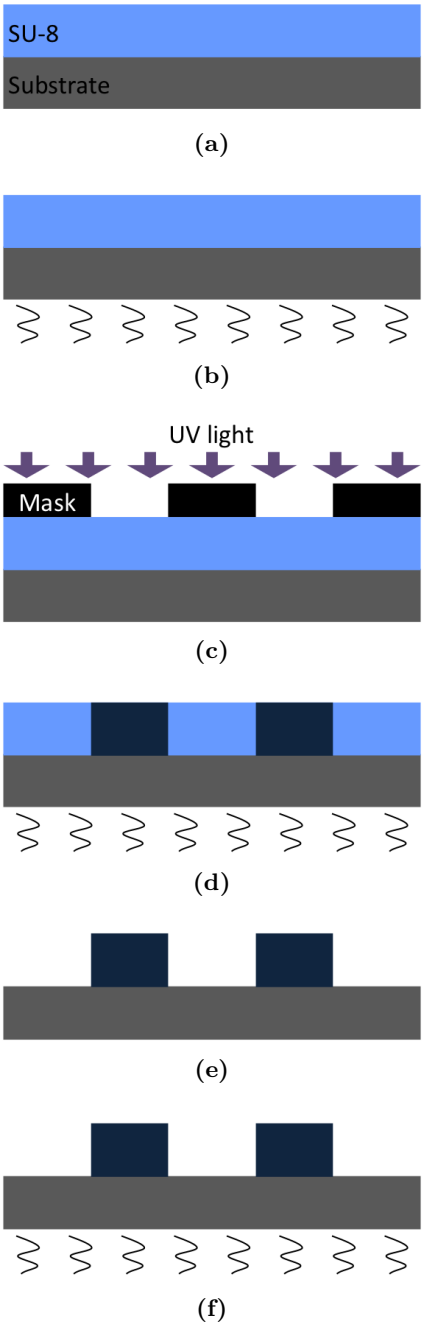

Figure 5.7: SU-8 process-flow. (a) Spin-coating of the photoresist. (b) Soft bake. (c) Exposure. (d) Post-exposure bake. (e) Development. (f) Hard bake.

Spin-coating (see Fig. 5.7a). A controlled amount of photoresist is dispensed on a cleaned substrate and spun. The thickness of the SU-8 layers obtained depends on the formulation's viscosity as well as the speed and time of revolution. Thick layers, typically above 50 μm, leave an edge bead which degrades the exposure conditions. To minimize this edge bead a relaxation time is recommended to improve the overall uniformity of the layer.

Pre-bake (see Fig. 5.7b). During this thermal treatment the solvent contained in the SU-8 formulation is evaporated. This step is performed by heating the substrate above the glass transition temperature T_g of the SU-8 oligomer (see Table 5.1) in order to improve the diffusion of the solvent. Typical temperature is around 95°C for a time defined by the photoresist layer thickness.

Exposure (see Fig. 5.7c). In order to initiate polymerization, SU-8 photoresist must be exposed to UV light, emitting mainly at 365 nm. The irradiation dose depends not only on the layer thickness, but also on the interface nature and structure design. Over-exposure results in better adhesion to the substrate but also to a worsening of the structures sidewall verticality and resolution. It is important to adjust the dose in order to get a good compromise between adhesion and resolution.

Post-exposure bake (see Fig. 5.7d). This thermal treatment induces the polymerization of the SU-8 oligomers in the regions that contain the acid catalyst generated during exposure. It results in a crosslinking of the exposed regions modifying the resist film properties in several ways: shrinkage occurs due to network densification and product outgassing, and the T_g of the system rises. As cross-linking proceeds and the network gradually approaches completion, the polymerization reaction slows down and eventually stops. The T_g of the material is thus dependent on the post-exposure bake temperature. Typically, this bake is performed on a hotplate at a temperature of 95°C for 15 min. To minimize internal film stress, the substrate is slowly heated up to 95°C and cooled down to room temperature with ramps of 4°C/min.

Development (see Fig. 5.7e). The patterns are revealed in propylene glycol methyl ether acetate (PGMEA) to dissolve the non-exposed SU-8. In order to reduce the development time and to increase its efficiency, agitation is recommended but other techniques such as spray can be applied to improve the development, especially for deep trenches. Finally, the substrate is dipped in a fresh PGMEA bath to remove residues

and rinsed with isopropanol. Development time is critical since it may induce some cracks in the structures and their loss of adhesion from the substrate. Well-defined, near-vertical sidewalls can be obtained with a well-controlled process.

Hard-bake (see Fig. 5.7f). This last step is not mandatory however a post-baking of the developed structures leads to a very resistant material. It leads to an enhanced reticulation of the polymer and as a consequence also to better mechanical properties and chemical resistance. Moreover it allows reducing internal stress and cracks present in the SU-8 parts and in many cases they are suppressed by heating above 95°C, typically between 100°C and 200°C, to have a sufficient polymer chain mobility. Great care must be taken in order to avoid thermal shocks inducing structures degradation.

5.5.1.3 SU-8 as a structural material for building waveguides

The fabrication of arrays of waveguides with SU-8 as the structural material has been performed by optimizing a standard SU-8 process-flow. A microfluidic device with 10 mm long and 200 μm thick SU-8 structures having an aspect ratio of 1:20 was fabricated. The patterned microchannels are 50 μm wide and 10 μm wide metal-coated SU-8 walls separate them. This device was used to demonstrate the principle of scintillation particle detection based on microfluidics[155] (see Section 5.5.2).

5.5.1.3.1 Fabrication process-flow Dense arrays of high aspect ratio structures are very sensitive to the process parameters. The SU-8 process described in Section 5.5.1.2 has been studied in order to optimize the various steps to fabricate them. An extra step of metallization has also been implemented to avoid optical cross-talk between neighboring channels separated by the SU-8 structures.

Spin-coating To obtain thick layers of few hundreds of micrometres the SU-8 GM1075 (from Gersteltec) is used. Uniform layers of 200 μm are obtained with rotation speeds of the order of 950 rpm. A dehydration step before spin-coating improves the adhesion of the SU-8 structures to the substrate. This step is recommended especially when small structures with high aspect ratios have to be patterned in the coated layer.

Pre-bake In order for thick layers to be uniform, the evaporation of the solvent requires a well leveled hot-plate. For thicknesses of the order of hundreds of micrometres the pre-bake is performed at a temperature of 120°C, as defined by the supplier, for a

duration depending on the SU-8 layer thickness. Slow temperature ramps of 4°C/min for heating and cooling should be applied in order to avoid the formation of cracks. While for thin layers the relaxation time before the pre-bake is optional, thick layers require a relaxation time of a few hours at room temperature, especially when fabricating high-aspect ratio structures. Best results are obtained when the relaxation is performed overnight.

Exposure Thick SU-8 layers require a rather high dose of irradiation in order to fully polymerize. The polymerized thickness E_p can be defined as follows[157]

$$E_p = E_i \gamma \ln \frac{D_i}{D_c} \tag{5.1}$$

where E_i is the film thickness, γ is the contrast of the photoresist which defines the development rate as a function of the absorbed dose, E_i is the incident dose and D_c is the critical dose below which the resist is entirely dissolved during development.

For 200 μm thick layers the optimal dose was found to be around 360-400 mJ/cm^2. Higher doses lead to a resolution loss of the high aspect ratio structures.

Post-exposure bake The polymerization initiated during the exposure is improved by a thermal treatment of about an hour at 95°C. In order to minimize the internal stresses slow ramps of 4°C/min are applied both for heating and cooling. Leaving the coated substrates at room temperature before this bake has a beneficial effect. During this delay of a few tens of minutes some chemical species diffuse in the exposed parts and lead to a better homogeneity within the resist. Most of the time if the post-exposure bake was performed immediately after the exposure it resulted in undulation and sometimes in stiction of the SU-8 walls (see Fig. 5.8).

Development The development step is critical for the small structures having high aspect ratios. Given the little space between the SU-8 walls the development at the bottom of the channels is difficult due to a low solvent diffusion (see Fig. 5.9a). Bath agitation is essential in order to develop deep trenches. The times required can amount to as much as one hour. Such long times of development are possible because the highly cross-linked exposed SU-8 exhibits a good chemical resistance to the developer with respect to unexposed SU-8. Once fully developed the wafers are rinsed. However due to surface tensions problems can arise during the rinsing step; the thin SU-8 walls are attracted, collapse and stick to each other (see Fig. 5.9b). It was found that an

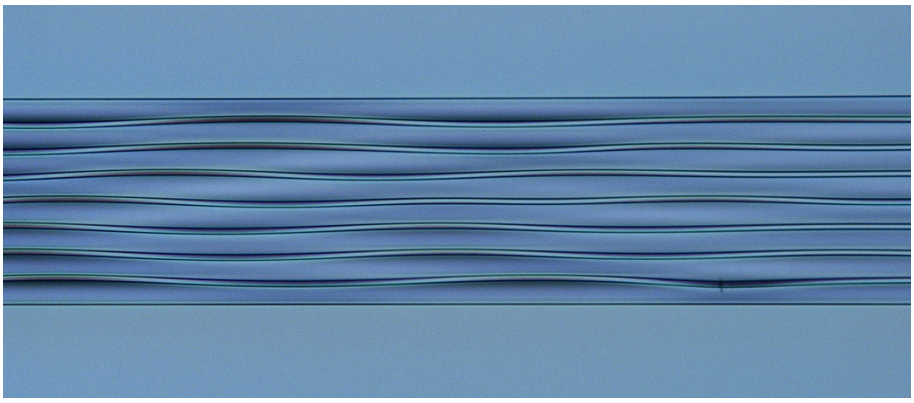

Figure 5.8: Top view of undulating SU-8 walls after post-exposure bake. This phenomenon was frequently observed when no relaxation time was applied between exposure and post-exposure bake.

extra immersion in an ethyl lactate solution for a few minutes before rinsing would solve this problem (see Figs. 5.9c and 5.9d).

Hard-bake Hard-bake improves the polymer reticulation and thus its adhesion to the substrate. It is essential to do this step for long and thin SU-8 walls to release all their internal stress and to strengthen them. In order to minimize the temperature gradient across thick layers of SU-8, the hard-bake is performed at 50°C for about 3 hours in an oven rather than on a hot-plate. Depending on the process conditions and mainly on the structures' shape and resolution, formation of cracks may occur (see Fig. 5.10a) induced by internal stress in SU-8 parts released during the development step. Cracked structures may lead to leakage in microfluidic systems, unwanted scattering and increased propagation loss in optical systems. For thin structures with high aspect ratios, the formation of cracks lead to their destruction. The cracks size and density can be drastically reduced during this thermal treatment and the smallest ones (*i.e.* 5 μm and smaller) can even disappear (see Fig. 5.10b). It was found that a flood exposure of the full wafers with a dose equivalent to the exposure dose before the hard-bake leads to better results in terms of material properties and structures definition.

Metallization To prevent optical cross-talk between adjacent microchannels and to increase their optical properties, guaranteeing an efficient light transmission from the interaction point to the photodetector, the walls and the bottom of the channels are metallized. Two coating methods, evaporation and sputtering, have been considered and in both cases an adhesion layer was not necessary. Sputtering gives the best results

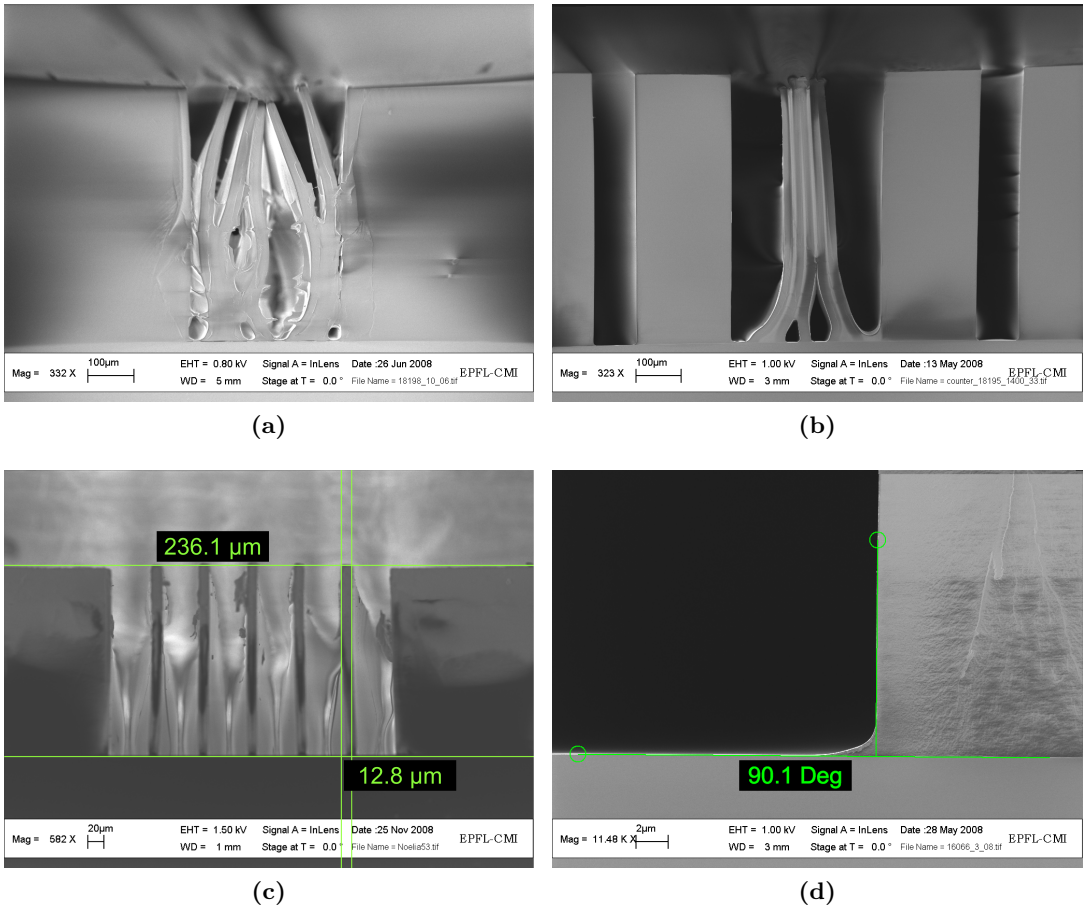

(a) **(b)**

(c) **(d)**

Figure 5.9: (a) SEM image of the cross section of deep trenches not fully developed. The solvent does not reach the bottom of the microchannels and the unpolymerized SU-8 is not completely removed causing the SU-8 ridges to bend and stick to each other. (b) SEM image of the cross section of almost completely developed deep trenches with collapsed SU-8 walls. They usually collapse during the last rinsing step after development. SEM images of the (c) cross section (d) of the bottom of the microchannels. Very smooth and near-vertical side walls are obtained.

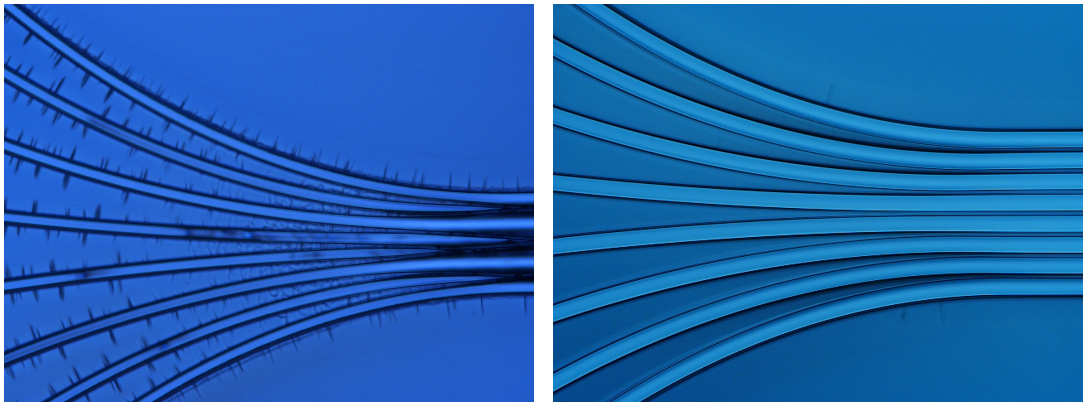

(a) (b)

Figure 5.10: (a) Cracks formed in the SU-8 layer during the process. (b) The density of cracks can be drastically reduced with a hard-bake after the development.

for our design with high aspect ratio structures. It is performed in the Balzers BAS50. However, due to the high aspect ratio of the walls and their close spacing, metallization is not homogeneous along the wall. It decreases with the depth of the channel. To have sufficient metal at the bottom of the channels and on the lower part of the walls, two consecutive metallizations are performed, guaranteeing at least 200 nm of metal at the bottom. The reason to deposit metal in two steps is due to the temperature reached during the sputtering process. A single, long, deposition results in undulation and collapsing of the thin SU-8 walls while two shorter cycles are not harmful. Gold and aluminum depositions have been performed. The results presented in this chapter have been obtained with Au-coated SU-8 microchannels.

At this stage, the wafer is diced to separate 16 chips with a footprint of 15 mm $\times$ 20 mm (see Fig. 5.11). The metal coating is then removed from the side of the chip to be coupled to the photodetectors in order to allow transmission of the scintillation light. Removal is performed by dipping a small portion of the chip in an etching solution.

5.5.2 Experimental set-up

The microfluidic chip is placed in an opto-mechanical set-up to close the channels for microfluidic manipulation and to optically couple them to the photodetectors. The microchannels are closed by covering the chip with an Al-coated Mylar foil and encapsulating the whole in a black PMMA block. Optical gel is used to improve the light transmission between the microfluidic chip and the quartz window of the photodetector. Tubes are connected to the inlet and outlet of the channel through the PMMA block. Filling and circulation of the liquid scintillator in the microchannel is performed with

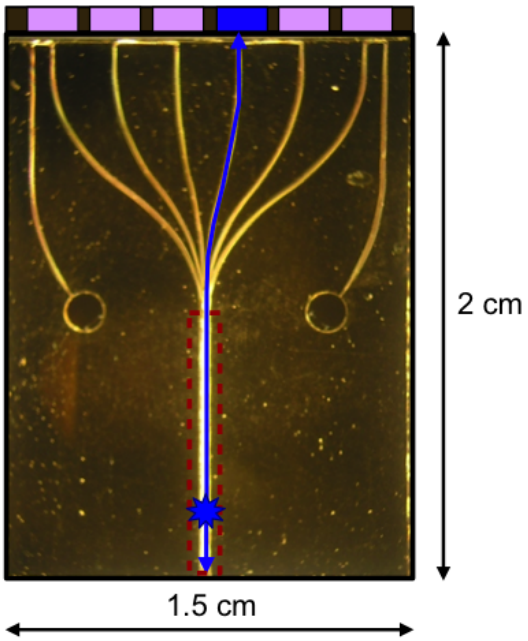

Figure 5.11: Top view of the open metallized SU-8 channels of the prototype microfluidic scintillation detector. The upper side of the chip, in contact with the photodetector pixels, is not metallized to allow light transmission between the microchannels and the photodetector.

a syringe controlled by hand. In a later stage, and in particular for future beam test experiments, a fluidic circulation controlled with a pump will be implemented. The channel is filled with a liquid scintillator (EJ-305 by Eljen Technology) selected for its high light output (80% of Anthracene) and for its emission spectrum peaking around 425 nm in the most sensitive region of the photodetector (MAPMT H7546B by Hamamatsu) of the experimental test bench. The photoelectric yield of the chip-MAPMT assembly is measured by exciting the liquid scintillator with electrons from a collimated ^{90}Sr source which are considered as MIPs (see Appendix B). The coincidence of two plastic scintillating fibres (Kuraray SCSF-78 0.5 mm square cross section), placed underneath the detector and each read-out by a PMT (H3165 by Hamamatsu), is used to trigger (see Fig. 5.12). For each trigger the signals from the MAPMT channels are sent to a multi-channel charge-to-digital converter (CAEN QDC V792).

The microchannel design of the prototype devices defines a detection zone, where impinging particles are detected, with high spatial resolution. 50 μm wide waveguides are separated by 10 μm wide SU-8 structures on a total length of 10 mm (see Figs. 5.13 and 5.14). In this region the microchannels are straight and parallel. They then fan-out from a pitch of 60 μm to a pitch of 2.3 mm over 10 mm to match the inter-pixel distance of the MAPMT (see Fig. 5.15). All the area will be covered by the microchannel

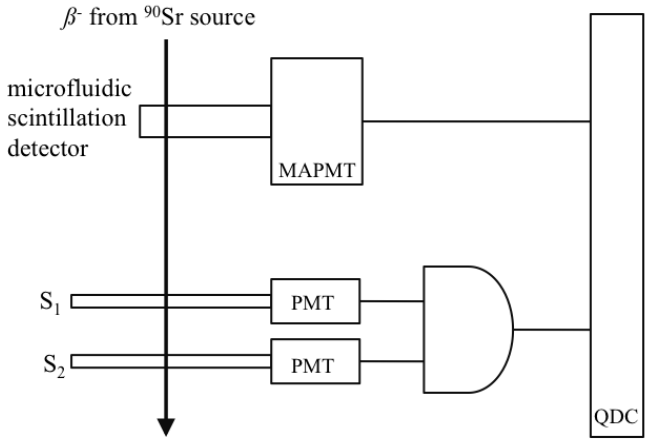

Figure 5.12: Experimental set-up used to demonstrate the principle of the new type of scintillation particle detector based on microfluidics. When a charged particle goes through the trigger scintillators S_1 and S_2 read-out by a PMT each, the coincidence of their signals triggers the photodetector (MAPMT) reading out the microfluidic scintillation chip.

used for detection. The layout of the prototype detector studied here has a reduced detection zone to cope with the pitch of the photodetector available in the experimental test bench, that did not match the distance between adjacent channels.

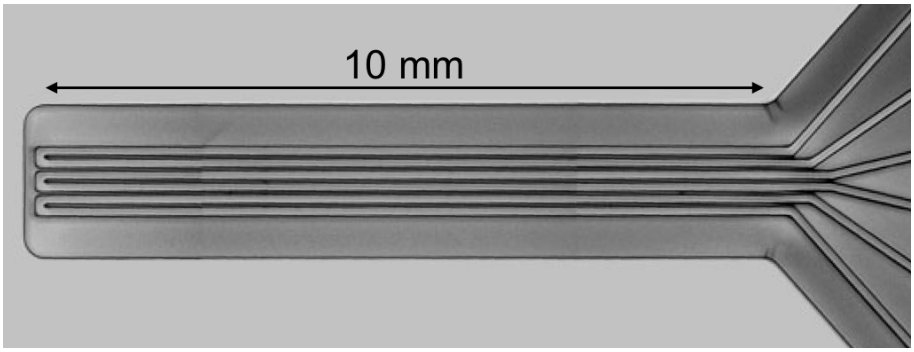

Figure 5.13: Top view of the straight parallel SU-8 walls defining the microchannels.

5.5.3 Results

The spectra of charge read-out from the individual scintillating microfluidic channels (200 μm deep and 50 μm wide) are fitted with the convolution of a Poissonian distribution P describing the fluctuations in the production of photoelectrons with a Gaussian term G describing the response of the read-out electronics to a given number of photo-

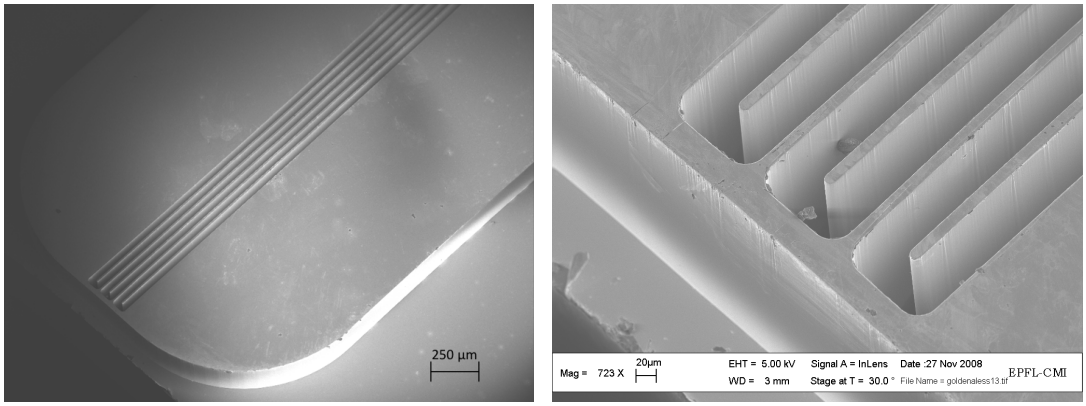

(a) **(b)**

Figure 5.14: SEM images of the microfluidic channels corresponding to the detection zone of the microfluidic scintillation chip.

electrons as developed in Section 2.4.1. The charge distribution contains also a pedestal term, corresponding to the cases where the read-out was triggered by an electron passing by a neighboring channel (due to the larger size of the triggering fibers with respect to the individual micro-channels) or where the light induced by the passing electron did not produce any measured photoelectron. In the present analysis, the pedestal peak is not fitted. Nevertheless, one can see that the pedestal peak is narrow and well separated from the first photoelecton peak, showing a reasonably low noise of the read-out system and a sufficient signal gain. If one excludes the pedestal from the fit, Eq. 2.4 can be written as

$$F(x) = P_{det} \otimes G_{det} = P(N, \bar{N}_{pe}) \otimes G(x, N, \sigma, \cdot\sqrt{N}) \tag{5.2}$$

where:

- N is the number of events,
- $\bar{N}_{pe}$ is the average number of photoelectrons per event, and
- σ is the standard deviation of the response of the readout electronics to single photoelectrons.

The fit leads to yields of about 0.74 photoelectrons for the channel most illuminated by the electrons. The outer channels give the lowest yield while the inner channels exhibit the highest yield. Its response is shown in Fig. 5.16 together with the fitted function.

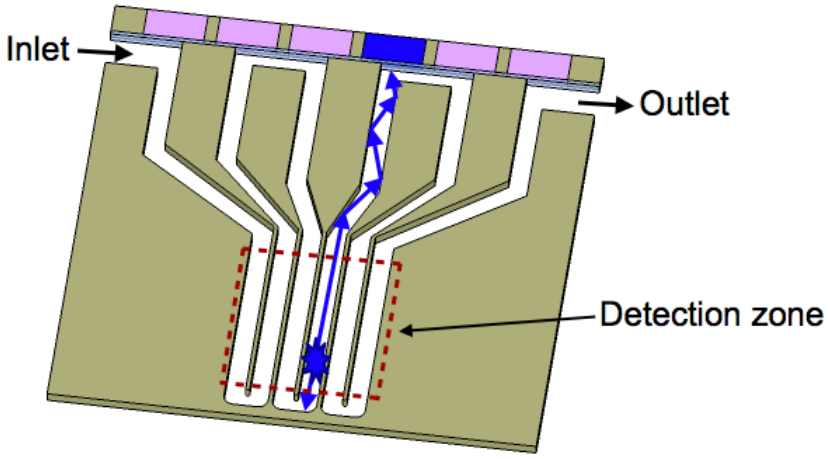

Figure 5.15: 3D schematic representation, not to scale, of the principle of operation of the fabricated prototype detector. A single microfluidic channel defines an array of optically separated waveguides. When a particle interacts with the liquid scintillator in one of the branches the scintillation light is guided towards the corresponding photodetector.The layout of the prototype detector shown here has a reduced detection zone (dotted contour) to cope with the pitch of the photodetector available in the experimental test bench.

The resulting average number of photoelectrons is well in agreement with the performance estimated following the procedure described in Section 2.4.1. Assuming that light is propagated in the waveguides by attenuated total internal reflection[147] (ATIR), the expected photoelectric yield can be expressed from Eq. 2.3 with an additional term to take into account the angles in the channels for the widening of the pitch[158]. It can thus be re-written as

$$\bar{N}_{pe} = N_{scint} \cdot \varepsilon_{coll} \cdot \varepsilon_{refl} \cdot \varepsilon_{att} \cdot \varepsilon_{ang} \cdot \varepsilon_{in} \cdot \varepsilon_{Q_{eff}} \tag{5.3}$$

where:

- N_{scint} is the number of scintillation photons produced isotropically in the microchannel by an impinging particle,
- ε_{coll} is the collection efficiency of a rectangular metal-coated microchannel,
- ε_{refl} is the gain due to the reflective end of the channel opposite to the photodetector,
- ε_{att} is the transport efficiency due to optical absorption in the liquid scintillator,
- ε_{ang} is the efficicency due to the sharp angles in the microchannel,

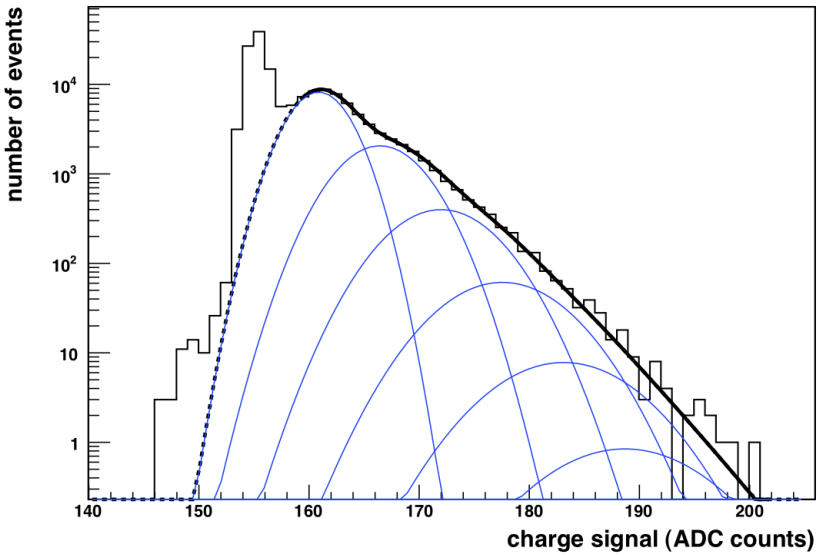

Figure 5.16: Photoelectron spectrum obtained by irradiating a 50 μm $\times$ 200 μm microchannel with MIPs. The average number of photoelectrons is 0.74. The Gaussian curves represent the contributions from 1 to 6 photoelectrons and the global convolution fits the signal.

- ε_{in} is the transmission efficiency at the interface between the microchannel and the photodetctor, and
- $\varepsilon_{Q_{eff}}$ is the quantum efficiency of the PMT.

A MIP traversing a 200 μm deep channel filled with the liquid scintillator EJ-305 produces a number N_{scint} of photons of the order of 420 according to the technical data provided by Eljen Technology. The efficiencies ε_{coll} and ε_{refl} are estimated to be of the order of 0.03 and 1.4 respectively by running Monte Carlo simulations (see Appendix D). The attenuation length of the liquid scintillator EJ-305 is reported by Eljen Technology to be of the order of 3 m. One can safely assume that there is virtually no attenuation along the 10 mm long channels, hence the transmission efficiency ε_{att} is assumed to be 0.99. The transport efficiency ε_{ang} is quite affected by the sharp angles in the channels is derived from the transmission values of optical waveguides with an angular misalignment[159]. The two angles of $\pm 15°$ of the central channels are estimated to induce an efficiency ε_{ang} of approximately 0.6. The outer channels have bigger angles of $\pm 37°$ and $\pm 51°$ which lead to much lower efficiencies of the order of 0.2 and 0.05 respectively, which is confirmed by the observation of a lower photoelectron yield corresponding to passing electrons. The transmission efficiency ε_{in} at the interface between the microchannels and the MAPMT can be roughly expected to be about 0.7

with a thin layer of optical gel. Around 425 nm, the wavelength of maximum emission of the liquid scintillator, the quantum efficiency of the photomultiplier tube $\varepsilon_{Q_{eff}}$ is estimated to be about 0.14 (see Section 4.2.2). The equation leads to a photoelectric yield $\bar{N}_{pe}$ of about 1 photoelectron per MIP for the central channels and to very low light yields of about 0.3 and 0.1 for the other ones.

From the above calculation, it is clear that the low light levels measured with these devices are mainly due to losses in the microchannels at the level of the sharp angles described by the term ε_{ang} in Eq. 5.3. An important fraction of the scintillation photons are lost before reaching the photodetector.

In order to improve the performance of the microfluidic scintillation detectors, a second generation of devices has been fabricated with an enhanced design in terms of light guiding properties. The sharp angles along the channels (see Fig. 5.17a) are replaced by smooth curves (see Fig. 5.17b) to minimize the photons lost due to the pitch enlargement necessary for the MAPMT read-out. The outer dimensions of the new chip remain the same, namely 15 × 20 mm. The detection area is identical, 50 μm wide channels are separated by 10 μm walls over a total length of 10 mm. The pitch enlargement occurs over the remaining 10 mm. A MATLAB routine was implemented to maximize the radiuses of curvature of all the channels[149].

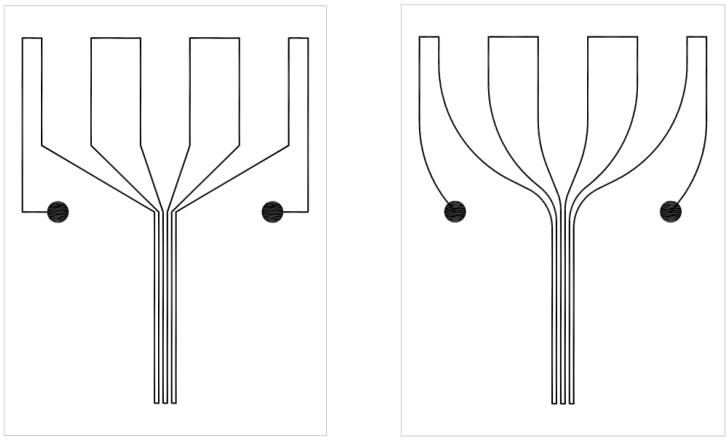

(a) **(b)**

Figure 5.17: Microfluidic channel designs of the prototype detectors. In both cases, the microchannel design defines a detection zone with a pitch of 60 μm on the lower part of the chip and the 50 μm wide channels fan-out to a pitch of 2.3 mm to match the pitch of the pixels of the photodetector. (a) In the first case the widening of the pitch is obtained with sharp angles, whereas (b) in the second case this is obtained with a smooth routing.

Based on the good agreement between the estimated photoelectric yield an the experimental results obtained with the first devices, one can apply the same model to estimate the light yield of the new generation of detectors. However, in this case there should be negligible losses along the curved microchannels and the term ε_{ang} can be excluded from Eq. 5.3. This leads to an expected average number of photoelectrons $\bar{N}_{pe}$ of the order 1.7 for all the channels of the new devices.

The devices are measured in the same experimental set-up as the previous ones, and an average number of about 1.65 photoelectrons per incident MIP is obtained, in excellent agreement with the theoretical expectation. Figure 5.18 shows the typical charge spectrum of one of the outermost scintillating microchannels. The good results obtained with the new prototypes are well in agreement with the extrapolation from the previous results. The significantly higher photoelectric yield measured for the same microchannel cross section leads to a detection efficiency E_{det} of approxiametely 80% for a single scintillating microfluidic channel as derived from Eq. 2.7.

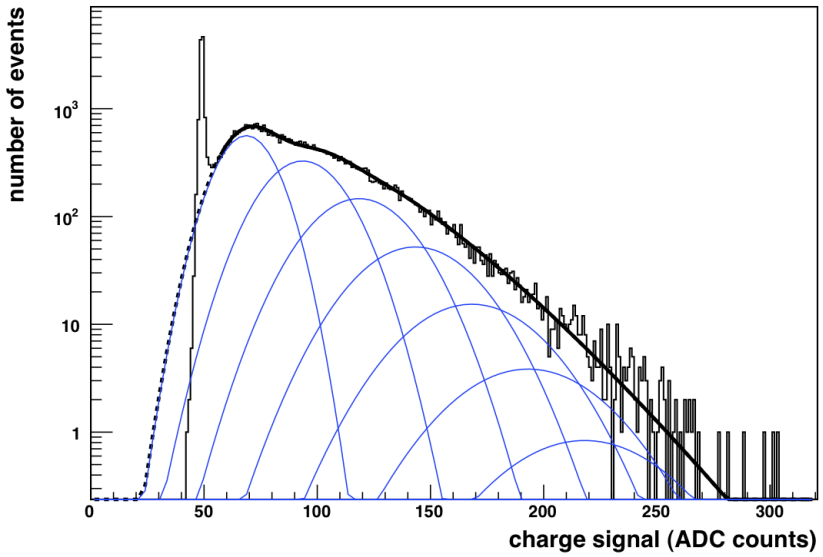

Figure 5.18: Photoelectron spectrum obtained by irradiating a 50 μm $\times$ 200 μm microchannel with MIPs. The average number of photoelectrons is 1.65. The Gaussian curves represent the contributions from 1 to 7 photoelectrons. The global convolution fits the signal very well.

5.6 Conclusions and outlook

The working principle of a novel type of scintillation detector, based on microfluidics, has been demonstrated experimentally. A standard microfabrication process was op-

timized to fabricate structures with high aspect ratios (up to 1:30) in thick layers, of the order of 200 μm, of the SU-8 negative-tone photoresist. These structures define dense arrays of microfluidic channels that are filled with liquid scintillators and optically coupled to external photodetectors. The photoelectric yield of this assembly was measured to be of the order of 1.65 photoelectrons per MIP traversing the liquid scintillator contained in the 200 μm deep microchannels. This number is in full agreement with theoretical calculations and is comparable to the yield of small diameter scintillating fibres.

Microfluidics offer the possibility to control the circulation of liquid scintillators in a relatively simple manner. One can have a continuous flow in the microchannels during data taking in order for the scintillator's performance not to be altered by radiation damage. It is also possible to circulate and change the scintillator only when the efficiency of the detector reaches a critical threshold. Both techniques allow to increase the radiation resistance of detectors by acting directly on their active medium. Moreover, one can change the type of scintillator in the channels enabling to perform different measurements with the same device without any other intervention than fluidic circulation of liquid scintillators in the microchannels.

The excellent results obtained with the SU-8 microfluidic devices are promising for the development of new scintillation detectors with microfabrication technologies. However the project is still in a very early phase and requires a considerable effort to progress from an experimental device to an actual detector. For future developments, it is of foremost importance to match the pixels of the photodetectors to the size of the microchannels. Figure 5.19 shows the sketch of a single plane of microfluidic waveguides with a constant pitch between the detection zone and the photodetector. Arrays of avalanche photodiodes[160] or silicon photomultipliers[50] (SiPM) represent attractive alternatives to MAPMTs. Ongoing developments of high resolution scintillating fibre trackers read-out by SiPMs give encouraging results to work with such detectors[160;51]. Besides, one can also envisage the integration of photodetectors into the substrate of the microfluidic detector, especially for the development of miniaturized particle detectors.

The ease of fabrication of microfluidic devices and the versatility of the geometries that can be implemented to microchannels offer a wide variety of potential configurations for new scintillation detectors. They can be designed and processed to meet the requirements of a wide range of applications such as high-energy physics detectors, X-ray imaging, positron emission tomography, dosimetry, pharmacological studies, and non-

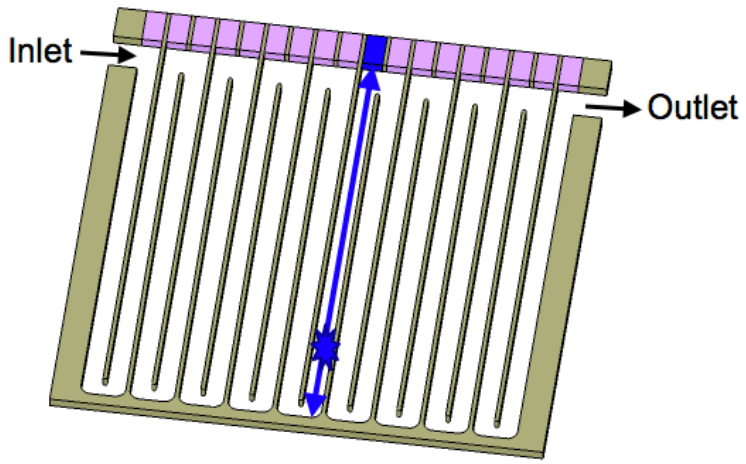

Figure 5.19: 3D schematic representation, not to scale, of the principle of operation of the microfluidic scintillation detector. A single microfluidic channel defines an array of optically separated waveguides. When a particle interacts with the liquid scintillator in one of the branches the scintillation light is guided towards the corresponding photodetector.

destructive material analysis. High spatial resolution miniaturized detectors as well as large area detectors can easily be fabricated with standard microfabrication techniques.

The high fill factors that can be achieved with scintillating microchannels, the possibility to measure very close to the edge of the microfabricated devices, and the increased radiation hardness obtained by circulating and renewing the liquid scintillator make this novel type detector particularly interesting for applications such as calorimetry, tracking, and beam monitoring in the field of high energy physics. Calorimetric detectors can be fabricated by coating the resins to be structured on the surface of heavy materials acting as absorbers. It could also be envisaged to etch the scintillating microchannels directly in the absorber. Low material budget tracking devices and hodoscopes can be fabricated with embedded channels in SU-8[161] in order to meet the very aggressive X_0 requirements of applications such as high energy physics experiments and hadrontherapy online dosimetry. Special formulations of the radiation hard SU-8 photosensitive epoxy allow to fabricate thin active layers with embedded microfluidic scintillating channels (see Appendix E). The compact design and the low material budget of these microfabricated scintillation detectors combined with small pitch arrays of photodetectors open the way to numerous applications where "macro detectors" cannot be used like *in situ* dosimetry and *online* beam profiling in the field of hadrontherapy.

Chapter 6

Conclusions and outlook

This last chapter summarizes the main achievements of this thesis. The two types of scintillation detectors studied are outlined and prospects for both technologies are presented.

In the context of this thesis, two types of scintillation detectors have been developed and studied. The first development aimed at fabricating and characterizing prototype tracking detectors based on the well established plastic scintillating fibres technology. The second research topic consisted in demonstrating the principle of operation of a novel type of scintillation detector based on microfluidics.

The scintillating fibre trackers have been studied in the context of the ATLAS experiment. The ATLAS collaboration will determine the absolute luminosity of the CERN LHC at Interaction Point 1 (IP1) by measuring the trajectory of protons elastically scattered at very small angles (μrad). A scintillating fibre tracker system called ALFA (Absolute Luminosity For ATLAS) is proposed for this measurement. Detector modules will be placed above and below the LHC beam axis in roman pot units at a distance of 240 m on each side of the ATLAS interaction point IP1. They will allow the detectors to approach the beam axis at distances of the order of a millimetre. Two overlap detectors, also based on the scintillating fibre technology, will measure the precise relative position of the two detector modules. Results obtained during beam tests at DESY and at CERN validate the detectors design and demonstrate the achievable resolution.

The main results obtained in this framework can be summarized as follows.

- Experimental results validated the choice of the Kuraray SCSF-78 0.5 mm square fibre for the ALFA tracking detectors. This fibre gives an average photoelectric yield of about 4 photoelectrons in combination with the photomultiplier MAPMT R7600-00-M64 by Hamamatsu. A photoelectric yield of 4 promises an excellent single fibre detection efficiency of the order of 95% leading to a tracking efficiency of the detector superior to 99%. Their efficiency starts decreasing for an accumulated dose greater than 3 kGy which makes them sufficiently radiation resistant for luminosity measurements during dedicated runs.

- The validation of the design of the tracking detectors consisting of 10 staggered planes with 2×64 fibres each. This configuration guarantees a spatial resolution of the prototype trackers of about 36 μm with 6 GeV electrons and 23 μm with 230 GeV protons, in agreement with the 30 μm required. No significant dead space at the edge of the detector was identified.

- The alignment method between two detector modules with so-called overlap detectors was demonstrated. Prototype overlap detectors were tested for the first time in a test beam at CERN and it was shown that the required precision could

be achieved. The vertical relative alignment could be controlled to a precision better than 15 μm.

- A procedure to bend plastic scintillating fibres to very small radiuses to cope with the requirements of the overlap detectors was proposed and successfully implemented to hundreds of fibres for the fabrication of these detectors.

The good results obtained with small-scale prototype detectors lead to the production of the eight detector modules required for the ALFA system. The fabrication of these detectors was very challenging. In particular due to the required spatial resolution implying an extremely precise and regular placement of a large number of small scintillating fibres on thin support plates. Great effort was thus required to successfully move from the construction of small-scale prototype devices to the production of all the detector modules. They are now installed in the LHC tunnel, ready to take data.

In view of the great challenges related to the manufacturing procedure of very precise scintillating fibres detectors, it seemed quite difficult to scale to a larger production. We decided to investigate the possibility of developing an alternative detector with similar performance but with a simplified manufacturing process, exploiting novel microfluidic technologies. The second part of the thesis was thus dedicated to proving the working principle of a liquid scintillation detector based on microfluidics. The approach followed was to benefit from the simplicity with which arrays of optical waveguides can be structured with standard microfabrication techniques in order to manufacture detectors. It is possible with photolithograpy to define regular patterns, with feature size of the order of the micrometre, and to reproduce them on a large number of samples. This naturally leads to detectors with an intrinsic high spatial resolution defined by the precision of the photolithography. It has the great advantage of guaranteeing a constant pitch over the whole detector surface and identical features from one detector to another. These techniques can be applied to the fabrication of miniaturized detectors as well as large sensing areas.

Among the many microfabrication techniques envisaged to manufacture prototype detectors, the SU-8 negative-tone photoresist was used as structural element.

The main results obtained with the microfluidic scintillation detectors are the following:

- The parameters of a standard SU-8 process have been optimized to construct thin detection layers (200 μm) with 50 μm wide hollow waveguides separated by 10 μm walls. By filling them with a liquid scintillator, detectors with an intrinsic spatial resolution of the order of 17.3 μm ($= 60\ \mu\text{m}\ /\sqrt{12}$) are obtained.

- The photolelectric yield of these detectors was measured to be about 1.65 photoelectrons per particle traversing the 200 μm deep channels when read-out by an MAPMT.

The excellent results obtained with the SU-8 microfluidic devices are promising for the development of new scintillation detectors with microfabrication technologies. They can be designed and processed to meet the requirements of a wide range of applications such as high-energy physics detectors, X-ray imaging, positron emission tomography, dosimetry, pharmacological studies, and non-destructive material analysis. It is possible to adapt the fabrication process to a wide range of detector geometries and dimensions to obtain state-of-the art spatial resolution and fill-factors of 100% with low material budget.

Bibliography

[1] W. Crookes. "Certain properties of the emanations of radium." *Chem. News*, **87**(241), 1903. 3

[2] H. Geiger and E. Marsden. "On a diffuse reflection of the α-particles." *Roy. Soc. Proc.*, **82**(557), 495–500, 1909. 3

[3] E. Rutherford. "The Scattering of α and β Particles by Matter and the Structure of the Atom." *Philos. Mag.*, **21**, 669–688, 1911. 3

[4] K. Nakamura *et al.* (Particle Data Group). "Review of Particle Physics." *J. Phys. G: Nucl. Part. Phys.*, **37**(075021), 2010. 10, 13, 16, 17, 21

[5] C. Zorn, S. Majewski, and R. Wojcik. "Preliminary study of radiation damage in liquid scintillators." *IEEE Trans. Nucl. Sci.*, **37**(2), 487–491, 1993. 12

[6] D. Oliver and G. Knoll. "Anisotropy of scintillation response of anthracene to neutron generated recoil protons and carbon ions." *IEEE Trans. Nucl. Sci.*, **15**(3), 122–126, 1968. 14

[7] G. Bendiscioli *et al.* "Study of a thin scintillator detector." *Nucl. Instr. and Meth.*, **206**, 471–476, 1983. 14

[8] M. Muga, D. Burnsed, and W. Steeger. "Recipe for making a thin film detector." *Nucl. Instr. and Meth.*, **104**, 605–610, 1972. 14

[9] N. Ajitanand and K. Iyengar. "On the technique of preparation of high quality thin film scintillators." *Nucl. Instr. and Meth.*, **133**, 71–74, 1976. 14

[10] H. Geissel *et al.* "Energy loss and straggling of alpha particles in thin homogeneous NE-111 scintillator foils." *Nucl. Instr. and Meth.*, **144**, 465–468, 1977. 14

[11] C. Manduchi, M. Russo-Manduchi, and G. Segato. "Repsonse of ultra-thin scingtillator foils to fission fragments." *Nucl. Instr. and Meth. A*, **243**, 453–458, 1986. 14

[12] E. Norbeck, T. Dubbs, and L. Sobotka. "Spin coating thin films of plastic scintillator." *Nucl. Instr. and Meth. A*, **262**, 546–547, 1987. 14

[13] L. Weathers and M. Tsang. "Fabrication of thin scintillator foils." *Nucl. Instr. and Meth. A*, **381**, 567–568, 1996. 14

[14] F. Brooks, W. Cilliers, and M. Allie. "The response of thin NE102A scintillator films to fission fragments." *Nucl. Instr. and Meth. A*, **240**, 338–342, 1985. 14

[15] T. Batsch and M. Moszynski. "Pulse height resolution of thin scintillator films." *Nucl. Instr. and Meth.*, **125**, 231–236, 1975. 14

[16] J. Kohl. "Respons of various thin-film scintillators to low-energy particles." *Nucl. Instr. and Meth.*, **125**, 413–417, 1975. 14

[17] K. Ettling and W. vonWitsch. "A thin-film scintillator detector for light ions in low-energy nuclear physics." *Nucl. Instr. and Meth.*, **148**, 299–301, 1978. 14

[18] G. Bendiscioli *et al.* "Performance of a thin scintillator detector." *Nucl. Instr. and Meth. A*, **227**, 478–482, 1984. 14

[19] A. Galindo-Uribarri *et al.* "A thin plastic scintillator time-zero detector and flux monitor." *Nucl. Instr. and Meth. A*, **301**, 457–464, 1991. 14

[20] Z. Youxiong *et al.* "The use of the thin plastic scintillator foocused by using concave ellipsoidal mirror in heavy ion TOF." *Nucl. Instr. and Meth. A*, **355**, 464–468, 1995. 14

[21] T. B. amn M Moszynski. "Timing properties of thin scintillator films." *Nucl. Instr. and Meth.*, **123**, 341–352, 1975. 14

[22] Z. Cho and C. Tsai. "Tin and lead loaded plastic scintillators for low energy gamma-ray detection with particular application to high dose rate application." *IEEE Trans. Nucl. Sci.*, **22**(1), 72–80, 1975. 14

[23] C. Ashford *et al.* "High-Z liquid scintillators containing tin." *Nucl. Instr. and Meth. A*, **243**, 131–136, 1986. 14

[24] L. Eriksson *et al.* "Comparative studies on plastic scintillators - Applications to low energy high rate photon detection." *Nucl. Instr. and Meth.*, **122**, 373–376, 1974. 14

[25] V.D. Ryzhikov *et al.* "Use of gadolinium orthosilicate scintillators in x-ray radiometers." *Opt. Eng.*, **44**(1), 016403–1:6, 2005. 15

[26] M. Moszynski *et al.* "Properties of CsF, a fast inorganic scintillator in energy and time spectroscopy." *Nucl. Instr. and Meth.*, **179**, 271–276, 1981. 15

[27] F. Nessi-Tedaldi *et al.* "Studies of lead tungstate crystals exposed to large proton and pion fluences." In "Proceedings of the 10^{th} International Conference on Advanced Technology and Particle Physics (ICATPP), Como, Italy, October 9-12," 2007. 15, 22

[28] L. Bollinger, G. Thomas, and R. Ginther. "Neutron detection with glass scintillators." *Nucl. Instr. and Meth.*, **17**, 97–116, 1962. 15

[29] R. Zhu. "Radiation damage in scintillating crystals." *Nucl. Instr. and Meth. A*, **413**, 297–311, 1998. 16

[30] K. Wick, D. Paul, P. Schröder, V. Stieber, and B. Bicken. "Recovery and dose rate dependence of radiation damage in scintillators, wavelength shifters and light guides." *Nucl. Instr. and Meth. A*, **61**, 472–486, 1991. 16, 17, 51

[31] K.G. Young *et al.* "Effects of radiation on scintillating fiber performance." *IEEE Trans. Nucl. Sci.*, **40**(4), 461–465, 1993. 16, 51, 52

[32] M. Ishii and M. Kobayashi. "Single crystals for radiation detectors." *Prog. Crystal Growth and Charact.*, **23**, 245–311, 1991. 16

[33] A. Bross and A. Pla-Dalmau. "Radiation damage of plastic scintillators." *IEEE Trans. Nucl. Sci.*, **39**(5), 1199–1204, 1992. 16, 51

[34] C. Zorn. "A pedestrian's guide to radiation damage in plastic scintillators." *Nucl. Phys. B (Proc. Suppl.)*, **32**, 377–383, 1993. 16

[35] E. Biagtan *et al.* "Effects of gamma radiation dose rate on the light output of commercial polymer scintillators." *Nucl. Instr. and Meth. B*, **93**, 296–301, 1994. 16

[36] V. Vasil'chanko *et al.* "New results on radiation damage studies of plastic scintillators." *Nucl. Instr. and Meth. A*, **369**, 55–61, 1996. 16

[37] E. Biagtan *et al.* "Gamma dose and dose rate effects on scintillator light output." *Nucl. Instr. and Meth. B*, **108**, 125–128, 1996. 16

[38] A. Murakami, H. Yoshinaka, and M. Goto. "Radiation Hardness of Plastic Scintillating Fiber against Fast Neutron and gamma-ray Irradiation." *IEEE Trans. Nucl. Sci.*, **40**(4), 495–499, 1993. 17, 51

[39] V. Senchishin *et al.* "A new radiation stable plastic scintillator." *Nucl. Instr. and Meth. A*, **364**, 253–257, 1995. 17

[40] A. Cardini *et al.* "Comparison of plastic scintillating fibres and capillaries filled with liquid scintillator." *Nucl. Instr. and Meth. A*, **346**, 163–167, 1994. 17, 21

[41] J. Birks. *Scintillation counters.* Pergamon, 1953. 17

[42] J. Birks. *The Theory and Practice of Scintillation Counting.* Pergamon, 1964. 17, 53

[43] D. Clark. "The intrinsic scintillation efficiency of plastic scintillators for ^{60}Co gamma excitation." *Nucl. Instr. and Meth.*, **117**, 295–303, 1974. 17

[44] E.H. Bellamy *et al.* "Absolute calibration and monitoring of a spectrometric channel using a photomultiplier." *Nucl. Instr. and Meth. A*, **339**, 468–476, 1994. 18

[45] S. Suzuki *et al.* "New position sensitive photomultiplier tubes for high energy physics and nuclear medical applications." *IEEE Trans. Nucl. Sci.*, **35**(1), 382–386, 1988. 20

[46] V. Agoristas *et al.* "Fast readout of scintillating fiber arrays using position-sensitive photomultipliers." *Nucl. Instr. and Meth. A*, **357**, 78–86, 1995. 20

[47] F. Ferroni and G. Martellotti. "Capillary fiber microvertex detectors." *Nucl. Instr. and Meth. A*, **368**, 224–228, 1995. 20, 21

[48] N. Nonaka *et al.* "An APD linear array for scintillating fiber tracker read-out." *Nucl. Instr. and Meth. A*, **383**, 81–88, 1996. 20

[49] M. Kapusta *et al.* "Hamamatsu S8550 APD arrays for high-resolution scintillator matrices readout." *Nucl. Instr. and Meth. A*, **504**, 139–142, 2003. 20

[50] B. Dolgoshein *et al.* "Status report on silicon photomultiplier development and its applications." *Nucl. Instr. and Meth. A*, **563**, 368–376, 2006. 20, 105

[51] G. Roper Yearwood *et al.* "The development of a high-resolution scintillating fiber tracker with silicon photomultiplier readout." *Nucl. Instr. and Meth. A*, **628**, 403–406, 2011. 20, 105

[52] A. Rochas. *Single Photon Avalanche Diodes in CMOS Technology.* Ph.D. thesis, Ecole Polytechnique Fédérale de Lausanne (EPFL), 2003. 20

[53] S. Golovkin *et al.* "Development of tracking detectors based on capillaries with liquid scintillator." *Nucl. Instr. and Meth. A*, **305**, 385–390, 1991. 21, 84

[54] M. Adinolfi *et al.* "Progress on high-resolution tracking with scintillating fibres: a new detector based on capillaries filled with liquid scintillator." *Nucl. Instr. and Meth. A*, **315**, 177–181, 1992. 21, 84

[55] P. Annis *et al.* "Experimental results from a large volume active target made of glass capillaries and liquid scintillator." *Nucl. Instr. and Meth. A*, **367**, 377–383, 1995. 21

[56] A. Cardini *et al.* "Study of capillary tracking detectors with position-sensitive photomultiplier readout." *Nucl. Instr. and Meth. A*, **361**, 129–137, 1995. 21

[57] S. Golovkin *et al.* "Radiation damage studies on new liquid scintillators and liquid-core scintillating fibers." *Nucl. Instr. and Meth. A*, **362**, 283–291, 1995. 21

[58] P. Annis *et al.* "A new vertex detector made of glass capillaries." *Nucl. Instr. and Meth. A*, **386**, 72–80, 1997. 21

[59] S Buontempo *et al.* "Development of large-volume, high-resolution tracking detectors based on capillaries filled with liquid scintillator." *Nucl. Instr. and Meth. A*, **360**, 7–12, 1995. 21, 84

[60] H. Shao, D. Miller, and C. Pearsall. "Scintillating Fiber Optics and Their Application in Radiographic Systems." *IEEE Trans. Nucl. Sci.*, **38**(2), 845–857, 1991. 22

[61] P. Ottonello, G. Rottigni, G. Zanella, and R. Zannoni. "An X-ray area detector with scintillating glass fiber optics." *Nucl. Instr. and Meth. A*, **323**, 485–488, 1992. 22

[62] G. Gennaro, M. Malvestio, G. Zanella, and R. Zannoni. "Scintillating optical fibers in mammography." *Nucl. Instr. and Meth. A*, **382**, 567–572, 1996. 22

[63] C. D'Ambrosio, H. Leutz, T. Shimizu, and O. Shinji. "Imaging performances obtained with fused bundles of scintillating fibres." *Nucl. Instr. and Meth. A*, **325**, 161–167, 1993. 22

[64] P. Reeder *et al.* "Imaging neutron beams with scintillating fiber faceplates." *Nucl. Instr. and Meth. A*, **402**, 155, 1998. 22

[65] L. Evans and P. Bryant. "LHC Machine." *JINST*, **3**(S08001), 2008. 27

[66] The ATLAS Collaboration, G. Aad, **A. Mapelli**, *et al.* "The ATLAS experiment at the CERN Large Hadron Collider." *JINST*, **3**(S08003), 2008. 27, 28, 37

[67] The ATLAS Collaboration. "ATLAS Forward Detectors for Luminosity Measurement and Monitoring." Letter of Intent CERN/LHCC/2004-010, CERN, 2004. 27, 29, 31

[68] The ATLAS Collaboration. "ATLAS Forward Detectors for Measurement of Elastic Scattering and Luminosiy." Technical Design Report CERN/LHCC/2008-004, CERN, 2008. 27, 29, 30, 31, 34

[69] C. Augier. "The UA4/2 experiment at the CERN $S\bar{p}pS$ collider." *Nucl. Instr. and Meth. A*, **389**, 409, 1997. 27, 134, 135

[70] P. van Esch. "The H1 forward proton spectrometer at HERA." *Nucl. Instr. and Meth. A*, **446**, 409, 2000. 27

[71] "The LEP project." Report CERN-PU-ED-80-01, CERN. 27

[72] The CMS Collaboration. "The CMS Experiment at the CERN LHC." *JINST*, **3**(S08004), 2008. 27, 31

[73] The LHCb Collaboration. "The LHCb Detector at the LHC." *JINST*, **3**(S08005), 2008. 27

[74] The TOTEM Collaboration. "The TOTEM experiment at the CERN Large Hadron Collider." *JINST*, **3**(S08007), 2008. 27, 31, 37

[75] The ALICE Collaboration. "The ALICE experiment at the CERN LHC." *JINST*, **3**(S08002), 2008. 27

[76] The ATLAS Collaboration. "Zero Degree Calorimeters for ATLAS." Letter of Intent CERN/LHCC/2007-001, CERN, 2007. 29, 30

[77] M.G. Albrow *et al.* "FP420: An R&D Proposal to Investigate the Feasibility of Installing Proton Tagging Detectors in the 420 m Region of the LHC." Letter of Intent CERN-LHCC-2005-025, CERN, 2005. 30, 42

[78] C. Royon. "High mass diffractive physics at the lhc." In "Proc. of DIS2007," 2007. 30

[79] The ATLAS Collaboration. "ATLAS High-Level Trigger, Data Acquisition and Controls." Technical Design Report CERN/LHCC/2003-022, CERN, 2003. 30, 41

[80] H. Stenzel. "Luminosity calibration from elastic scattering." ATLAS Technical Note ATL-LUM-PUB-2007-001, CERN, http://cdsweb.cern.ch/record/1007180, 2007. 31

[81] D. Bernard *et al.* "The real part of the antiproton-proton elastic scattering amplitude at the centre of mass energy of 546 GeV." *Phys. Lett. B*, **198**(4), 583–589, 1987. 32, 37

[82] C. Joram, H. Stenzel, and A. Braem. "Basic considerations on the Overlap Detectors of the ATLAS ALFA detectors." Tech. Rep. ATL-LUM-PUB-2007-002, CERN, 2006. 34, 38, 39

[83] K. Dahlerup-Petersen. "Field measurements." Tech. rep., CERN, 2006. 34

[84] U. Amaldi *et al.* "The real part of the forward proton proton scattering amplitude measured at the CERN intersecting storage ring." *Phys. Lett. B*, **66**(4), 390–394, 1977. 36, 134

[85] C. Augier. *Mesure de la partie réelle de l'amplitude de la diffusion élastique proton-antiproton vers l'avant, à l'énergie dans le réferentiel du centre de masse 541 GeV*. Ph.D. thesis, Université de Paris Sud: Orsay, 1993. 37

[86] R. Battiston *et al.* "The "Roman Pot" spectrometer and the vertex detector of experiment UA4 at the CERN SPS collider." *Nucl. Instr. and Meth. A*, **238**, 35–44, 1985. 37

[87] P. Abe *et al.* "Measurement of small angle antiproton-proton elastic scattering at $\sqrt{s} = 546$ and 1800 GeV." *Phys. Rev. D*, **50**(4), 5518–5534, 1994. 37

[88] A. Brandt *et al.* "A forward proton detector at D0." Tech. rep., Fermilab, 1997. 37

[89] V. Abazov *et al.* "The upgraded D0 detector." *Nucl. Instr. and Meth. A*, **565**, 463–537, 2006. 37

[90] S. Bultmann *et al.* "The PP2PP experiment at RHIC: silicon detectors installed in Roman Pots for forward proton detection close to the beam." *Nucl. Instr. and Meth. A*, **535**, 415–420, 2004. 37

[91] M. Derrick *et al.* "The ZEUS Leading Proton Spectrometer and its use in the measurement of elastic œÅ0 photoproduction at HERA." *Z. Phys. C*, **73**, 253–268, 1997. 37

[92] P. van Esch *et al.* "The H1 forward proton spectrometer at HERA." *Nucl. Instr. and Meth. A*, **446**, 409–425, 2000. 37

[93] K. Lang *et al.* "A comprehensive characterization of Hamamatsu 16- and 64-anode PMTs." *Nucl. Instr. and Meth. A*, **461**, 571–573, 2001. 40

[94] E. Albrecht *et al.* "Performance of a cluster of multi-anode photomultipliers equipped with lenses for use in a prototype RICH detector." *Nucl. Instr. and Meth. A*, **488**, 110–130, 2002. 40

[95] K. Lang *et al.* "Characterization of 1600 Hamamatsu 16-anode photomultipliers for the MINOS Far detector." *Nucl. Instr. and Meth. A*, **545**, 852–871, 2005. 40

[96] N. Tagg *et al.* "Performance of Hamamatsu 64-anode photomultipliers for use with wavelength—shifting optical fibres." *Nucl. Instr. and Meth. A*, **539**, 668–678, 2005. 40

[97] E. Baussan *et al.* "The neutrino oscillation OPERA experiment Target Tracker." *Nucl. Instr. and Meth. A*, **581**, 465–468, 2007. 40

[98] P. Abbon *et al.* "The characterisation of the multianode photomultiplier tubes for the RICH-1 upgrade project at COMPASS." *Nucl. Instr. and Meth. A*, **595**, 177–179, 2008. 40

[99] M. Gilliot *et al.* "Scintillating anticoincidence detection elements design and tests with muons and protons." *Nucl. Instr. and Meth. A*, **621**, 258–266, 2010. 40

[100] K. Rielage *et al.* "Characterization of a multianode photomultiplier tube for use with scintillating fibers." *Nucl. Instr. and Meth. A*, **463**, 149–160, 2001. 40

[101] M. Buénerd. "The RICH counter of the AMS experiment." *Nucl. Instr. and Meth. A*, **502**, 158–162, 2003. 40

[102] G. Barbarino *et al.* "The Time-of-Flight system for the PAMELA experiment in space." *Nucl. Instr. and Meth. A*, **584**, 319–326, 2008. 40

[103] **A. Mapelli**, H. Dam, M. Glaser, and C. Joram. "Characterization of irradiated plastic scintillating fibres for the ATLAS Luminosity tracker ALFA." ATLAS Technical Note ATL-COM-LUM-2007-009, CERN, 2007. 40, 45, 51

[104] P Barrillon *et al.* "PMF: the front end electronic of the ALFA detector." *Nucl. Instr. and Meth. A*, **623**(1), 463–465, 2010. 41

[105] P. Barrillon *et al.* "MAROC: Multi-Anode Readout Chip for MAPMTs." In "IEEE Nuclear Science Symposium Record," N23-2. 2006. 41, 49

[106] W. Iwanski. "FPGA based Readout Logic of the Front-end Electronics of the ATLAS Absolute Luminosity Monitor." In "Proceedings of TWEPP07," 2007. 41

[107] A. Pilkington. "The ATLAS forward physics program." ATLAS Technical Note ATL-PHYS-CONF-2008-020, CERN, 2008. 42

[108] **A. Mapelli**, A. Braem, C. David, A. Folley, C. J. L. Kottelat, M. van Stenis, H. Stenzel, and M. Szauter. "Design, Construction and Metrology of the Overlap Detectors for the ALFA system." ATLAS Technical Note ATL-COM-LUM-2006-008, CERN, 2006. 45, 57, 69

[109] S Ask, **A. Mapelli**, *et al.* "Luminosity measurement at ATLAS - Development, construction and test of scintillating fibre prototype detectors." *Nucl. Instr. and Meth. A*, **568**, 588–600, 2006. 45, 47, 65

[110] F. Anghinolfi, **A. Mapelli** *et al.* "Hadron beam test of a scintillating fibre tracker system for elastic scattering and luminosity measurement in ATLAS." *JINST*, **2**(P07004), 2007. 45, 59, 65, 69, 72

[111] A. Braem, **A. Mapelli** *et al.* "Trigger counter studies for the alfa detector." ATLAS Technical Note CERN-ATL-LUM-PUB-2009-001, CERN, 2009. 45, 72

[112] **A. Mapelli**. "Studies and development of a magnetic shield for the ATLAS MAPMTs." ATLAS Technical Note ATL-COM-LUM-2010-007, CERN, 2010. 45, 76

[113] B. Allongue, **A. Mapelli** *et al.* "Test beam 2008: First measurements with an ALFA roman pot prototype." ATLAS Technical Note ATL-LUM-INT-2010-001, CERN, 2010. 45, 74, 77, 79

[114] C. Joram and A. Braem. "Fibre tests for the ALFA detector with a lab set-up using a ^{90}Sr source." Tech. rep., CERN, 2005. 46, 138

[115] A. Braem, A. Folley, J. Gentil, C. Joram, and L. Kottelat. "Characterization studies on scintillating fibres." ATLAS Technical Note ATL-LUM-PUB-2006-004, CERN, 2006. 46, 57

[116] J. Santos, J. Saraiva, Y. Nunes, A. Wemans, A. Maio, and M. Maneira. "Aluminization of scntillating fibers for the luminosity detector of ATLAS." Tech. Rep. ATL-LUM-PUB-2007-005, CERN, 2006. 46

[117] R. Ruchti. "Tracking with scintillating fibers." *Nucl. Phys. B (Proc. Suppl.)*, **44**, 308–319, 1995. 48, 53

[118] R. Ruchti. "The use of scintillating fibers for charged-particle tracking." *Ann. Rev. Nucl. Part. Sci.*, **46**, 281–319, 1996. 48, 53

[119] H. de la Torre Perez. "Characterisation and Monte-Carlo study of the T22 Electron Tests Beam Line at DESY II." Tech. Rep. EUDET-Memo-2007-049, 2007. 48

[120] C. Colledani *et al.* "A submicron precision telescope for beam test purposes." *Nucl. Instr. and Meth. A*, **372**, 379–384, 1996. 48

[121] M. Milite. DESY-THESIS 2001-50, 2001. 48

[122] A. Lucotte *et al.* "A front-end read out chip for the OPERA scintillator tracker." *Nucl. Instr. and Meth. A*, **521**, 378–392, 2004. 48, 65

[123] J. Bisplinghoff *et al.* "A scintillating fibre hodoscope for high rate applictaions." *Nucl. Instr. and Meth. A*, **490**, 101–111, 2002. 51

[124] E.C. Aschenauer *et al.* "Testrun results from prototype fiber detectors for high rate particle tracking." *Nucl. Instr. and Meth. A*, **424**, 459–469, 1999. 51

[125] K. Hara *et al.* "Radiation hardness and mechanical durability of kuraray optical fibers." *Nucl. Instr. and Meth. A*, **411**, 31–40, 1998. 51

[126] B. Bicken *et al.* "Recovery and permanent radiation damage of plastic scintillators at differenet dose rates." *IEEE Trans. Nucl. Sci.*, **38**(2), 188–193, 1991. 51

[127] **A. Mapelli**. "Development of a detector (ALFA) to measure the absolute LHC luminosuty at ATLAS." In "Proceedings of the 10^{th} International Conference on Advanced Technology and Particle Physics (ICATPP), Como, Italy, October 9-12," 2007. 51

[128] M. Glaser *et al.* "New irradiation zones at the CERN-PS." *Nucl. Instr. and Meth. A*, **426**, 72–77, 1999. 52

[129] J. Mercier and E. Marechal. *Chimie des polymères: synthèses, réactions, dégradations*. Presses Polytechniques et Universitaires Romandes, 1996. 52

[130] H.A. Klose *et al.* "On the measurement of degradation and recovery of scintillating plastic fibres." *Nucl. Instr. and Meth. A*, **135**, 555–559, 1998. 52

[131] R. Bock *et al.* "PAW - Towards a Physics Analysis Worstation." *Comp. Phys. Comm.*, **45**(181-190), 1987. 55

[132] C. Wilkes, J. Summers, and C. Daniels, eds. *PVC Handbook*. Hanser Gardner Publications, Inc., 2005. 57

[133] S. Jakobsen and C. Joram. "Light yield stability over time in bent squared scintillating fibers." Tech. Rep. ATL-COM-LUM-2010-XXX, CERN, 2010. 59

[134] **A. Mapelli** and C. Joram. "Estimation of the δ-ray production in the ALFA detector 10_2_6." Tech. Rep. CERN-ATL-COM-LUM-2007-009, CERN, 2007. 64, 69

[135] P. Barrillon, **A. Mapelli**, *et al.* "Test of scintillating fibres prototype detectors using the OPERA front-en read out chip." ATLAS Technical Note ATL-COM-LUM-2006-005, CERN, 2006. 65

[136] V. Vorobel and H. Stenzel. "GEANT4 simulation of the testbeam set-up for the ALFA detector." ATLAS Technical Note CERN-ATL-COM-LUM-2006-006, CERN, 2006. 65

[137] A. Braem, C. Joram, **A. Mapelli**, A. Kocnar, and J. Pospichal. "Metrology results of the ALFA 2006 prototype detectors." ATLAS Technical Note ATL-LUM-PUB-2006-007, CERN, 2006. 65

[138] B. Rossi. *High-Energy Particles*. Prentice-Hall, Inc., 1952. 69

[139] **A. Mapelli** and C. Joram. "ALFA Overlap Detectors Prototype Study from the CERN Testbeam in 2006." ATLAS Technical Note ATL-COM-LUM-2007-003, CERN, 2007. 71

[140] M. Clemens *et al.* "The electromagnetic simulation software package MAFIA 4." In "Computational Electromagnetics and Its Applications, 1999. Proceedings. (ICCEA '99) 1999 International Conference on," pp. 565–568. 1999. 76

[141] B. Allongue *et al.* "Results from the ALFA test beam campaign in 2009." ATLAS Technical Note ATL-LUM-INT-2010-XXX, CERN, 2010. 79

[142] C. Curat. "Liquid scintillator filled capillaries." 83

[143] A Bay *et al.* "A high-resolution tracking hodoscope based on capillary layers filled with liquid scintillator." *Nucl. Instr. and Meth. A*, **457**, 107–116, 2001. 84, 85

[144] A. Artamonov *et al.* "Liquid scintillator calorimetry for the LHC." *Nucl. Instr. and Meth. A*, **360**, 240–244, 1995. 84

[145] J. Konijin *et al.* "RD46 Status Report - High resolution tracking devices based on capillaries filled with liquid scintillator." Status Report CERN-LHCC 97-38, CERN, 1997. 84, 85, 86

[146] R. Guerre, C. Hibert, Y. Burri, P. Flückiger, and P. Renaud. "Fabrication of vertical digital silicon optical micromirrors on suspended electrode for guided-wave optical switching applications." *Sens. Act. A*, **123-124**, 570–583, 2005. 87

[147] R. Guerre. *Guided-wave micro-electro-mechanical systems (MEMS) optical switches for telecommunication applications*. Ph.D. thesis, Ecole Polytechnique Fédérale de Lausanne (EPFL), 2005. 87, 101

[148] M. Key, V. Cindro, and M. Lozano. "On the radiation tolerance of SU-8, a new material for gaseous microstructure radiation detector fabrication." *Rad. Phys. Chem.*, **71**, 1003–1007, 2004. 87

[149] N. VicoTriviño, **A. Mapelli**, and P. Renaud. "Fabrication of high aspct ratio structures in SU-8 for high-spatial resolution microfluidic scintillation detectors.", 2009. EPFL Semester Project Thesis. 88, 103

[150] H. Lorenz, M. Despont, N. Fahrni, N. LaBianca, P. Renaud, and P. Vettiger. "SU-8: a low-cost negative resist for mems." *J. Micromech. Microeng.*, **7**, 121–124, 1997. 88

[151] H. Lorenz *et al.* "High-aspect-ratio, ultrathick, negative-tone near-UV photoresist and its applications for MEMS." *Sens. Act. A*, **64**, 33–39, 1998. 88

[152] S. Metz, S. Jiguet, A. Bertsch, and P. Renaud. "Polyimide and SU-8 microfluidic devices manufactured by heat-depolymerizable sacrificial material technique." *Lab Chip*, **4**, 114–120, 2004. 88

[153] J. Schmitz. "Adding functionality to microchips by wafer post-processing." *Nucl. Instr. and Meth. A*, **576**, 142–149, 2007. 88

[154] J.H. Daniel *et al.* "Fabrication of high aspect-ratio polymer microstructures for large-area electronic portal X-ray imagers." *Sens. Act. A*, **140**, 185–193, 2007. 88

[155] **A. Mapelli**, B. Gorini, M. Haguenauer, S. Jiguet, G. Lehmann Miotto, W. Vandelli, N. VicoTriviño, and P. Renaud. "Scintillation particle detection based on microfluidics." *Sens. Act. A*, **162**, 272–275, 2010. 88, 93

[156] G. Genolet. *New photoplastic fabrication techniques and devices based on high aspect ratio photoresist.* Ph.D. thesis, Ecole Polytechnique Fédérale de Lausanne (EPFL), 2001. 90

[157] S. Jiguet. *Microfabrication d'objets composites fonctionnels en 3D à haut facteur de forme, par procédés UV-LIGA et microstéréolithographie.* Ph.D. thesis, Ecole Polytechnique Fédérale de Lausanne (EPFL), 2004. 94

[158] **A. Mapelli**, B. Gorini, M. Haguenauer, S. Jiguet, and P. Renaud. "Development and studies of a novel microfabricated radiation hard scintillation particle detector with high spatial resolution." *Nucl. Phys. B (Proc. Suppl.)*, **197**, 43–47, 2009. 101

[159] J. Sutherland *et al.* "Alignment Tolerance Measurements and Optical Coupling Modeling for Optoelectronic Array Interface Assemblies." In "45^{th} Elec. Comp. and Tech. Conf.", pp. 577–583. 1995. 102

[160] Q. Ingram *et al.* "Radiation hard avalanche photodiodes for the CMS detector." *Nucl. Instr. and Meth. A*, **537**, 379–382, 2005. 105

[161] **A. Mapelli**, B. Gorini, S. Jiguet, N. V. Triviño, and P. Renaud. *SU-8 processes for microfluidic radiation detctors and integrated optical waveguides*. Nova Publiashers, 2011. 106

[162] W. Herr. "Beam-beam effects in the LHC." *Particle Accelerators*, **50**, 69–81, 1995. 132

[163] S. van der Meer. "Calibration of the effective beam height in the ISR." Tech. Rep. ISR-PO/68-31, CERN, 1968. 133

[164] W. Herr and B. Muratori. "Concept of luminosity." *CAS - CERN Accelerator School: Intermediate Course on Accelerator Physics*, **1**, 361–378, 2003. 135

[165] "http://physics.nist.gov/physrefdata/star/text/estar.html." 138, 139

[166] B. Saleh and M. Teich. *Fundamentals of Photonics*. John Wiley & Sins, Inc., 1991. 159, 160

Nomenclature

Variables and constants

$-dE/dx$	Rate of energy loss, or Stopping power	[MeV·g^{-1}cm^2]
β	Particle velocity expressed in terms of c, v/c	[-]
$\delta\,(\beta\gamma)$	Density effect correction to ionization energy loss	[-]
η	Pseudorapidity	[-]
γ	Lorentz factor $1/\sqrt{1-\beta^2}$	[-]
μ	Magnetic permeability	[H/m]
σ	Cross section	[b]
θ	Forward scattering angle	[rad]
ε_{att}	Optical attenuation efficiency	[%]
ε_{coll}	Collection efficiency	[%]
ε_{det}	Detection efficiency	[%]
ε_{in}	Transmission at scintillator-photodetector interface	[%]
$\varepsilon_{Q_{eff}}$	Photodetector quantum efficiency	[%]
ε_{refl}	Optical gain due to reflections	[%]
A	Mass number	[-]
c	Speed of light in vacuum = 299 792 458	[m·s^{-1}]
E	Incident particle energy γMc^2	[MeV]
e	Electron charge magnitude $\approx 1.602 \times 10^{-19}$	[C]

Nomenclature

E_{CM}	Centre of mass energy	[eV]
f	Frequency	[Hz]
L	Luminosity	[$\mathrm{cm^{-2}s^{-1}}$]
m	Incident particle mass	[MeV]
m_e	Electron mass at rest ≈ 0.510 ($\approx 9.109 \times 10^{-31}$ kg)	[$\mathrm{MeV/c^2}$]
N_A	Avogadro's number $= 6.022 \times 10^{23}$	[$\mathrm{mol^{-1}}$]
N_b	Number of colliding bunches	[-]
N_i	Number of particles per bunch	[-]
p	Particle momentum	[eV]
R	Counting rate	[Hz]
r_e	Classical electron radius $= e^2/4\pi\epsilon_0 m_e c^2 \approx 2.8 \times 10^{-15}$	[m]
T	Kinetic energy	[MeV]
T_g	Glass transition temperature	[°C]
v	Particle velocity	[$\mathrm{m{\cdot}s^{-1}}$]
X_0	Radiation length	[$\mathrm{g{\cdot}cm^{-2}}$]
Z	Atomic number	[-]
z	Incident particle charge	[-]
N_{pe}	Number of photoelectrons	[-]
N_{scint}	Number of scintillation photons	[-]

Abbreviations

^{90}Sr	Strontium-90
ADC	Analog-to-Digital Converter
ALFA	Absolute Luminosity For ATLAS
ALICE	A Large Ion Collider Experiment

APD	Avalanche PhotoDiode
ATLAS	A Toroidal Large ApparatuS
CCD	Charge-Coupled Device
CERN	Conseil Européen pour la Recherche Nucléaire
CMS	Compact Muon Solenoid
DAQ	Data AcQuisition system
DESY	Deutsches Elektronen SYnchrotron
FPGA	Field-Programmable Gate Array
GBL	Gamma-ButyroLactone
GM-APD	Geiger-Mode Avalanche PhotoDiode
HEP	High Energy Physics
IP	Interaction Point
IP1	ATLAS Interaction Point
IP5	CMS Interaction Point
LHC	Large Hadron Collider
LHCb	LHC beauty
LUCID	LUminosity measurement using a Cherenkov Detector
MAPMT	Multi-Anode PhotoMultiplier Tube
MAROC	Multi-Anode Read-Out Chip
MEMS	Micro-Electro-Mechanical Systems
MIP	Minimum Ionizing Particle
NIM	Nuclear Instrumentation Module
OD	Overlap Detector
PAG	Photo-Acid Generator

PC	Personal Computer
PCB	Printed Circuit Board
PDMS	PolyDiMethylSiloxane
PET	Positron Emission Tomography
PGMEA	Propylene Glycol Methyl Ether Acetate
PMF	PhotoMultiplier Front-end
PMMA	PolyMethylMethAcrylate
PMT	PhotoMultiplier Tube
PS	PolyStyrene
PVT	PolyVinylToluene
QDC	Charge-to-Digital Converter
RP	Roman Pot
SiPM	Silicon PhotoMultiplier
SPAD	Single Photon Avalanche Diode
SPECT	Single Photon Emission Computed Tomography
TDAQ	Trigger and Data AcQuisition
TIR	Total Internal Refraction
TOTEM	Total Cross Section Elastic Scattering and Diffraction Dissociation at the LHC
USB	Universal Serial Bus
UV	UltraViolet
VME	Versa Module Eurocard
WLS	WaveLength Shifter
ZDC	Zero Degree Calorimeter

Appendix A

Luminosity of particle accelerators

In particle physics experiments, the most important parameters are the energy available for the production of new effects and the number of useful interactions or events. The event rate is of particular importance when rare events with a small production cross section are studied. To determine the cross section of an event of interest based on the measurement of its rate, one needs to determine precisely the luminosity of the machine producing it.

A.1 Luminosity

The luminosity L of an accelerator characterizes its performance. It is a process-independent parameter that is completely determined by the properties of the colliding beams and it relates the cross section of a given process σ to the corresponding event rate

$$R = L \cdot \sigma \tag{A.1}$$

where the event rate R is equal to dN/dt and N is the number of events of a given process. The rate of events R_{meas} measured by a given detector is proportional to the rate of events R produced

$$R_{meas} = R \cdot A \cdot \varepsilon \tag{A.2}$$

where A is the acceptance of the detector and ε its efficiency .

In a collider the luminosity L of two bunched beams with N_b bunches colliding head-on[162] with a frequency f is

$$L = N_b f N_1 N_2 I_x \left(\rho_1 \left(x\right) \rho_2 \left(x\right)\right) I_y \left(\rho_1 \left(y\right) \rho_2 \left(y\right)\right) \tag{A.3}$$

where $N_{1(2)}$ are the beam intensities in number of particles in the colliding bunches $\rho_{1(2)}(x)$, $\rho_{1(2)}(y)$ are the densities of beam 1(2) in the $x-y$ transverse plane at the interaction point. Assuming there is no correlation between x and y and $I_x \left(\rho_1 \left(x\right) \rho_2 \left(x\right)\right) = \int \rho_1 \left(x\right) \rho_2 \left(x\right) dx$ is the beam overlap integral in the x direction. The same definition applies for the y direction.

The general case where the bunches from the two beams with Gaussian profiles are not identical the luminosity is expressed as

$$L = F \frac{N_b f N_1 N_2}{2\pi \sqrt{\sigma_{1x}^2 + \sigma_{2x}^2} \sqrt{\sigma_{1y}^2 + \sigma_{2y}^2}} \tag{A.4}$$

where, F is a factor which accounts for the non-zero crossing angle, σ_{ix} and σ_{iy} are the horizontal (x) and vertical (y) distributions for beam $i = 1{,}2$. To simplify the expression it is assumed that the bunches have the same shape in the transverse profile, that the profiles are independent of position along the bunch, that the particle distributions are not altered during collisions and that there is no crossing angle.

$$L = \frac{N_b f N_1 N_2}{4\pi \sigma_x \sigma_y} \tag{A.5}$$

where σ_x and σ_y characterize the Gaussian beam profiles in the horizontal (x) and vertical (y) directions.

A.2 Methods of absolute luminosity determination

There are roughly three types of luminosity measurement. The first method relies on the accurate measurement of the rate of a well-known and sizable cross section from machine parameters. In the case of hadronic colliders this gives the worst precision, typically above 10%. The second method relies only on machine parameters and does not require any *a-priori* knowledge of particle cross sections. Precisions better than 5% can be achieved. The third one uses the optical theorem and can reach precisions in the order of 2-3%.

A.2.1 Cross sections of known processes

This method relies on the accurate measurement of the rate of a process with a well known and sizable cross section. The rate of events R_{meas} of a given process whose cross section is well known from previous studies is measured with a detector whose acceptance A and efficiency ε are known for the process of interest. The event rate R can thus be determined with Eq. A.2 and the luminosity L can be calculated with Eq. A.1.

This type of luminosity determination is widely used in e^+e^- colliders such as LEP where a high precision can be reached; e^+ and e^- being elementary objects and the E_{cm} of their collisions is actually E_{cm} of the beams. On the other hand, for hadrons E_{cm} depends on how their internal components interact at every collision. Moreover, strong interaction processes have in general a bigger uncertainty in the cross section as compared to electromagnetic processes. It is thus difficult to find a well-sizable cross section in order to precisely determine the luminosity of a hadron collider such as the LHC.

A.2.2 Beam separation scan

S. van der Meer proposed a method to determine the absolute luminosity from machine parameters which does not require the *a priori* knowledge on particle cross sections[163]. He showed that the luminosity of two colliding beams at ISR* (Intersecting Storage Rings) could be measured by observing the counting rate R in a detector while scanning one of the beams vertically with respect to the other. This method is known as the *van der Meer* (*VdM*) scan[163], *beam separation* scan or *luminosity* scan. In this method, the overlap integral defined in Eq. A.3 can be calculated as

$$I_x\left(\rho_1\left(x\right)\rho_2\left(x\right)\right) = \frac{R_x\left(0\right)}{\int R_x\left(x\right)dx} \tag{A.6}$$

where $R_x\left(x\right)$ is the rate measured by a beam monitor detector when a beam scan is performed in the x direction. The convoluted width of the beams can be defined as

$$\Sigma_x = \frac{1}{\sqrt{2\pi}}\frac{R_x\left(0\right)}{\int R_x\left(x\right)dx} \tag{A.7}$$

* The ISR (Intersecting Storage Rings) was a particle accelerator at CERN operated from 1971 to 1984. It was the world's first hadron collider and ran with maximum center of mass energy of 62 GeV.

Equation A.5 can thus be written as

$$L = \frac{N_b f N_1 N_2}{2\pi \Sigma_x \Sigma_y} \tag{A.8}$$

which is the general formula used to determine luminosity from machine parameters by performing beam separation scans.

Precisions of the order of 3.5% have been achieved by beam separation scans.

A.2.3 Optical theorem

The absolute luminosity can also be determined with the optical theorem by measuring the rate of small-angle elastic scattering processes together with the total interaction rate.

The total elastic and inelastic counting rate is related to the luminosity and the total cross section elastic and inelastic by the expression

$$R_{el} + R_{inel} = L \cdot \sigma_{tot} \tag{A.9}$$

The total cross section is related to the elastic cross section for small values of the momentum transfer t by the optical theorem

$$\frac{d\sigma_{el}}{dt} \mid_{t=0} = \frac{\sigma_{tot}^2}{16\pi} \left(1 + \rho^2\right) = \frac{1}{L} \frac{dR_{el}}{dt} \mid_{t=0} \tag{A.10}$$

Therefore the luminosity can be calculated directly from experimental rates through

$$L = \frac{\left(1 + \rho^2\right)}{16\pi} \frac{\left(R_{el} + R_{inel}\right)^2}{\frac{dR_{el}}{dt} \mid_{t=0}} \tag{A.11}$$

Both counting rates and the differential elastic counting rate at small t have to be measured with high precision. This requires a forward inelastic detector to measure the inelastic rate N_{inel} and the possibility to measure the differential elastic rate $\frac{dR_{el}}{dt}$ down to very small values of t and the elastic rate N_{el}. The latter is typically done with Roman Pot systems[84;69].

A slightly modified version uses the Coulomb scattering amplitude which can be precisely calculated. The elastic scattering amplitude is the superposition of the strong

(f_N) and the Coulomb (f_C) amplitudes. The latter dominates at small values of t. The differential cross section can thus be re-written as

$$\frac{d\sigma_{el}}{dt} \mid_{t=0} = \frac{1}{L}\frac{dR_{el}}{dt} \mid_{t=0} = \pi \mid f_N + f_C \mid^2 \approx \pi \mid \frac{2\alpha_{em}}{-t} + \frac{\sigma_{tot}}{4\pi}(\rho + i)\, e^{B\frac{t}{2}} \mid^2 \qquad \text{(A.12)}$$

where α_{em} is the electromagnetic fine-structure constant, ρ is the ratio of the imaginary and real part of the nuclear scattering amplitude, B the nuclear slope for pp scattering and σ_{tot} is the total cross section. If the differential cross section is measured over a large enough range, the unknown parameters σ_{tot}, ρ, B and L can be determined by a fit[69] (see Fig. A.1). The advantage of this method is that it can be performed measuring only elastic scattering without the need to measure the inelastic rate N_{inel}. It is a good way to measure the luminosity and the total cross section without the need of any inelastic detector.

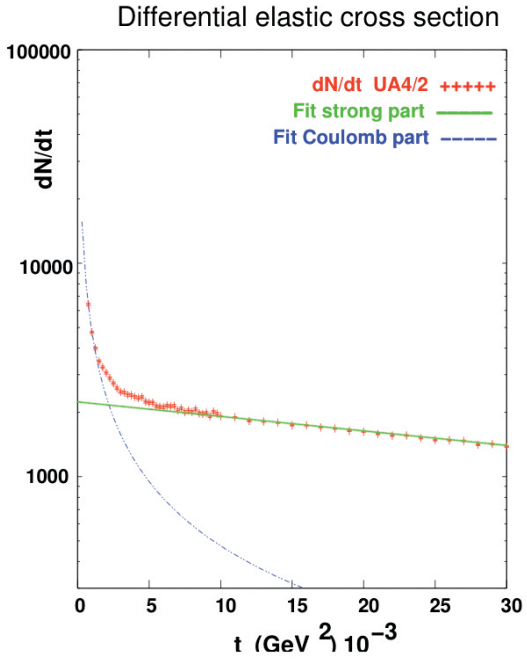

Figure A.1: Principle of luminosity measurement using the optical theorem in proton proton (antiproton) collisions by measuring the differential rate of elastic events[164].

The measurement of the Coulomb amplitude usually requires dedicated experiments with detectors very close to the beam, typically with so-called Roman Pots, and therefore special beam parameters such as reduced intensity and zero crossing angle. Furthermore, in order to measure very small angle scattering, one has to reduce the divergence of the beam. For that purpose special running conditions with high β^* at the collision point are often needed. The precision of such a measurement is as good as a few percent.

A.3 Conclusions

One should distinguish between luminosity measurement and monitoring. The methods described above give an absolute determination of the luminosity. Other methods are used to monitor the luminosity and can be calibrated using the absolute methods. Such relative measurements allow following the luminosity evolution during a collider fill and also between different fills. A possibility is to calibrate them under special, favourable beam conditions (*e.g.* low luminosity and high β^* and use them to determine the luminosity for normal runs (*i.e.* high luminosity).

Appendix B

Electrons from ^{90}Sr source

The most common source of fast electrons is a radioisotope that decays by β^- emission. The decay process of the ^{90}Sr sources used to characterize the scintillators in this thesis can be expressed as follows

$$\begin{aligned} {}^{90}Sr \rightarrow {}^{90}Y + \beta^- \\ \searrow \\ {}^{90}Zr + \beta^- \end{aligned} \tag{B.1}$$

where the decay of ^{90}Sr into ^{90}Y, with a half-life of 28 years, produces electrons with a maximum energy E_{max} of 0.55 MeV and the decay of ^{90}Y into the stable ^{90}Zr, with a half-life of 64 hours, produces electrons with a maximum energy E_{max} of 2.28 MeV. Although the daughter decay of ^{90}Y into ^{90}Zr has a shorter half-life than the parent decay of ^{90}Sr into ^{90}Y it never decays away completely because there are always new daughter ^{90}Y atoms being created by decay of the parent ^{90}Sr. An equilibrium is reached where, for each ^{90}Y atom lost by decay, a new one is gained by decay of ^{90}Sr. Thus the number of disintegrations per second of ^{90}Y is equal to the number of disintegrations per second of ^{90}Sr. This means that the activity of ^{90}Y is equal to the activity of ^{90}Sr. A radioactive source of ^{90}Sr will therefore always have an equal activity of ^{90}Y included within it. The combined energy spectrum of both decays is shown in Fig. B.1.

The total stopping power and the average range of electrons in polystyrene (the scintillating fibre core material) and 1,2,4-trimethylbenzene (the base material of the liquid scintillator) are shown in Fig. B.2. The specific density of polystyrene and of the liquid scintillator EJ-305 by Eljen are 1.06 and 0.89 respectively. The stopping power needs

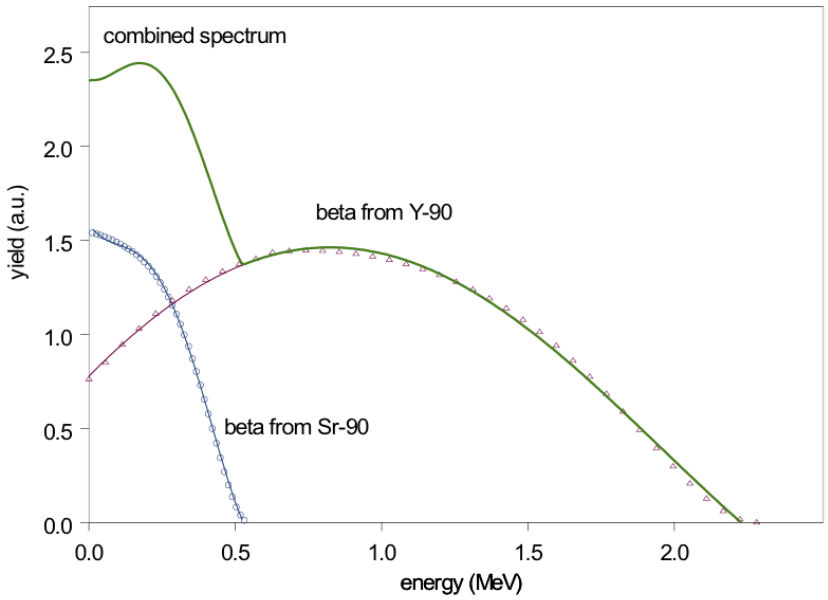

Figure B.1: Energy spectrum of electrons emitted from a ^{90}Sr source[114].

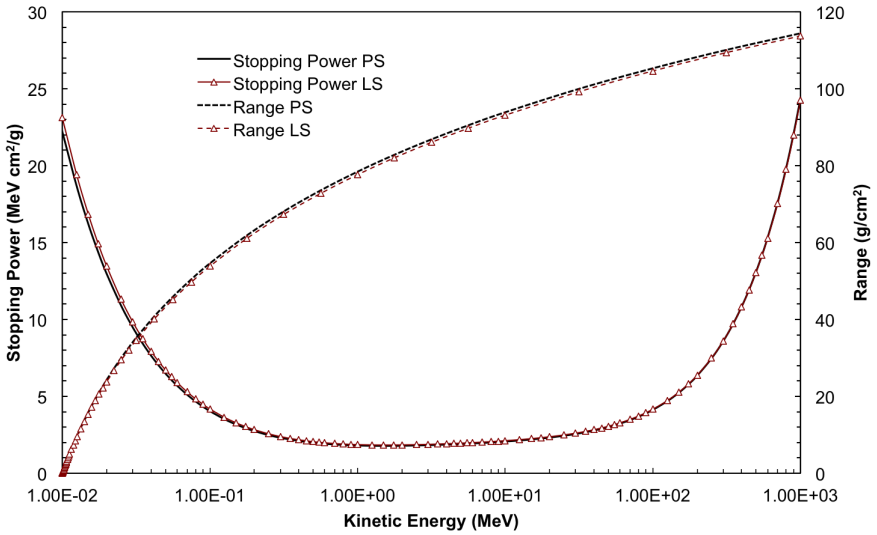

Figure B.2: Total stopping power and range of electrons in polystyrene (PS) and in 1,2,4-trimethylbenzene (LS)[165].

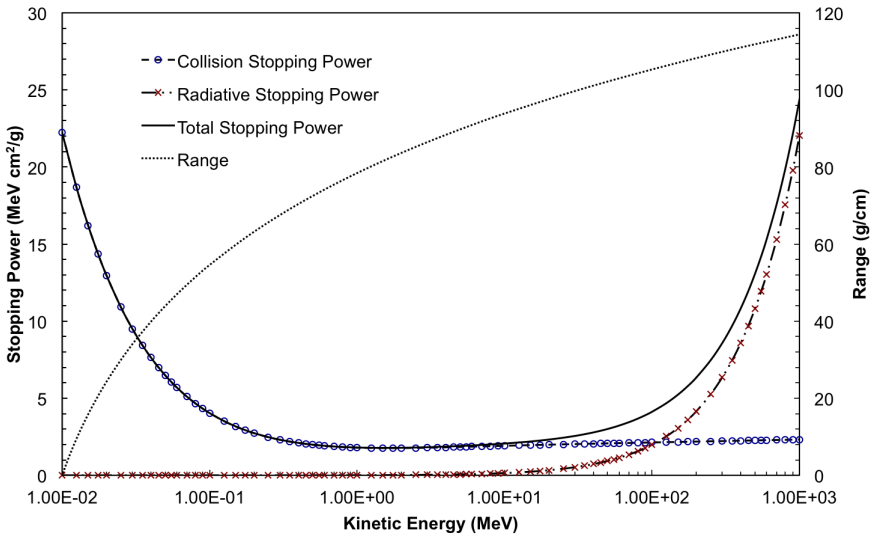

Figure B.3: Collision, radiative and total stopping powers and range of electrons in polystyrene (PS)[165]. The curves are almost identical for 1,2,4-trimethylbenzene.

to be multiplied with the density in order to obtain the energy loss in MeV/cm and the range needs to be divided by the density in order to obtain it in the unit cm. With densities of the order of 1 both for polystyrene and the liquid scintillator, one sees that electrons up to a maximum energy of about 2.2 MeV have an energy loss of the order of 2 MeV/cm.

Appendix C

Metrology of the ALFA 2006 prototype detectors

This appendix is adapted from the following ATLAS technical notes

- A. Braem, C. Joram, **A. Mapelli**, A. Kocnar, and J. Pospichal, "Metrology results of the ALFA 2006 prototype detectors", *CERN-ATL-LUM-PUB-2006-007*, CERN, 2006
- **A. Mapelli**, A. Braem, C. David, A. Folley, C. Joram, L. Kottelat, M. van Stenis, H. Stenzel, and M Szauter, "Design, Construction and Metrology of the Overlap Detectors for the ALFA system", *CERN-ATL-LUM-PUB-2006-008*, CERN, 2006

C.1 The ALFA 2006 prototype detectors

For the 2006 test beam of the ALFA scintillating fibre detector three different detectors were fabricated, all based on Kuraray SCSF-78 0.5 mm^2 square fibres. The details of the fabrication of the tracking detectors and of the overlap detectors can be found in Sections 4.3.1 and 4.4.1 respectively.

- 10_2_16 is a detector with 10 UV planes of 16 fibres each. The detector is mainly aimed for spatial resolution studies.
- 2_2_64 is a detector with 2 UV planes of 64 fibres each. The detector reflects the current baseline design for the ALFA detectors to be installed in the Roman Pots.
- OD1 and OD2 are two identical Overlap Detectors with 2 plates consisting of 2 layers with 2 $\times$ 30 fibers each.

The detector 2_2_64 is shown in Fig. C.1. About 30 fibres on each side are cut under an angle of 90° and aluminium coated before assembly. The other fibres are machined after gluing under an angle of 45° and left uncoated. The design of the detector 10_2_16 is similar, however all fibres are cut under 45°. The sides of all fibres are vacuum coated over the full length with a reflective Al film of about 100 nm thickness. Its main purpose is to suppress cross-talk of the primary scintillation light between adjacent fibres. However the reflective side coating also improves the light yield of fibres with a 45° cut.

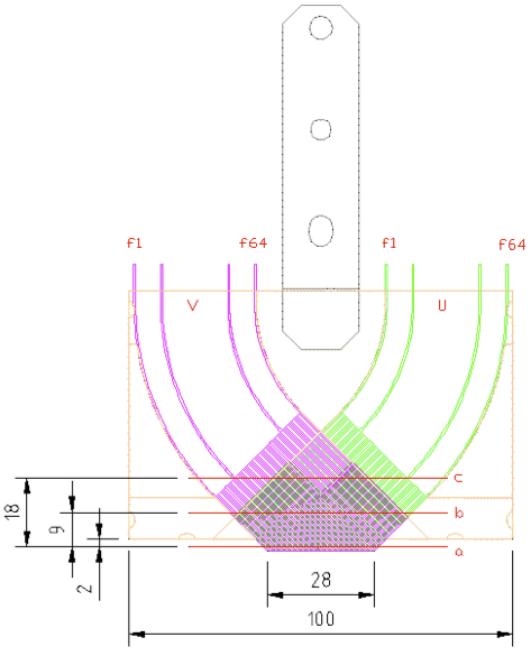

Figure C.1: Design of one plane of the detector 2_2_64. The second plane (not shown) is identical to the first one, except that it is horizontally displaced by nominally 353.5 μm (= 500 μm $\times\sqrt{2}$ / 2).

C.2 The coordinate measurement machine

The measurements were performed with an optical coordinate measurement machine (CMM) of type SmartScope CNC 250 from the company OGP, Optical Gaging Products Inc., (see Fig. C.2, left). The machine allows to measure the coordinates X,Y,Z with a precision better than $(3 + 6L/1000)$ μm, L being the measured length in mm. The measurement range is 300 × 150 × 200 mm (X,Y,Z). The machine is equipped with a motorized 12× zoom, which allows magnifications in the range 32 to 280 (64 to 560 with an additional lens). The sample can be illuminated with a ring light source which is subdivided in sectors and annular zones. It allows illuminating the fibres

under different angles to obtain the best contrast and definition of the fibres edge. The CMM is equipped with the software Measurex which is able to detect edges and more complex objects. The convex shape of the fibres, possible pitch variations, and other small irregularities made it difficult to program the machine for a fully automatic measurement. It was found more time effective to perform the measurements in a quasi-manual mode. After aligning the CMM coordinate system to the object under test, the operator moved the optical cursor with a joystick to the desired position, usually the boundary between two fibres. The fact that the fibres are coated with a reflective Al film in combination with the rounded edges leads to optical phenomena in the CMM optics which complicate the identification of the fibre edge (see Fig. C.2, right). The software memorized these position (X,Y,Z) together with comments in a data file for later analysis.

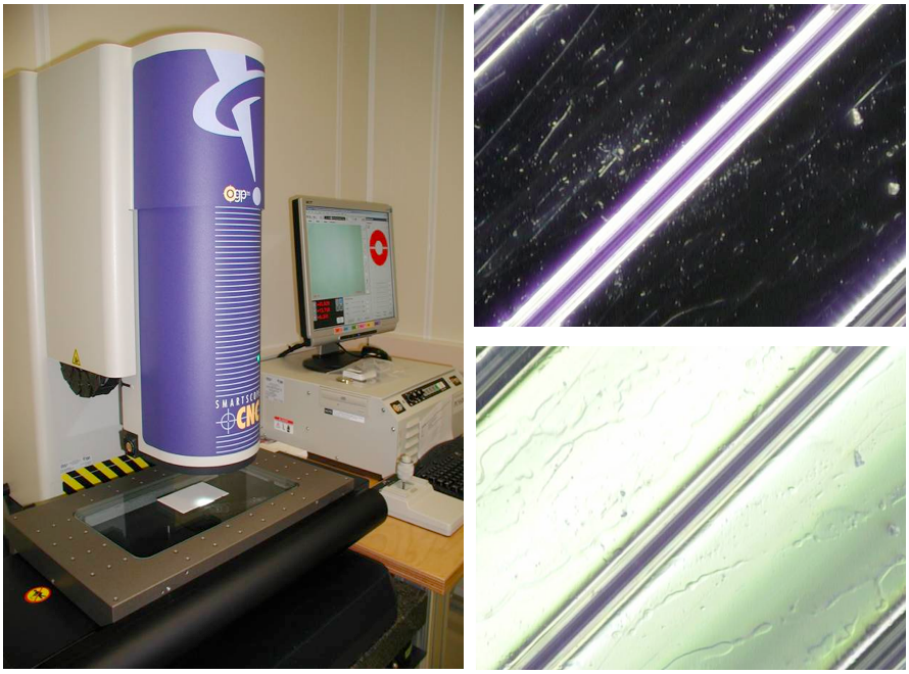

Figure C.2: Left: Photograph of the CMM and its control PC. Right: Two photographs of fibre layers for different illumination. The appearance of the gap region between two fibres is very sensitive to the chosen parameters of the light source (angle, intensity). The gap region exhibits several dark bands which are optical phenomena related to the convex shape of the fibres.

C.3 Measurement procedures and data parameterization

The metrological control of the detectors was performed in several steps throughout the fabrication process.

1. An improved assembly procedure and modifications of the assembly tool compared to the 2005 model guarantee the correct positioning of the spacers relative to the central substrate. Dimensional imperfections of the components would have no impact. A metrological control of the components was therefore skipped.

2. The tool was used to align and glue the two 45° spacer plates on the U and V side of the central substrate plate. The correct positioning of the spacers was verified by a metrological control after the glue was hardened. The results of this test are not discussed in this note.

3. After positioning and gluing the fibres on the substrate, a second metrological analysis was performed where the position of every fibre was determined. A Cartesian reference system is defined by the intersection of the straight lines $\bar{P_1P_2}$ and $\bar{P_1P_4}$ with the origin in the left or right bottom corner of the assembly. The x-positions of the edges between two fibres are determined at the levels y = -2, 7 and 16 mm (see Fig. C.3).

4. The data is recorded and analysed in the following way:

   (a) The angles α are calculated as where points 1 and 2 correspond to the two most distant available measurements A, B or C. The angles $<\alpha_u>$ and $<\alpha_v>$ are determined as averages per layer. From these the correction angle α_{corr} = $<\alpha_u>$ - $<\alpha_u>$ was calculated, which ideally should be zero.

   (b) The x_i and y_i coordinates of the crossing points CPi of the 16 (64) U and V fibres are calculated. Nominally, the x_i values should be 50.0 mm. The y-value of the crossing points of the first U and 16^{th} (64^{th}) V fibres were taken as reference y_{ref} for the alignment of all planes.

   (c) The correction angle α_{corr} and the differences Δx = 50.0 – $<x_i>$ and Δy = $< y_{ref}$ - $<y_{ref}> >$ are used to determine the positions of the support arms relative to the ceramic plates. The support arms are then glued such that, in the new coordinate system which has its origin in the centre of the upper precision hole and whose y-axis is aligned with the other precision hole, both α_{corr} and Δy disappear. At this moment also the staggering s is introduced. The nominal staggering values are summarized in Table C.1. The coordinates in the new system (x',y') relative to the old ones (x,y) are defined by

$$(x', y') = T + R \cdot \begin{pmatrix} x \\ y \end{pmatrix} = \begin{pmatrix} \Delta x + s \\ \Delta y \end{pmatrix} + \begin{pmatrix} \cos\alpha_{corr} & -\sin\alpha_{corr} \\ \sin\alpha_{corr} & \cos\alpha_{corr} \end{pmatrix} \cdot \begin{pmatrix} x \\ y \end{pmatrix} \quad \text{(C.1)}$$

5. The final metrological control was performed after machining of the 45° fibre ends. The positions of all fibres were now measured in the new coordinate system with origin in the upper precision hole of the support arm. It is the data from this measurement which was finally used in the physics data analysis. A comparison with the previously recorded and transformed data (*c.f.* point 4.c above) showed agreement of the fibre angles to better than 0.05% and of the positions to better than 30 μm.

6. Two complementary measurements were performed:

   (a) The end position of the fibres (y-coordinate) was directly determined.

   (b) After the 10 planes of the 10_2_16 detector were assembled, the detector was mounted under the CMM such that the fibre end cuts could be directly inspected and measured (see Fig. C.4). This allowed for a direct verification of the plane staggering which otherwise is determined only indirectly from the measurements of the individual planes.

Table C.1: Nominal staggering between the 10 planes of the ALFA detectors.

plane	s (mm)
1	0.000
2	0.2828
3	-0.1414
4	0.1414
5	-0.2828
6	0.3536
7	-0.0707
8	0.2121
9	-0.2121
10	0.0707

C.4 Results

All fibre locations are parameterized in the following form:

$$y_i = a_i x_i + b_i \tag{C.2}$$

The parameters a_i and b_i are derived from the measured points A_i, B_i or C_i as

$$a_i = \frac{y_{A,i} - y_{B,i}}{x_{A,i} - x_{B,i}} = y_{A,i} - a_i x_{A,i} \tag{C.3}$$

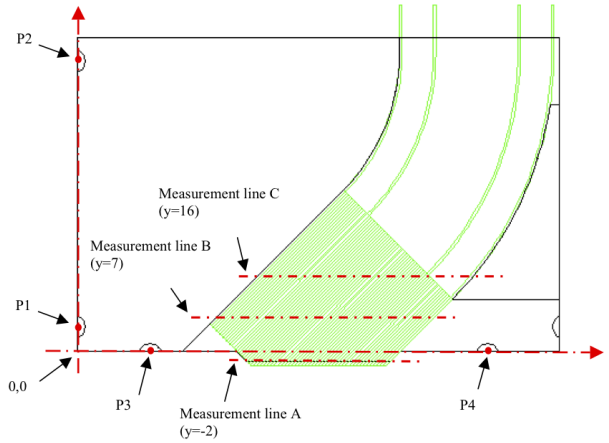

Figure C.3: Schematic representation of a fibre layer (U layer in this case). The y-levels at which the coordinate measurements were performed are indicated as dashed-dotted lines.

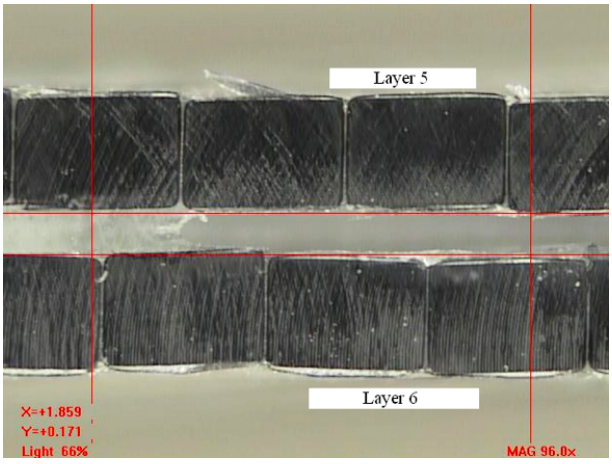

Figure C.4: Photograph taken with the CMM of the fibre ends, machined under 45°. In this view the nominal fibre cross section is 0.5 × 0.707 mm.

The z-position of every fibre is not needed to be known with high precision. It is assumed that all fibres on one layer have the same nominal position. In the following, the plots of the various parameters are presented including the fibre pitches p which were calculated at the $x = 0$ position from the b-parameters:

$$p_i = \frac{1}{\sqrt{2}} |b_1 - b_{i-1}| \tag{C.4}$$

Of interest are the vector-field plots which show the difference of the nominal and measured crossing points of the i^{th} U and the j^{th} V fibres. The differences $dx = x - x_0$ and $dy = y - y_0$ are determined separately, which allows to scale up the deviation by a factor k for better visibility. The vectors point form the nominal crossing point (x_0, y_0) to the scaled measured point $(x_0 + k \cdot dx, y_0 + k \cdot dy)$. The nominal and the measured grid are aligned at the (arbitrarily chosen) crossing point of the fibres U1 and V16 (V64). The staggering plots are derived from the individually measured planes. In the case of the 10_2_16 detector the data is compared to direct measurements.

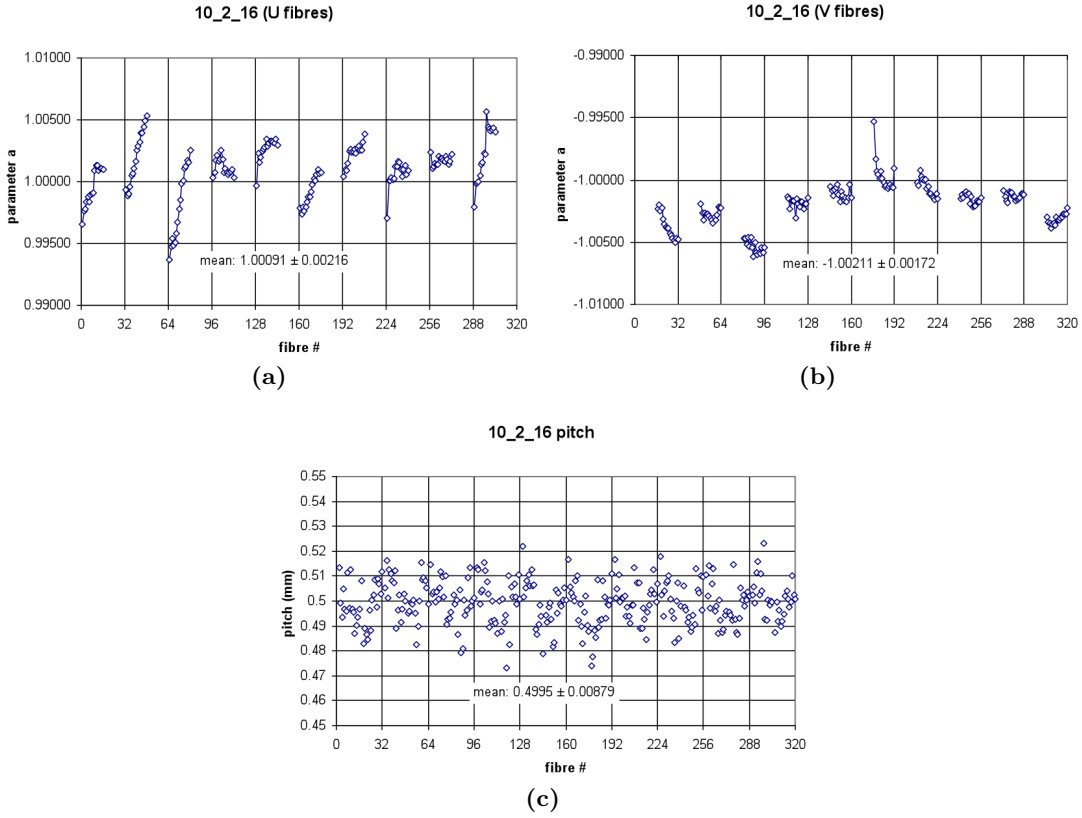

Figure C.5: Fibre slope a for all (a) U layers and (b) V layers of detector 10_2_16. (c) Fibre pitch for all 20 × 16 fibres of detector 10_2_16.

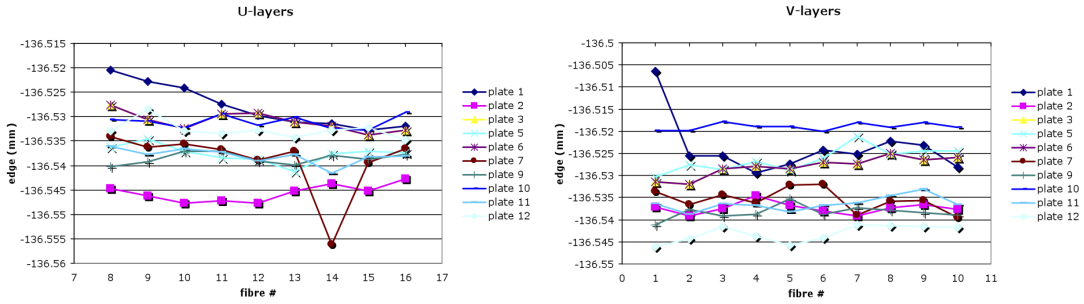

(a) **(b)**

Figure C.6: Y-coordinate of the fibres ends for the (a) U-layers and (b) V layers of detector 10_2_16.

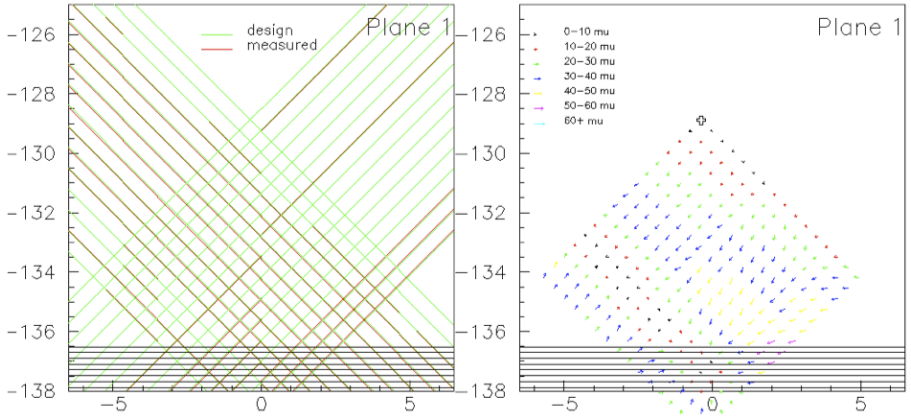

(a)

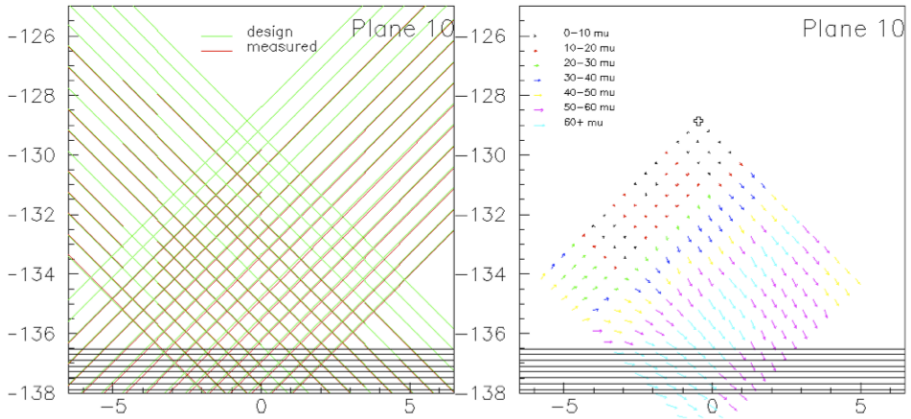

(b)

Figure C.7: Vector field plot for (a) plane 1 and (b) plane 10 of detector 10_2_16. The deviations are scaled by a factor 5. The alignment point (crossing of fibre U1 and V16) is marked with a cross.

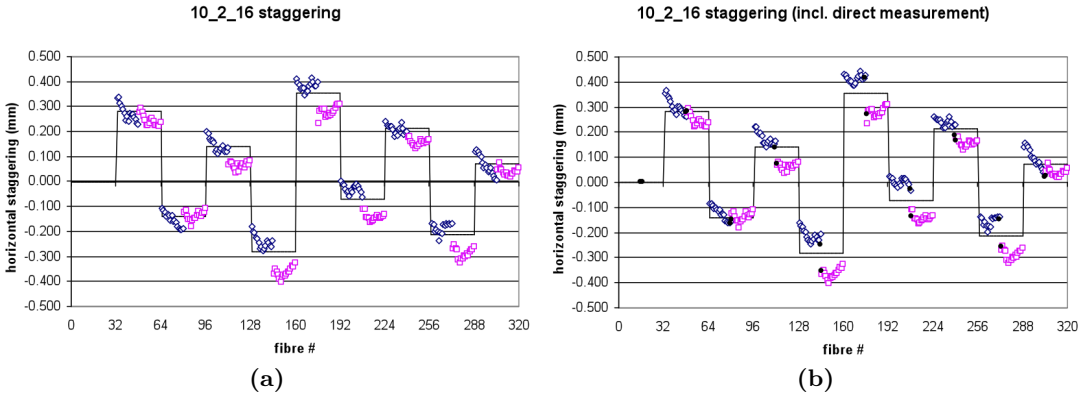

(a) (b)

Figure C.8: (a) Fibre staggering relative to the fibres of the first plane (fibres 1 – 32) of detector 10_2_16. The staggering is calculated from the measurements on the individual planes and the subsequent transformations. (b) Direct staggering measurements on selected fibres (U1 and V16) of detector 10_2_16 are superimposed to the data plotted in (a).

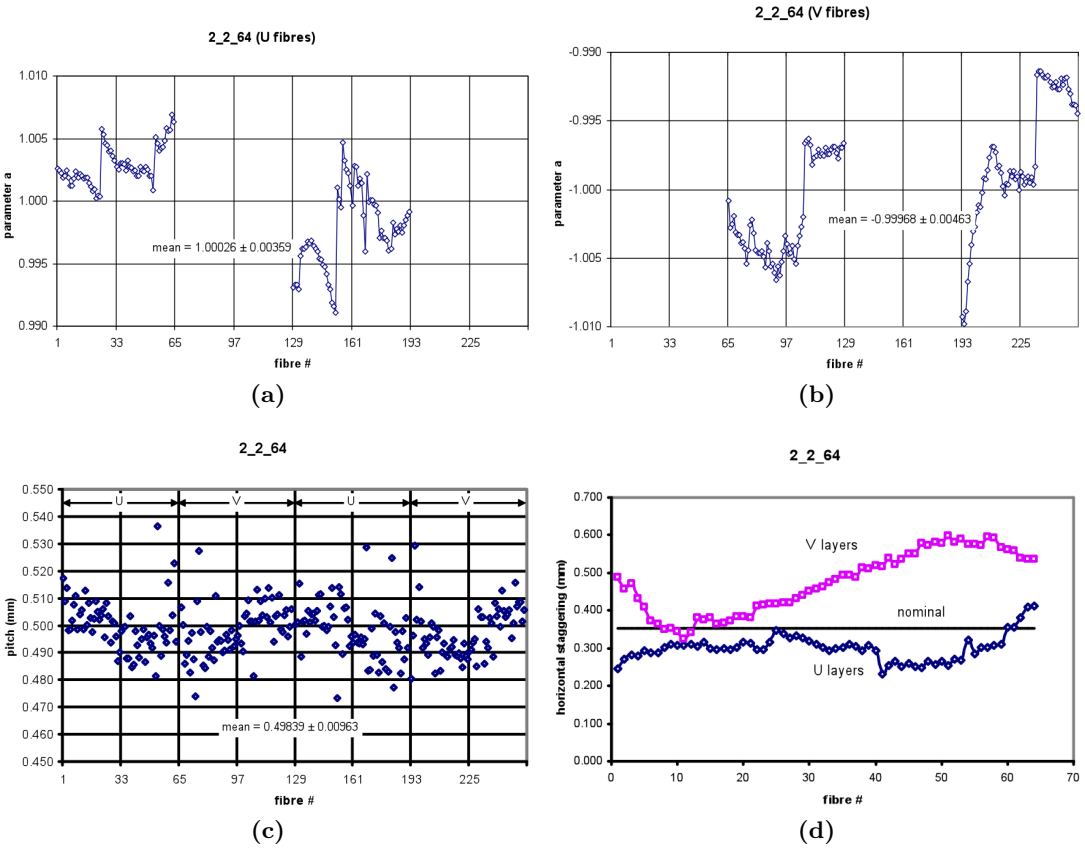

(a) (b)

(c) (d)

Figure C.9: Fibre slope a for all (a) U layers and (b) V layers of detector 2_2_64. (c) Fibre pitch for all 4 × 64 fibres of detector 2_2_64. (d) Fibre staggering of the 2 × 64 fibres of the second plane of detector 2_2_64 with respect to the fibres of the first plane. The nominal staggering value is 353.5 μm (horizontal line).

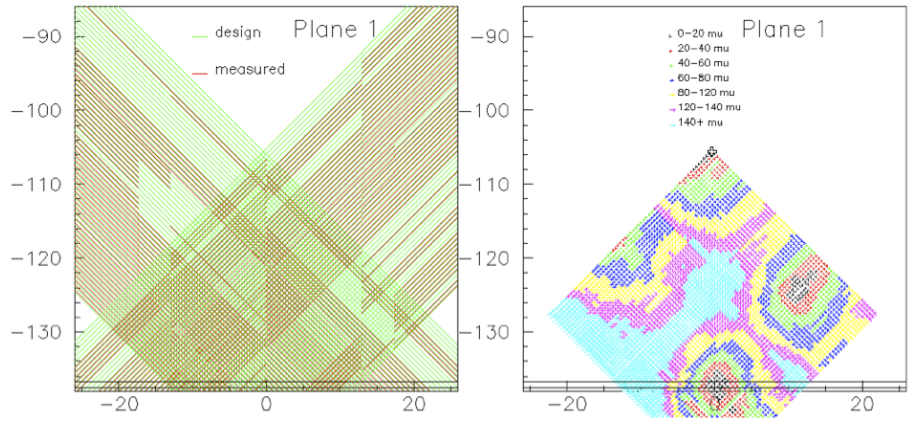

(a)

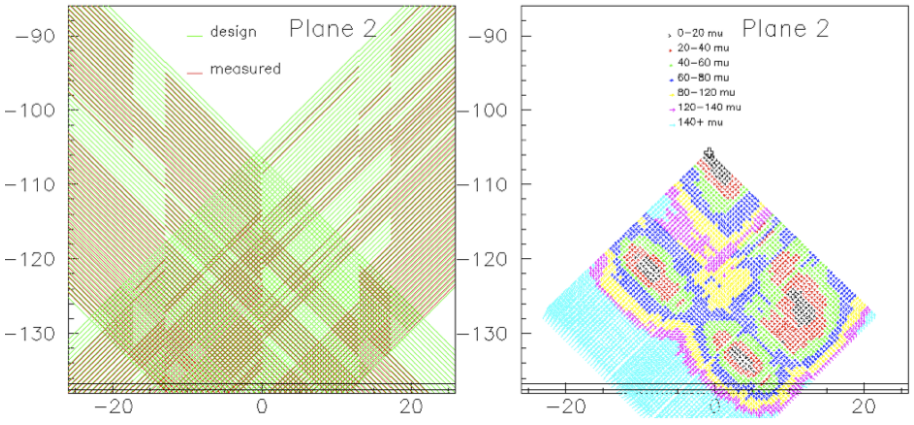

(b)

Figure C.10: Vector field plot for (a) plane 1 and (b) plane 2 of detector 2_2_64. The deviations are scaled by a factor 5. The alignment point (crossing of fibre U1 and V64) is marked with a cross. The distortions are typically two times larger than for the detector 10_2_16 (see Fig. C.7).

C.5 Monte-Carlo studies of the achievable detector resolution

A simple geometrical Monte-Carlo code has been used to estimate the achievable detector resolution σ_x, σ_y based on the measured fibre geometry data (a, b, z). The code generates particles within a defined spot size (x_{min} - x_{max}, y_{min} - y_{max}) and an angular polar range (0 - θ_{max}) relative to the detector normal. It extrapolates the particle trajectories and calculates the impact points on the fibre layers, from which the hit fibres can be identified, taking into account their measured position and also the non active fibre cladding. A single fibre detection efficiency different from one is simulated by eliminating hits accordingly. Finally, the code uses either the centre-of-gravity of the minimum-overlap algorithms to reconstruct the particle coordinates x and y. The reconstruction relies obviously on the precise knowledge of the actual position of the fibres. In the basic version the code does not simulate cross-talk, nor does it produce false noise hits or matter related effects like multiple scattering. The detector resolution is restricted to purely geometrical effects and represents therefore a somewhat optimistic approximation, which appeared to be realistic at the time of the test beam.

C.5.1 Detector 10_2_16

Assuming full detection efficiency and absence of inactive cladding, *i.e.* 20 hits per track, the detector has an ultimate theoretical resolution of $50/\sqrt{12} = 14.4$ μm. To estimate the contribution of the geometry only, the simulation was run with the measured geometry but with unrealistic cladding-less fibres. The result is a spatial resolution of 19.9 μm (see Fig. C.11). Quadratic de-convolution indicates that the geometrical imperfections of the detector lead to a resolution term of about 14 μm. Simulating a more realistic detector (10 μm cladding, single fibre detection efficiency 95%, angular spread 1 mrad) results in a resolution of 22 μm.

C.5.2 Detector 10_2_64

At the time of the 2006 test beam the detector 10_2_64 (10 planes with 2 $\times$ 64 fibres each) was only a virtual object. To estimate its resolution, a geometry file was produced which comprised the measured geometry of the first plane of the existing detector 2_2_64 and 9 artificial planes created by a random number code. The a-parameters of the 9 planes are random permutations of the measured a-parameters of the existing first plane of 2_2_64. The b-parameters were produced by accumulating pitch values

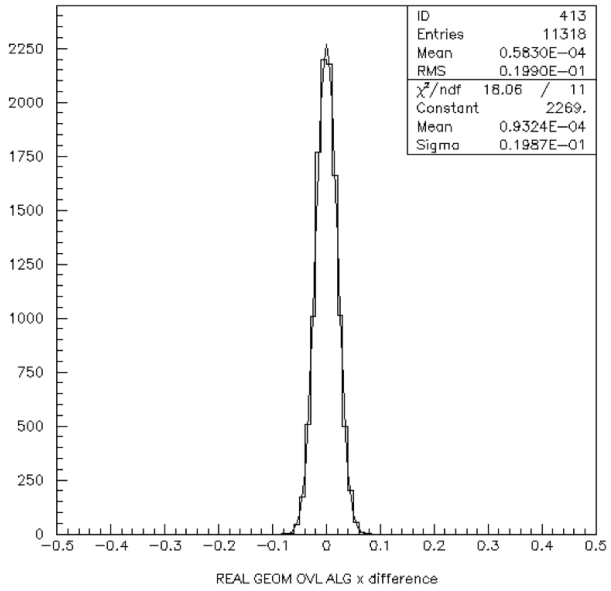

Figure C.11: Result of a Monte-Carlo study using the as measured geometry of detector 10_2_16, however unrealistic cladding-less fibres. The minimum overlap algorithm is used to reconstruct the tracks.

which were randomly generated from a normal distribution with mean 0.70711 mm and sigma = 15 μm. The staggering of the individual layers was based on the nominal values plus random distortions of up to $\pm$50 μm (uniform distribution). Vector field plots (see Fig. C.12a) and staggering distribution (Fig. C.12b) of the virtual detector look similar to the ones measured for 2_2_64. Running the geometrical simulation program for the idealized (cladding-less, fully efficient, zero beam divergence) virtual detector leads to a resolution of 26.8 μm, *i.e.* a geometrical resolution term of 22.6 μm. The more realistic simulation (10 μm cladding, single fibre detection efficiency 95%, angular spread 1 mrad) ends up at a resolution of 27.5 μm (see Fig. C.12c). The code which generates the virtual detector geometry was run with different seed values for the random number generator. This led to different patterns in the vector field plots and the staggering distribution. The final result, namely the spatial resolution obtainable with the detector was practically independent of the seed.

C.6 Overlap detectors

During their construction the overlap detector prototypes were measured three times. The first survey asserted the fibre position on the ceramic plates. The second survey was required to precisely position the metallic blade with respect to the ceramic plates. To do so, the blade was positioned on a tool with two precision pins and the centre

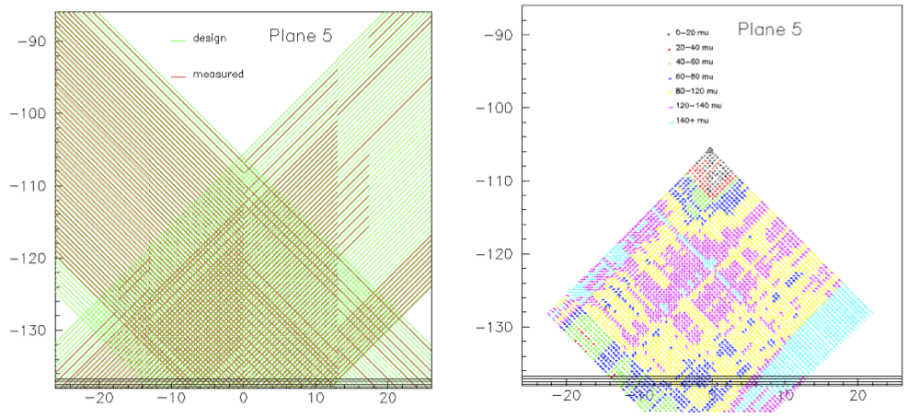

(a)

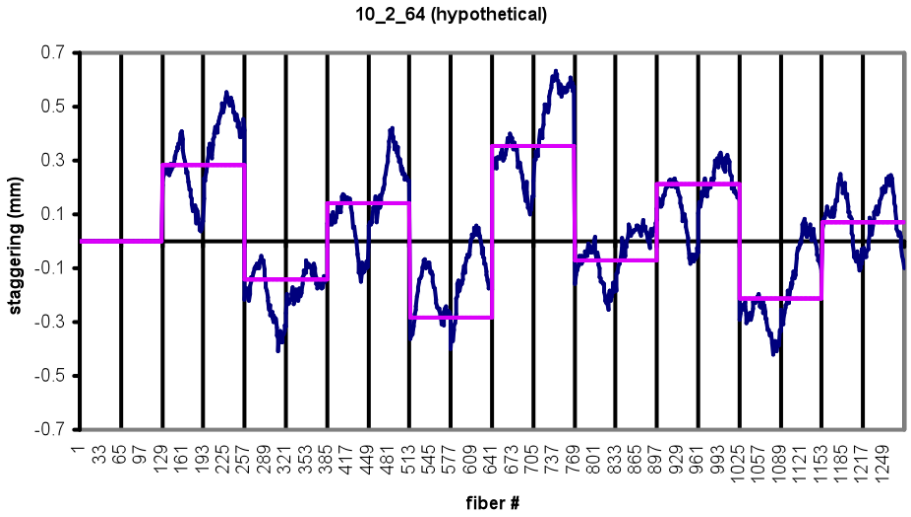

(b)

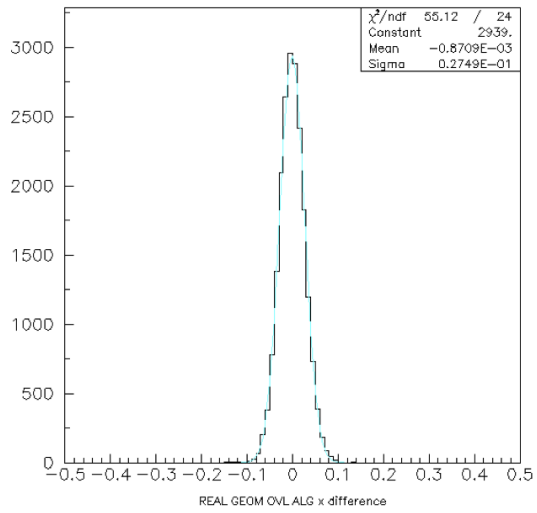

(c)

Figure C.12: (a) Vector field plot for hypothetical plane 5 of detector 10_2_64. (b) Staggering distribution of the virtual detector 10_2_64. (c) Simulated spatial resolution for the virtual detector 10_2_64.

of the upper pin was defined as the origin of the two axis used to re-measure the fibre positions as shown in Fig. C.13a. The centre of the oblong hole of the blade was chosen as a second point to define the y-axis. The ceramic plate was then positioned against three precision pins C1, C2, and C3.

The end points of the lower two fibres were measured on each side of the plate. These two points defined a straight line and a spacer was inserted between the plate and pin C3 to move the plate such that the centre of this line would stand at x=0. The plate was then rotated in order for the fibres to be perpendicular to the blade's vertical axis (the y-axis). This rotation was achieved by placing a spacer between the plate and either pin C1 or C2 according to the angle to be corrected. Finally, identical spacers were inserted between the plate and spacers C1 and C2 to place the fibres at the required height. The position of each blade relative to the plates was chosen to produce the desired vertical staggering.

To determine the exact position of the fibres, the y-coordinate of the gap between the fibres was measured at three different x positions (20, 23 and 25 mm from the centre of the system) as drawn in Fig. C.13b. The pitch and the centre of the fibres were determined and the slopes calculated (see Figs. C.14a and C.14b). Within a layer the slopes of all the fibres have a small variation but from one layer to the other there can be large variations. Moreover from the plot of Fig. C.14b it is clear that the pitch of all the fibres is very close to the expected 500 μm except for fibre 16 of every layer. These two geometrical effects come from the imprecise alignment of the upper fibre on the front side of the substrate and the lower fibre on the back side. The positioning of the fibres on each side of the detector is done relative to the inner ceramic plate's lower edge, thus within the layer the pitch is well controlled but not from one side to the other. This imperfection had to be corrected in the next prototype. The staggering between the fibres of OD2 and OD1 is plotted in Fig. C.14c. Its mean value is less than 10 μm away from the expected value of 250 μm (fibre size divided by the number of plates per OD, namely two) but it goes as far as 350 μm. The variation in the staggering comes from the accumulation of the small displacement of every fibre during the glueing. Good care must be taken during this step of the construction sequence. This geometrical data was recovered in a geometry file that was used to simulate the detector in a beam and to reconstruct real events from the test beam that took place in October 2006 at CERN.

To estimate the achievable vertical resolution "y, particle tracks were generated with a simple geometrical Monte-Carlo code and the hits with the detector were reconstructed

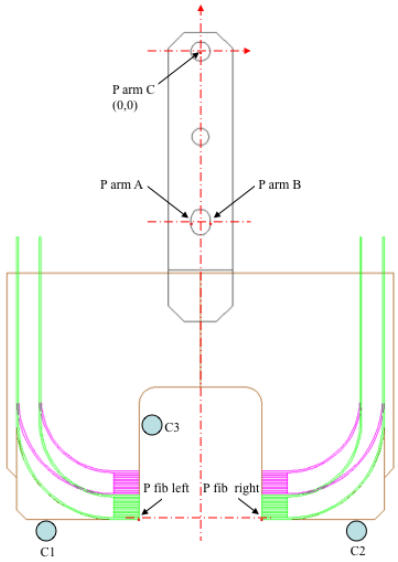

(a)

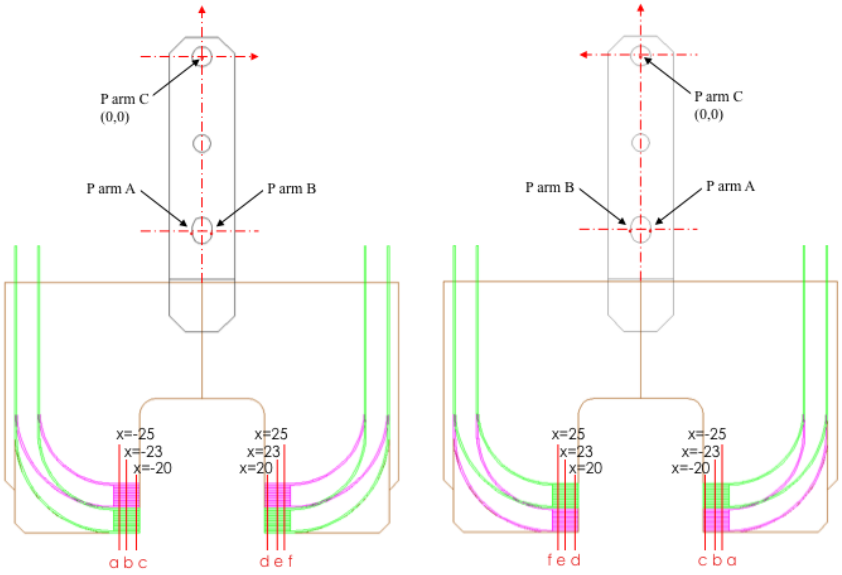

(b)

Figure C.13: (a) Sketch of one plate of the ODs under measurement for the glueing of the blade on the ceramic plate. (b) Metrology procedure for the final survey of the four overlap detector plates to determine the fibres position.

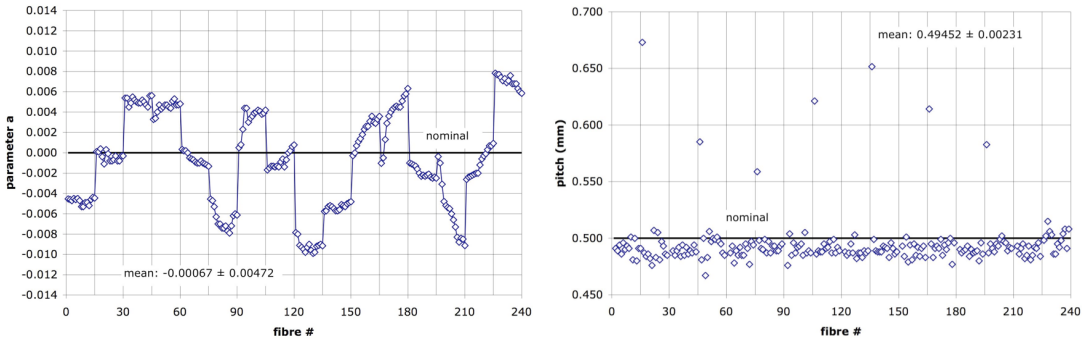

(a)

(b)

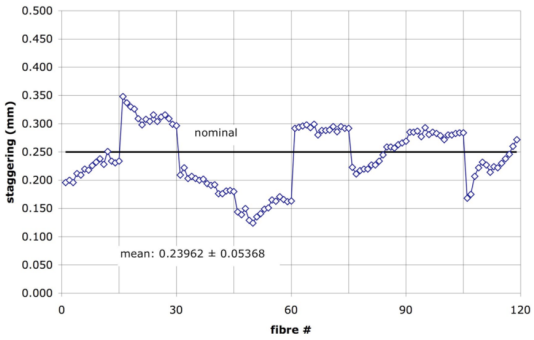

(c)

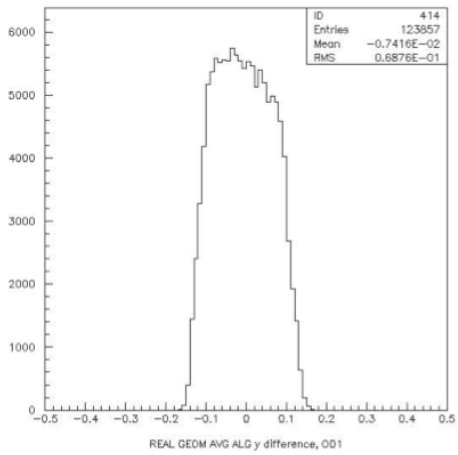

(d)

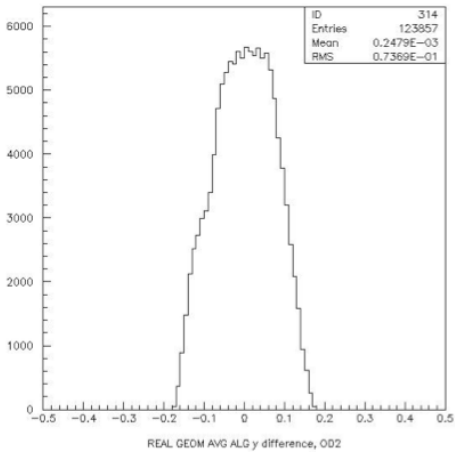

(e)

Figure C.14: (a) Parameter a (fibre slope) for all the fibres of the overlap detectors. (b) Fibre pitch of the overlap detectors. (c) Staggering between the fibres of the two plates of OD2 and OD1. Results of the Monte-Carlo study using the measured geometry for (d) OD1 and (e) OD2.

taking into account the measured fibres geometry. The code uses the average algorithm to reconstruct the y-coordinate of the particle.

$$y_{rec} = \frac{1}{2}\left(y_{OD1,L1} + y_{OD1,L2}\right) - \frac{1}{2}\left(y_{OD2,L1} + y_{OD2,L2}\right) \tag{C.5}$$

where $y_{ODi,Lj}$ is the coordinate of the fibre hit in the j^{th} layer of the the i^{th} overlap detector. The plots of Figs. C.14d and C.14e show the residual reconstructed coordinate relative to the hit coordinate. The standard deviation of these box plots gives us the resolution we can expect from each overlap detector with their measured geometry. The theoretical resolution of the ODs, taking into account the inactive cladding of the fibres, is 240 μm $/\sqrt{12} = 69$ μm. Simulating the ODs with a detection efficiency of 95% resulted in a resolution of 69 μm for OD1 and 73 μm for OD2. Effects such as cross-talk or multiple scattering were not simulated; the divergence between the theoretical and simulated resolution of OD2 is attributed to geometrical imperfections.

C.7 Conclusions

The results of the metrological measurements performed on the detectors 10_2_16 and 2_2_64 built for the ALFA beam tests in 2006 are presented. The geometrical quality of 10_2_16 is generally good. In particular, the length of the fibres at the 45° cuts could be adjusted with high precision for all 10 planes. The vector field plots of the distortion of the UV crossing points show a consistent pattern, which indicates that the positioning precision degrades with the distance of the fibres from the ceramic spacer. The geometrical simulation study indicates that the detector should be easily capable to reach the targeted 30 μm resolution. The detector 2_2_64 shows significantly larger deviations from the ideal geometry. Cumulative effects in the a-parameter and, even more expressed, in the staggering are observed. The vector field plots show similar patterns as for 10_2_16, however the distortions are typically a factor 2 larger. Despite these substantial distortions, a hypothetical detector 10_2_64 of comparable quality would have a resolution just below 30 μm. The distortion patterns observed in 2_2_64 reveal a weakness of the currently applied fibre gluing procedure. The fibres positions in the central part, far away from the spacers, are subject to cumulative effects (glue excess, fibre diameter, fibre deformation) which are difficult to control. Improvements of the assembly and gluing method should be studied to reduce the distortions and give additional safety margin for the spatial resolution.

Appendix D

Monte Carlo simulations of microfluidic waveguides

In order to estimate the optical properties of the microfluidic waveguides, Monte Carlo simulations are performed. The method consists in generating photons isotropically in the channels and counting the photons reaching their ends. In these calculations, the photons are considered as elementary particles. They are transported across microchannels modelled as three dimensional rectangular volumes in which the attenuation is neglected. The probabilities of reflection R and transmission T are evaluated with Fresnel equations for non-polarized light at all the interfaces between the liquid scintillator and the metal claddings, and between the metal claddings and the SU-8 walls or the silicon substrate. The probabilities of reflection R and transmission T are expressed as follows

$$R = \frac{R_x + R_y}{2} \tag{D.1}$$

and

$$T = 1 - R \tag{D.2}$$

where R_x and R_y are the reflectances for the x-polarized mode and y-polarized mode[166] such that

$$R_x = \left(\frac{n_1 \cdot \cos\theta_1 - n_2 \cdot \cos\theta_2}{n_1 \cdot \cos\theta_1 + n_2 \cdot \cos\theta_2} \right)^2 \tag{D.3}$$

and

$$R_y = \left(\frac{n_2 \cdot \cos\theta_1 - n_1 \cdot \cos\theta_2}{n_2 \cdot \cos\theta_1 + n_1 \cdot \cos\theta_2} \right)^2 \tag{D.4}$$

The x-polarized mode is called the transverse (TE) polarization or orthogonal polarization, since the electric fields are orthogonal to the plane of incidence. The y-polarized mode is called the transverse magnetic (TM) polarization since the magnetic fields are orthogonal to the plane of incidence, or the parallel polarization since the electric fields are parallel to the plane of incidence. The x and y polarizations are also called the s and p polarizations.

As shown in Fig. D.1, at every interface, the incidence, refraction, and reflection, labelled with subscripts 1, 2, and 3, respectively, are such that the angles of reflection θ_3 and incidence θ_1 are equal and the angles of refraction θ_2 and incidence θ_1 satisfy Snell's law

$$n_1 \cdot \sin\theta_1 = n_2 \cdot \sin\theta_2 \tag{D.5}$$

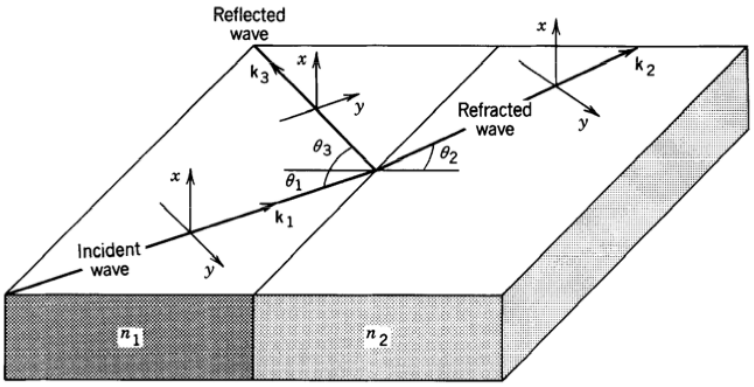

Figure D.1: Reflection and refraction at the boundary between two media with different refractive indices[166].

A given number of scintillation photons γ_{scint} is generated isotropically in the liquid scintillator (EJ-305) contained in the microchannels (see Fig. D.2). They are coated with a thin layer of gold deposited by sputtering on the SU-8 GM-1075 walls and on the silicon substrate. The channels are closed with a foil of aluminum-coated Mylar.

The photons travel in the scintillator in all directions and the probabilities of reflection R and transmission T are estimated with Eqs. D.1 and D.2 for every photon as they reach an interface with aluminum or gold. A fraction of photons are reflected with an angle equal to the angle of incidence. The photons which are not reflected back in the

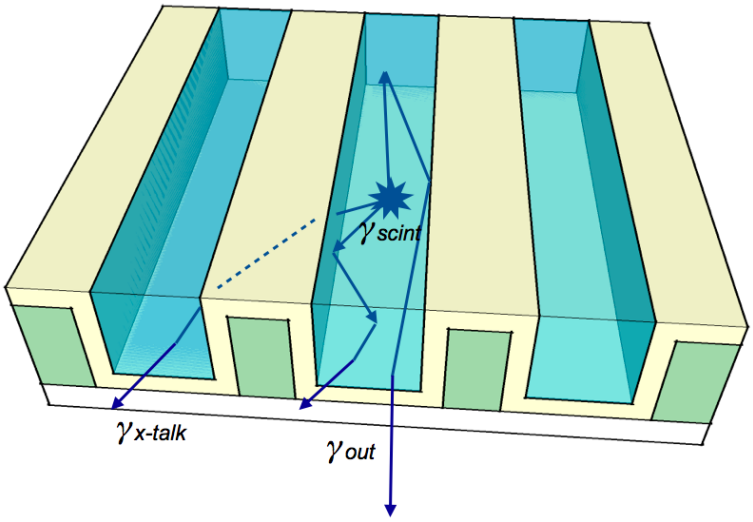

Figure D.2: Cross-section of two microfluidic channels containing the liquid scintillator EJ-305. They are coated with a layer of gold deposited by sputtering on the SU-8 GM-1075 walls and on the silicon substrate. The channels are closed with a foil of aluminum-coated Mylar (not shown).

channel are transmitted in the metal coatings with an angle satisfying Snell's law (see Eq. D.5). These photons can then either be reflected or transmitted at the following interface with silicon, SU-8 or air. The calculations are repeated for every boundary until they reach the air surrounding the device. To take into account the attenuation at each reflection on the metal coatings, the photons can only be reflected a finite number of times before they are totally lost. The ratio of photons γ_{out} escaping the channel in which they were generated, on the side in contact with the photodetector, are counted. The ratio between γ_{out} and γ_{scint} allows to determine the collection efficiency ε_{coll} and the reflection efficiency ε_{coll} of the channels. Moreover, the photons γ_{x-talk} escaping the neighbouring channels give an information on the cross-talk between the microchannels.

Appendix E

SU-8 embedded microchannels

E.1 Fabrication of multi-layers in SU-8

Multi-layer structuring of SU-8 is usually achieved by spin-coating additional layers on top of layers that have already been developed. This has the disadvantage that the consecutive spin-coatings are limited by the topography of the previous structured layers. In order to prevent this limitation, the approach followed to fabricate embedded SU-8 microchannels is to consecutively coat and expose SU-8 layers with different UV sensitivities and to develop them all at once during a single development step at the end of the process.

E.1.1 Process-flow of embedded microchannels

A layer of 25 μm of SU-8 (GM1060 from Gerstelec) is deposited and fully polymerized on a 4" silicon wafer coated with a sacrificial layer (see Fig. E.1a). A second layer of SU-8 GM1075 is spin-coated and baked to obtain a homogeneous thickness of 200 μm. Exposure through a mask with the design of the microchannels is performed and followed by a post-exposure bake for the cross-linking of the exposed regions (see Fig. E.1b). At this point, instead of developing this layer a third layer of 50 μm of a highly UV absorbing formulation based on the GM1070 photoresist is spin-coated on top. After soft-baking, it is exposed through a mask to leave the inlet and outlet regions of the microchannels non-polymerized (see Fig. E.1c). A post-exposure bake for the three layers is performed after this second and last exposure. The development of the second and third layers of SU-8 is performed at once in a specific developer (see Fig. E.1d). The unpolymerized resin is dissolved and driven out of the channels by agitation. The developed embedded channels are cleaned in a fresh PGMEA bath and

rinsed with isopropanol (see Fig. E.2). The SU-8 stack is released from the carrier wafer in order to obtain a microfluidic device entirely made of SU-8 (see Fig. E.1e).

E.1.2 Characterisation of UV absorbing SU-8 photoresists

This fabrication process relies on the fact that the upper SU-8 layer has an enhanced UV absorption with respect to the lower layers. It is crucial for the fabrication of embedded channels in SU-8 to precisely control the polymerization thickness of the top layers in order to release the microchannels. Various GM1070 based photoresists containing different photo-acid generator (PAG) concentrations were studied in terms of sensitivity and contrast (see Table E.1) to find the best option for the fabrication of embedded microchannels. The sensitivity $D_{0.5}$ is the dose necessary to obtain structures with dimensions identical to those on the exposure mask. It is defined as the dose required to polymerize a normalized SU-8 thickness of 0.5 (see Fig. E.3). The GM1070-905 photoresist, with the highest concentration of photo acid generator, was selected to fabricate the embedded microchannels. It shows a low contrast allowing a good control of the polymerized thickness over an exposure range between 2 to 10 s and a sufficient sensitivity to thoroughly polymerize the top layer, from 6 to 50 μm respectively, without affecting the lower layers.

Table E.1: Properties of the GM1070 based SU-8 photoresists with increased photo-acid generator (PAG) concentrations. C_i is the initial PAG concentration.

GM1070 formulation modified	PAG concentration (% weight)	Sensitivity $D_{0.5}$ (mJ / cm^2)	Contrast
902	C_i	13	0.63
903	$2 \times C_i$	20	0.45
904	$4 \times C_i$	32	0.39
905	$6 \times C_i$	78	0.27

E.2 Embedded microfluidic channels used as waveguides

The multi-layer approach proposed in Section E.1 was followed to fabricate embedded SU-8 channels used as microfluidic waveguides with a liquid core and a solid cladding. In order to improve the waveguiding properties of the microchannels an additional step was required to deposit an internal optical coating. The core of interest consists of the liquid scintillator used for the microfluidic particle detector (see Section 5.5.1.3). It has a refractive index of about 1.5 and in order for the microfluidic channel to efficiently guide the scintillation light by total internal reflection the solid core must have a lower

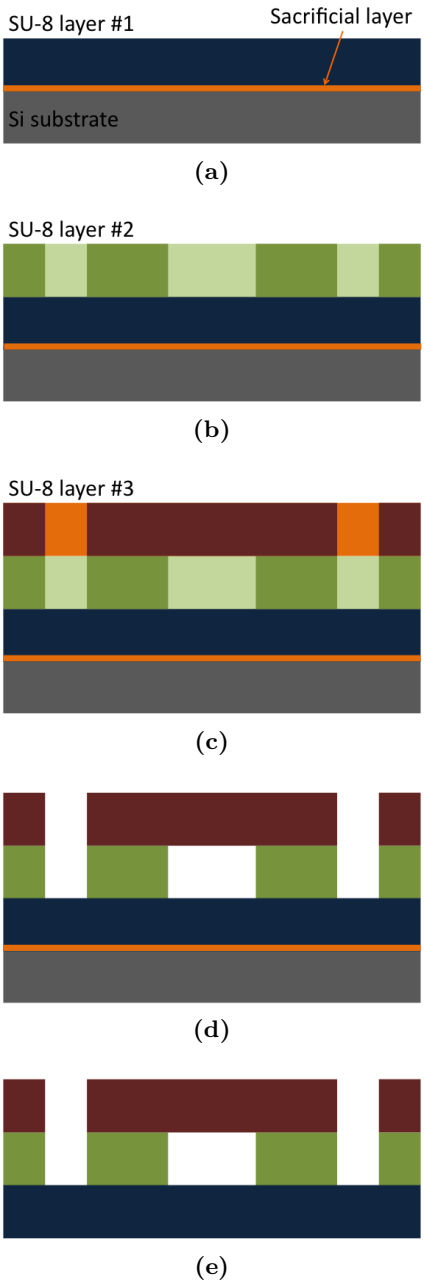

Figure E.1: Fabrication process-flow of embedded microchannels in SU-8. (a) Spin-coating and polymerization of the first layer of SU-8 on a silicon substrate. (b) Exposure of the second layer of SU-8. (c) Exposure of the third layer of SU-8. (d) Development of the second and third layers of SU-8. (e) Release of the SU-8 embedded channels from the substrate.

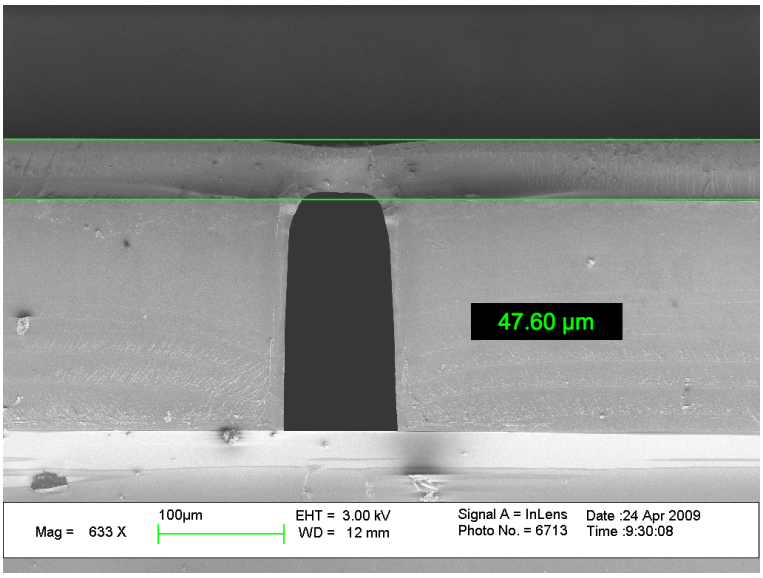

Figure E.2: SEM image of the cross section of an embedded microchannel in SU-8.

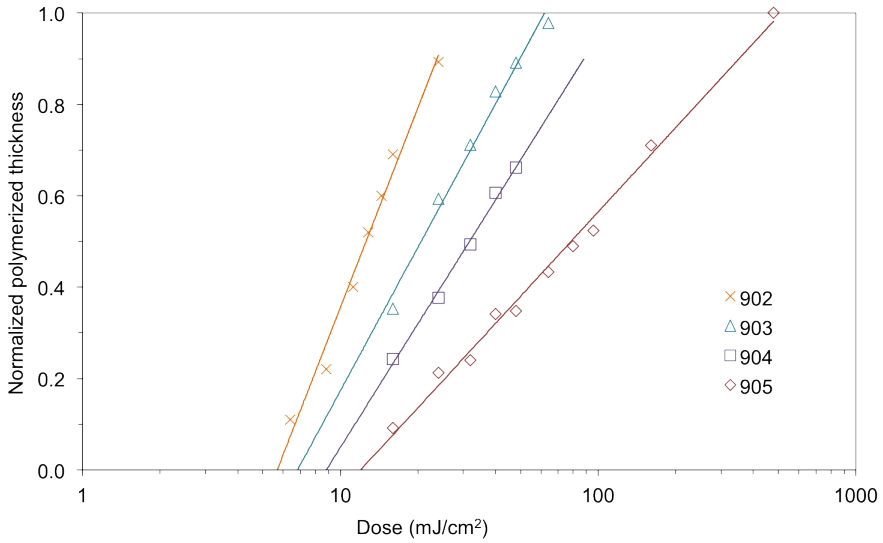

Figure E.3: Linear regression applied to the linear part of the characteristic curve of the special formulations of the GM1070 resist. The polymerized thickness is plotted as a function of the exposure dose. Backside exposure through quartz substrates of GM1070 with an increasing concentration of photo-initiator (GM1070-902, GM1070-903, GM1070-904, GM1070-905) was performed to determine the thickness of polymerization.

refractive index than the fluid it contains. SU-8 has a refractive index of the order of 1.6 and cannot be used as an optical cladding for this application. Among the materials investigated as optical coatings for the embedded microfluidic waveguides, polydimethylsiloxane (PDMS) is a good candidate. It is chemically compatible to the liquid scintillator and its index of refraction is of the order of 1.4.

The deposition of PDMS on the inner walls of the embedded microchannels is carried out in two steps. First, the PDMS is dissolved and injected in the microchannels in order to fill them. When all the walls are covered, the PDMS circulation is stopped and the channels are heated. During this bake, an air flow is forced inside the microchannels. This creates a channel inside the PDMS while the thin layer that has already adhered to the walls of the microchannel polymerizes.

Curriculum Vitae

Alessandro A. Mapelli

Date of birth:	June 7^{th}, 1979
Marital status:	Single
Nationality:	Italian

Experience

From 2010	**CERN, Geneva, Switzerland** Fellow
2006 – 2010	**CERN, Geneva, Switzerland** Doctoral Student
2005 – 2006	**CERN, Geneva, Switzerland** ATLAS Experiment Technical Coordination
2002	**Istituto Nazionale di Fisica Nucleare (INFN-LNF), Frascati, Italy** Internship in the Mechanical Workshop

Education

2006 – 2010	**Ecole Polytechnique Fédérale de Lausanne (EPFL), Switzerland** Ph.D. (Dr. ès Sciences) in Microsystems
2000 – 2005	**Ecole Polytechnique Fédérale de Lausanne (EPFL), Switzerland** M.Sc. (Master of Science) in Microengineering Specialization: Micro- and Nano-Systems
1998 – 2000	**Ecole Polytechnique Fédérale de Lausanne (EPFL), Switzerland** Cours de Mathématiques Spécial
1994 – 1998	**Lycée International de Ferney-Voltaire, France** Baccalauréat Scientifique à Option Internationale

List of publications

Peer-reviewed papers

Microfluidic cooling

A. Mapelli, J. Daguin, H. van Lintel, G. Nuessle, P. Petagna and P. Renaud, "Novel low material budget microfabricated cooling devices for particle detectors and front-end electronics", *Nucl. Phys. B (Proc. Suppl.)* (2011) doi:10.1016/j.nuclphysbps.2011.04.050

M. Fiorini, A. Mapelli *et al.*, "The Gigatracker: An ultra-fast and low-mass silicon pixel detector for the NA62 experiment", *Nucl. Instr. Meth. A* **628**(2011)1 292-295

M. Morel, A. Mapelli *et al.*, "The electro-mechanical integration of the NA62 Giga Tracker time tagging pixel detector", *JINST* **5**(2010) C12023

Microfluidic scintillation detection

A. Mapelli, B. Gorini, M. Haguenauer, S. Jiguet, N. Vico Triviño and P. Renaud, "Development and studies of novel microfabricated radiation hard scintillation detectors with high spatial resolution", *IEEE Trans. Nucl. Sci.* **58**(2011) 1-4

A. Mapelli, B. Gorini, M. Haguenauer, S. Jiguet, G. Lehman Miotto, W. Vandelli, N. Vico Triviño and P. Renaud, "Scintillation particle detection based on microfluidics", *Sens. Act. A* **162**(2010) 272-275

A. Mapelli, B. Gorini, M. Haguenauer, S. Jiguet, N. Vico Triviño and P. Renaud, "Novel radiation hard microfabricated scintillation detectors with high spatial resolution", *Nucl. Instr. and Meth. A* **617**(2010) 400-401

A. Mapelli, B. Gorini, M. Haguenauer, S. Jiguet, N. Vico Triviño and P. Renaud, "SU-8 microfluidic device for scintillating particle detection", *Proc. Chem.*, **1**(2009) 1347-1350

A. Mapelli, B. Gorini, M. Haguenauer, S. Jiguet and P. Renaud, "Development and studies of a novel microfabricated radiation hard scintillation particle detector with high spatial resolution", *Nucl. Phys. B (Proc. Suppl.)*, **197**(2009) 43-47

Absolute Luminosity For ATLAS

A. Mapelli, "ALFA: Absolute Luminosity For ATLAS - Development of a scintillating fibre tracker to determine the absolute LHC luminosity at ATLAS", *Nucl. Phys. B (Proc. Suppl.)*, **197**(2009), 387-390

F. Anghinolfi, A. Mapelli *et al.*, "Hadron beam test of a scintillating fibre tracker system for elastic scattering and luminosity measurement in ATLAS", *JINST* **2**(2007) P07004

S. Ask, A. Mapelli *et al.*, "Luminosity measurement at ATLAS - Development, Construction and Test of Scintillating Fibre Prototype Detectors", *Nucl. Instr. Meth. A* **568**(2006) 588-600

ATLAS

ATLAS Collaboration, G. Aad, A. Mapelli *et al.*, "Measurement of the production cross section for W-bosons in association with jets in *pp* collisions at$\sqrt{s}$ = 7 TeV with the ATLAS detector", *Phys. Lett. B* **698**(2011), 325-345

ATLAS Collaboration, G. Aad, A. Mapelli *et al.*, "Search for Massive Long-Lived Highly Ionizing Particles with the ATLAS detector at the LHC", *Phys. Lett. B* **698**(2011), 353-370

ATLAS Collaboration, G. Aad, A. Mapelli *et al.*, "Measurement of the centrality dependence of J/ψ yields and observation of Z production in lead-lead collisions with the ATLAS detector at the LHC", *Phys. Lett. B* **697**(2011), 294-312

ATLAS Collaboration, G. Aad, A. Mapelli *et al.*, "Measurement of inclusive jet and dijet cross sections in proton-proton collisions at 7 TeV centre-of-mass energy with the ATLAS detector", *Eur. Phys. J. C* **71**(2011), 1512

ATLAS Collaboration, G. Aad, A. Mapelli *et al.*, "Search for quark contact interactions in dijet angular distributions in *pp* collisions at$\sqrt{s}$=7 TeV measured with the ATLAS detector", *Phys. Lett. B* **694**(2011), 327-345

ATLAS Collaboration, G. Aad, A. Mapelli *et al.*, "Charged-particle multiplicities in *pp* interactions at $\sqrt{(s)}$ = 900 GeV measured with the ATLAS detector at the LHC", *Phys. Lett. B* **688**(2010), 21-42

ATLAS Collaboration, G. Aad, A. Mapelli *et al.*, "Observation of a Centrality-Dependent Dijet Asymmetry in Lead-Lead Collisions at$\sqrt{s_{NN}}$ = 2.76 TeV with the ATLAS Detector at the LHC", *Phys. Rev. Lett.* **105**(2010), 252303

ATLAS Collaboration, G. Aad, A. Mapelli *et al.*, "Search for New Particles in Two-Jet Final States in 7 TeV Proton-Proton Collisions with the ATLAS Detector at the LHC", *Phys. Rev. Lett.* **105**(2010), 161801

ATLAS Collaboration, G. Aad, A. Mapelli *et al.*, "Performance of the ATLAS detector using first collision data", *J. High Energy Phys.* **09**(2010), 056

ATLAS Collaboration, G. Aad, A. Mapelli *et al.*, "Readiness of the ATLAS Tile Calorimeter for LHC collisions", *Eur. Phys. J. C* **70**(2010), 723-753

ATLAS Collaboration, G. Aad, A. Mapelli *et al.*, "Drift Time Measurement in the ATLAS Liquid Argon Electromagnetic Calorimeter using Cosmic Muons", *Eur. Phys. J. C* **70**(2010), 755-785

ATLAS Collaboration, G. Aad, A. Mapelli *et al.*, "The ATLAS Inner Detector commissioning and calibration", *Eur. Phys. J. C* **70**(2010), 787-821

ATLAS Collaboration, G. Aad, A. Mapelli *et al.*, "The ATLAS Simulation Infrastructure", *Eur. Phys. J. C* **70**(2010), 823-874

ATLAS Collaboration, G. Aad, A. Mapelli *et al.*, "Commissioning of the ATLAS Muon Spectrometer with Cosmic Rays", *Eur. Phys. J. C* **70**(2010), 875-916

ATLAS Collaboration, G. Aad, A. Mapelli *et al.*, "Readiness of the ATLAS Tile Calorimeter for LHC collisions", *Eur. Phys. J. C* **70**(2010), 1193-1236

ATLAS Collaboration, G. Aad, A. Mapelli *et al.*, "The ATLAS Collaboration", *Nucl. Phys. A* **830**(2009), 925c–940c

ATLAS Collaboration, G. Aad, A. Mapelli, *et al.*, "The ATLAS Experiment at the CERN Large Hadron Collider", *JINST* **3**(2008) S08003

ATLAS arXiv preprints

Measurement of Dijet Azimuthal Decorrelations in pp Collisions $\sqrt{s}$=7 TeV", (2011) CERN-PH-EP-2011-014, submitted to Phys. Rev. Lett.

ATLAS Collaboration, G. Aad, A. Mapelli *et al.*, "Search for supersymmetry using final states with one lepton, jets, and missing transverse momentum with the ATLAS detector in $\sqrt{s}$=7 TeV pp collisions", (2011) CERN-PH-EP-2011-013, submitted to Phys. Rev. Lett.

ATLAS Collaboration, G. Aad, A. Mapelli *et al.*, "Luminosity Determination in *pp* Collisions at $\sqrt{s}$=7 TeV Using the ATLAS Detector at the LHC", (2011) arXiv:1101.2185

ATLAS Collaboration, G. Aad, A. Mapelli *et al.*, "Study of Jet Shapes in Inclusive Jet Production in *pp* Collisions at $\sqrt{s}$=7 TeV using the ATLAS Detector", (2010) arXiv:1101.0070

ATLAS Collaboration, G. Aad, A. Mapelli *et al.*, "Search for Diphoton Events with Large Missing Transverse Energy in 7 TeV Proton-Proton Collisions with the ATLAS Detector", (2010) arXiv:1012.4272

ATLAS Collaboration, G. Aad, A. Mapelli *et al.*, "Measurement of the inclusive isolated prompt photon cross section in *pp* collisions at $\sqrt{s}$ = 7 TeV with the ATLAS detector", (2010) arXiv:1012.4389

ATLAS Collaboration, G. Aad, A. Mapelli *et al.*, "Charged-particle multiplicities in *pp* interactions measured with the ATLAS detector at the LHC", (2010) arXiv:1012.5104

ATLAS Collaboration, G. Aad, A. Mapelli *et al.*, "Measurement of the top quark-pair production cross section with ATLAS in *pp* collisions at $\sqrt{s}$ = 7 TeV", (2010) arXiv:1012.1792

ATLAS Collaboration, G. Aad, A. Mapelli *et al.*, "Studies of the performance of the ATLAS detector using cosmic-ray muons", (2010) arXiv:1011.6665

ATLAS Collaboration, G. Aad, A. Mapelli *et al.*, "Measurement of underlying event characteristics using charged particles in *pp* collisions at $\sqrt{s}$ = 900 GeV and 7 TeV with the ATLAS detector", (2010) arXiv:1012.0791

ATLAS Collaboration, G. Aad, A. Mapelli *et al.*, "Observation of a Centrality-Dependent Dijet Asymmetry in Lead-Lead Collisions at $\sqrt{S_{NN}}$= 2.76 TeV with the ATLAS Detector at the LHC", (2010) arXiv:1011.6182

ATLAS Collaboration, G. Aad, A. Mapelli *et al.*, "Measurement of the $W \to l\nu$ and $Z/\gamma* \to ll$ production cross sections in proton-proton collisions at $\sqrt{s} = 7$ TeV with the ATLAS detector", (2010) arXiv:1010.2130

ATLAS Collaboration, G. Aad, A. Mapelli *et al.*, "Expected Performance of the ATLAS Experiment - Detector, Trigger and Physics", (2008) arXiv:0901.0512

Conference proceedings

Microfluidic cooling

A. Mapelli *et al.*, "Novel low material budget microfabricated cooling devices for particle detectors and front-end electronics", Proceedings of *The 12th Topical Seminar on Innovative Particle and Radiation Detectors (IPRD10)*, June 7-10, 2010, Siena, Italy

A. Kluge, A. Mapelli *et al.*, "NA62 Gigatracker", Proceedings of *19^{th} International Workshop on Vertex Detectors* June 6 -11 2010 Loch Lomond, Scotland, UK

M. Morel, A. Mapelli *et al.*, "The electro-mechanical integration of the NA62 Giga Tracker time tagging pixel detector", Proceedings of *TWEPP-10: Topical Workshop on Electronics for Particle Physics*, September 20-24, 2010, Aachen, Germany

Microfluidic scintillation detection

A. Mapelli, B. Gorini, M. Haguenauer, S. Jiguet, N. Vico Triviño and P. Renaud, "SU-8 microfluidic device for scintillation particle detection", Proceedings of *The 23rd European Conference on Sensors, Actuators and Microsystems (Eurosensors)*, Sep. 6-9, 2009, Lausanne, Switzerland

A. Mapelli, B. Gorini, M. Haguenauer, S. Jiguet, N. Vico Triviño and P. Renaud, "Development and studies of novel microfabricated radiation hard scintillation detectors with high spatial resolution", Proceedings of *The 1st International Conference on Advancements in Nuclear Instrumentation, Measurements Methods and their Applications (ANIMMA)*, June 7-10, 2009, Marseille, France

A. Mapelli, B. Gorini, M. Haguenauer, S. Jiguet, N. Vico Triviño and P. Renaud, "Novel radiation hard microfabricated scintillation detectors with high spatial resolution", Proceedings of *The 11th Pisa Meeting on Advanced Detectors*, May 24-30, 2009, La Biodola, Isola d'Elba, Italy

A. Mapelli, B. Gorini, M. Haguenauer, S. Jiguet and P. Renaud, "Development and studies of a novel microfabricated radiation hard scintillation particle detector with high spatial resolution", Proceedings of *The 11th Topical Seminar on Innovative Particle and Radiation Detectors (IPRD08)*, October 1-4, 2008, Siena, Italy

Absolute Luminosity For ATLAS

A. Mapelli, "ALFA: Absolute Luminosity For ATLAS - Development of a scintillating fibre tracker to determine the absolute LHC luminosity at ATLAS", Proceedings of *The 11th Topical Seminar on Innovative Particle and Radiation Detectors (IPRD08)*, October 1-4, 2008, Siena, Italy

A. Mapelli, "Development of a detector (ALFA) to determine the absolute LHC luminosity at ATLAS", Proceedings of *The 10th International Conference on Advanced Technology and Particle Physics (ICATPP)*, October 9-12, 2007, Como, Italy

Book chapters

A. Mapelli, B. Gorini, S. Jiguet, N. Vico Triviño, P. Renaud, "SU-8 Processes for Microfluidic Radiation Detectors and Integrated Optical Waveguides", in *Horizons in World Physics*, **275**(2011) **ISBN**: 978-1-61324-015-1.

Invited speaker presentations

A. Mapelli, P. Petagna *et al.*, "R&D on Microchannel Cooling for the NA62 Experiment at CERN", *Technological Seminar*, IBM Zurich Research Laboratory, Ruschlikon, Switzerland, September 21, 2010.

A. Mapelli and P. Petagna, "Low material budget microfabricated cooling devices for particle detectors and front-end electronics 2009 testbeam and beyond", *Technological Seminar*, LPHE, Ecole Polytechnique Fédérale de Lausanne, Switzerland, August 30, 2010.

A. Mapelli, "Microfluidic scintillation detectors", *Technological Seminar*, INFN Gruppo Roma, Università La Sapienza, Roma, Italy, March 19, 2009.

A. Mapelli, "Microfluidic scintillation detectors", *Technological Seminar*, Laboratory of High Energy Physics, University of Bern, Switzerland, December 9, 2008.

Conference talks

A. Mapelli, "SU-8 microfluidic device for scintillation particle detection", Presented at *The 23rd European Conference on Sensors, Actuators and Microsystems (Eurosensors)*, Sep. 6-9, 2009, Lausanne, Switzerland

A. Mapelli, "Development and studies of a novel microfabricated radiation hard scintillation particle detector with high spatial resolution", Presented at *The 11th Topical Seminar on Innovative Particle and Radiation Detectors (IPRD08)*, October 1-4, 2008, Siena, Italy

A. Mapelli, "ALFA: Absolute Luminosity For ATLAS - Development of a scintillating fibre tracker to determine the absolute LHC luminosity at ATLAS", Presented at *The 10th International Conference on Advanced Technology and Particle Physics (ICATPP)*, October 9-12, 2007, Como, Italy

Conference posters

A. Mapelli "Novel low material budget microfabricated cooling devices for particle detectors and front-end electronics", Presented at *The 12th Topical Seminar on Innovative Particle and Radiation Detectors (IPRD10)*, June 7-10, 2010, Siena, Italy

A. Mapelli, "Novel radiation hard microfabricated scintillation detectors with high spatial resolution", Presented at *The 11th Pisa Meeting on Advanced Detectors*, May 24-30, 2009, La Biodola, Isola d'Elba, Italy

A. Mapelli, "ALFA - Absolute Luminosity For ATLAS - a scintillating fibre tracker", Presented at *The 1st EIROforum School on Instrumentation (ESI 2009)*, May 11-15, 2009, Geneva, Switzerland

A. Mapelli, "Development and studies of novel microfabricated radiation hard scintillation detectors with high spatial resolution", Presented at *The 1st International Conference on Advancements in Nuclear Instrumentation, Measurements Methods and their Applications (ANIMMA)*, June 7-10, 2009, Marseille, France

A. Mapelli, "ALFA: Absolute Luminosity For ATLAS - Development of a scintillating fibre tracker to determine the absolute LHC luminosity at ATLAS", Presented at *The 11th Topical Seminar on Innovative Particle and Radiation Detectors (IPRD08)*, October 1-4, 2008, Siena, Italy

CERN technical reports

NA62 Collaboration, A. Mapelli *et al.*, "NA62 Technical Design Report" (2010)

A. Mapelli and C. Joram, "Design and Construction of a Cosmic Test Bench for ALFA", (2010) Under preparation

A. Mapelli, C. Joram and F. Ravotti, "Design and Construction of a Cosmic Test Bench for TOTEM", (2010) Under preparation

A. Mapelli, "Studies and development of a megnetic shield for the ALFA MAPMTs", (2010) CERN-ATL-COM-LUM-2010-007

B. Allongue, A. Mapelli *et al.*, "Test Beam 2008: First measurements with an ALF Roman Pot Prototype", (2010) CERN-ATL-LUM-INT-2009-001

ATLAS Collaboration, "ATLAS Forward Detectors for Measurement of Elastic Scattering and Luminosity Determination", ATLAS TDR 18 (2008) CERN-LHCC-2008-004

A. Mapelli, "ALFA: Absolute Luminosity For ATLAS - Development of a scintillating fibre tracker to determine the absolute LHC luminosity at ATLAS", (2007) CERN-ATL-LUM-PUB-2007-006

S. Ask, A. Mapelli *et al.*, "Noise and Cross-Talk Studies of the ALFA Prototypes in 2006 Testbeam at CERN", (2007) CERN-ATL-COM-LUM-2007-010

A. Mapelli *et al.*, "Characterization of irradiated plastic scintillating fibres for the ATLAS luminosity tracker", (2007) CERN-ATL-COM-LUM-2007-009

A. Mapelli and C. Joram, "Estimation of the delta ray production in the ALFA detector 10_2_6", (2007) CERN-ATL-COM-LUM-2007-005

A. Mapelli *et al.*, "Design, Construction and Metrology of the Overlap Detectors for the ALFA System", (2007) CERN-ATL-COM-LUM-2007-004

A. Mapelli and C. Joram, "ALFA Overlap Detectors Prototype Study from the CERN Testbeam in 2006", (2007) CERN-ATL-COM-LUM-2007-003

P. Barillon, A. Mapelli *et al.*, "Test of Scintillating Fibres Prototype Detectors using the OPERA front-end read out chip", (2006) CERN-ATL-LUM-PUB-2006-008

A. Braem, A. Mapelli *et al.*, "Metrology Results of the ALFA 2006 Prototype Detectors", (2007) CERN-ATL-LUM-PUB-2006-007

Supervision of student projects

N. Vico Triviño, "Development and studies of microfluidic waveguides", EPFL Master Thesis, 2009

N. Vico Triviño, "Fabrication of high aspect ratio structures in SU-8 for high spatial resolution microfluidic scintillation detectors", EPFL Semester Project, 2009

L. Hans, "Etudes de photodiodes pour un détecteur de particules intégré basé sur la scintillation microfluidique", EPFL Semester Project, 2009

S. Jakobsen, "Characterization of the MPPC S10362-11-100U by Hamamatsu and implementation in a set-up to measure scintillating fibres", CERN Summer Student, 2008

H. Dam, "Characterization of Irradiated Fibers for the ATLAS ALFA Luminosity Detector", CERN Summer Student, 2007

P. Canta, "Characterization of a set of MAPMTs for the ALFA prototype detector", CERN Summer Student, 2006

A. Kocnar, "Metrology and testing of detectors used in ATLAS ALFA", CERN Summer Student, 2005